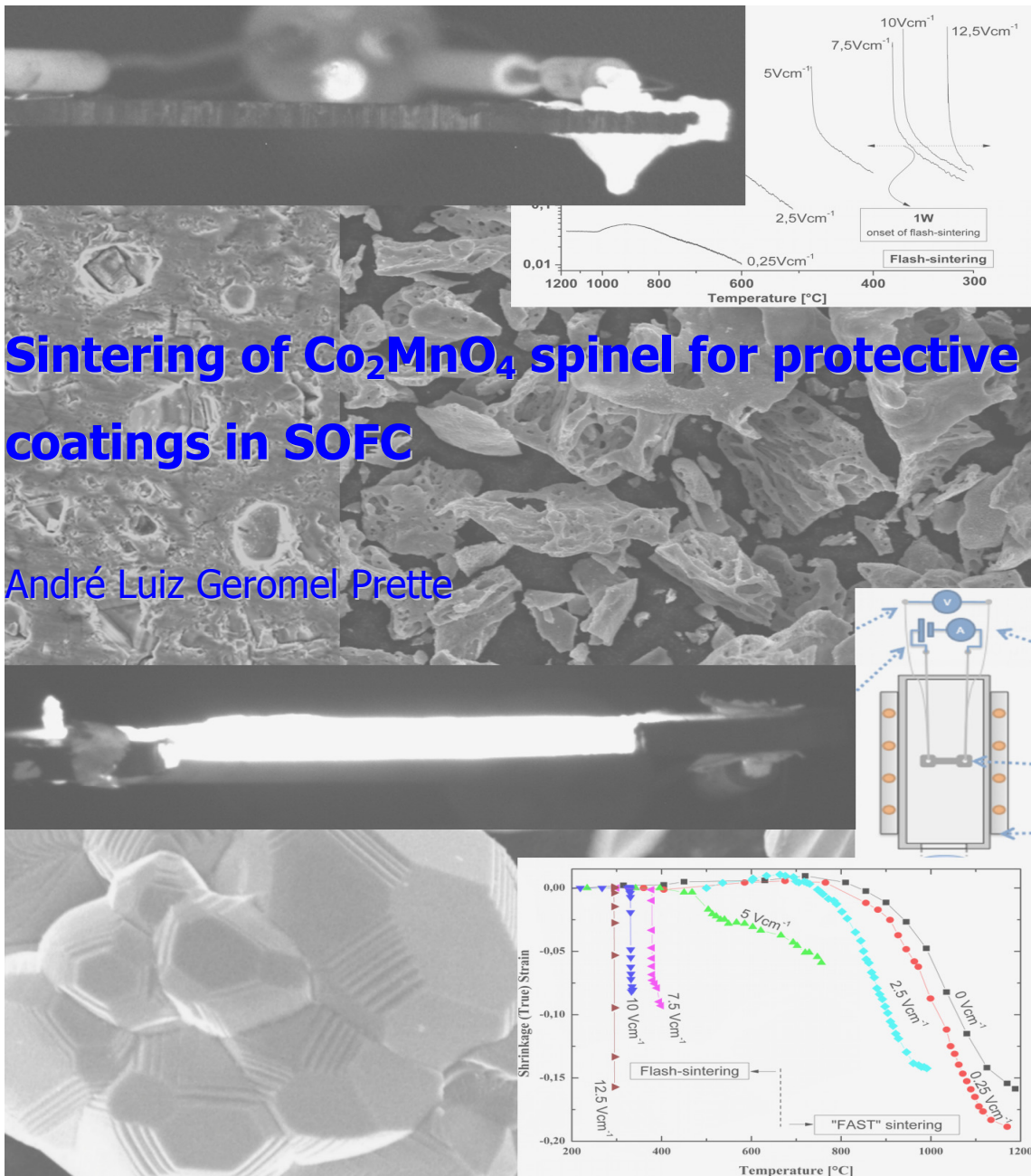UNIVERSITY
OF TRENTO - Italy

Department of Materials Engineering
and Industrial Technologies

Doctoral School in Materials Engineering – XXIII cycle

Sintering of Co$_2$MnO$_4$ spinel for protective coatings in SOFC

André Luiz Geromel Prette

April, 2011

Doctoral thesis

Sintering of Co$_2$MnO$_4$ spinel for protective coatings in SOFC

André Luiz Geromel Prette

Advisor:
Prof. Ing. Vincenzo M. Sglavo

Doctoral Committee:

Prof. Gian Domenico Sorarù, Università degli Studi di Trento

Prof. Herbet Danninger, Vienna University of Technology

Prof. Michel Vert, Université de Montpellier I

Prof.ssa. Laura Montanaro, Politecnico di Torino

To my wife Tatiane

ABSTRACT

Protective coatings are often deposited on SOFC interconnectors to avoid poisoning of cathode from chromium species that evaporate from stainless steel interconnects or supports. Co_2MnO_4 spinel compounds are usually considered as the main constituent of protection barriers. Nevertheless, such ceramic sinters at high temperatures (>1200°C) and this can be problematic for the properties of the stainless steel components. One of the major issues is, in fact, the creation of a compact and impermeable coating at relatively low temperature in order to preserve the metal substrate. In the present research work, Co_2MnO_4 spinel was synthesized by various methods (solid-state, gel-combustion, co-precipitation and reverse micelle) and the obtained specific surface area, structure and particle size were correlated with thermal behaviour, sintering temperature and achieved density. It was found that regardless the synthesis process the only obtained phase is Co_2MnO_4. Specific surface area from 0,8 to 65 m^2g^{-1} was obtained, depending on the synthesis method.

Sintering aids such as Nb_2O_5 and LiF were used to obtain dense microstructure at relatively low temperature. Considerable changes in sintering temperature were observed this being even 100-200ºC lower than that necessary for the consolidation of pure spinel though microstructure with only close pores was achieved.

A novel sintering method based on Field Assisted Techniques (FAST) that promoted flash-sintering phenomenon was finally applied to Co_2MnO_4. Small electric field ($<7,5$ V cm^{-1}) applied to the spinel decreases the sintering temperature down to 600°C. The application of an electric field above 7,5 V cm-1 flash-sintering phenomenon takes place and sintering temperature drops to about 300°C, the sintering time being less than 1 second.

UNIVERSITY OF TRENTO - Italy

ACKNOWLEDGEMENTS

To work colleagues Anna, Vincenzo, Marzio, Michele, Emanuelle, Amaia, Elisa, Aylin, Francesca, Valeria, Alexia, Pradeep, Aravind, Andrea, Claudia, Ricardo, Ernesto, Livio, John and Alessandro for their patience, sympathy and eventually help.

To my family and friends who bear the pain of my absence in the way of my progress.

To all my friends made during my staying in Europe, for their fellowship and for all the time we spent together.

To Stefano Brichetti, Fabrizio Mognabosco and Giani Voltolini who gave us the opportunity to live in apartment I lived and made the period at Opera Universitaria as better as possible.

To all the professors of DIMTI at UniTN related or not with the PhD program in Materials engineering, a special acknowledge to Giovanna Carlà for all the help and understanding during the PhD program.

To Prof. Vincenzo Sglavo for his patience and wisdom to pull me toward the right direction of my work and for all the tutoring and help provided.

To God to give be wisdom and strength to achieve the conclusion of this work.

CONTENTS

1. INTRODUCTION

Much is discussed regarding fuel cells, commonly associated as hydrogen cells or even hydrogen power. The reason for this can be because at its beginning it was mainly used with hydrogen as fuel and oxygen as oxidizing agent. Many people still think that fuel cells will rise from the sketch to the real life. It was and still is a controversial topic.

Scientists are normally optimist about fuel cell future, especially for what regards low temperature fuel cells. Now a days more and more researches are been done in order to utilize fossil fuel or reformed fuels in fuel cells.

In March 11, 2011 a big earthquake (9,0 Richter scale) followed by a Tsunami hit the biggest Island of Japan (Honshu) damaging the Power Plant complex of Fukushima. The atomic power plan was constituted by six atomic reactors where three of them had problems with cooling system and exploded releasing atomic dust and radioactivity on the surrounding area of the power plant and to the world. Based on this natural and nuclear accident, agencies all around the world pronounced themselves against atomic power and froze new contracts and construction of atomic power plants.

Since the world still tries to reduce the use of fossil fuels and the same time to reduce global warming it is the thought of the author that fuel cell will play an important role in the near future regarding the energy.

Fuel cells are often known as "green energy" or clean energy because to produce energy (in the conversion process) only inert gases and water are, in theory, released.

Pessimist researches and some politicians are often exposing that fuel cells are not good due to the investment of massive funds in the fuel cell research field with limited returns. The same occur to the investment by the industry side.

It is common for the skeptic people to take the amount of funds injected in the fuel sector in respect to the return of these funds and compare with the funds injected in the more established and developed fields, i.e. internal combustion engines, regarding the return of this field. In this case an important point that has to be taken in to account is that these more grounded technologies have in some cases hundreds of years of development.

Nowadays many types of fuel are been used in fuel cell and also many types of cell are also developed. Some of these types are currently been tested as standalone unit, i.e. molten carbonate and solid oxide fuel cell, and mobile devices to be used in busses, i.e. tubular solid oxide fuel cells and polymeric membrane fuel cell.

Fuel cells still remain as a costly energy due to the production cost and pricy materials. However, there is no reason to think that once the fuel cell production lines starts to assemble large number of units, like in a industrial

production line, the prices would not drop to some acceptable range and turn this technology commercially available. It is expected with fuel cell production the same kind of behaviour that happened with automobile industries.

Centuries ago automobiles were very expensive and restricted to few personalities who could pay for that and in some cases were choose to have an automobile, some decades after the first unit was sold the price per unit dropped already 60-70%. It is hoped that in this century fuel cell market will become more available and cheap, especially about solid oxide fuel cells. What render solid oxide fuel cell more interesting technology among fuel cells is the wide possibility to use multi-fuel (hydrogen, carbon monoxide, methane, etc.) and high temperatures allowing hybrid systems and cogeneration through the high temperature exhaustion. The use of cogeneration and hybrid system can afford very high efficiency in the conversion of fuel to usable energy i.e. electricity and heat.

The high efficiency estimated in the fuel cells pull me toward the choice to dedicate my PhD thesis to enhance this sector. Decrease costs, increase lifetime and reliability were one the thoughts pursued during the time of course thinking environmentally as well to reduce the pollution and provide cheaper energy.

One specific part of the fuel cells is the interconnector, which makes the contact of one cell and the adjacent. A brief search about articles in

ScienceDirect returns 1406 articles published using SOFC interconnect as keywords, works are remote as 1990 when few was talked about fuel cells. Still today interconnect for SOFC is very much studied as well as coatings for interconnect to improve performance and lifetime. Very common coating for interconnects is Co_2MnO_4 that is the focus of this PhD work.

In the present thesis some syntheses of Co_2MnO_4 Spinel are discussed, so the use of sintering aids and novel sintering techniques.

The work and research about cobalt manganese oxide spinel was idealized in collaboration with the company SOFCPower that produces planar solid oxide fuel cells. Many PhD theses were done in collaboration with this company what shows their commitment with research and improvement of their product through scientific and methodological pursuit. Another part of the research was carried out during a visiting period at the University of Colorado at Boulder (USA), in collaboration with Prof. Rishi Raj.

a) Synthesis of Co_2MnO_4 spinel

Solid oxide fuel cell stacks are basically composed by the cells itself, interconnectors and sealing. Interconnectors are the linking part that is in contact with one cell and the adjacent. Interconnectors are in contact with both oxidizing and reducing atmospheres. In the SOFC hereof studied, metallic interconnect is used and since temperatures as high as 1000°C are

applied in operation, even stainless steel suffer some oxidation at the cathode side (air side). Usually stainless steel used in these cases are high chromium steel, which rises another problem, cathode poisoning by chromium species. To avoid or minimize these problems it was previously studied the use of protective coating made of cobalt manganese oxide (Co_2MnO_4) spinel. When the beginning of this research there were no commercially available Co_2MnO_4 spinel, which is used as barrier coating in the planar SOFC. Since the sintering temperature of this material is reasonably high, new syntheses methods were studied in order to obtain cobalt manganese oxide spinel powder with properties compatible with what was expected regarding final density, sintering temperature and cost.

The first aim of this work was to develop a scalable synthesis method to produce cobalt manganese oxide at industrial scale producing reliable powder that can be sintered at a lowest temperature possible with cheapest production cost possible.

Solid-state reaction method was the first to be tried since it is the simplest and cheapest method, not the best though. Solid-state method was followed by gel-combustion method that produced very good spinel powders at low cost and with possibility to produce the powder in a continuous production similarly to the plasma spray technique. Another SOFCPower co-worker previously studied gel-combustion method that became the control method for the production of spinel. Novel production methods such co-

precipitation of cobalt oxyhydroxide with manganese sulfate and reverse micelle were also developed. The aim was always to obtain cobalt manganese oxide easily sinterable and offering a better barrier effect by means of dense structure and lowest temperature possible.

While the research was carried out two commercial producers of cobalt manganese oxide grounded their line at affordable prices with very good properties. The powder produced by these producers was also studied (characterized not synthesized).

b) Sintering-aids for Co$_2$MnO$_4$ spinel

Cobalt manganese oxide spinel was successfully produced but the sintering temperature achieved was quite high.

In a try to solve the problem and reduce the sintering temperature, without losing density, various sintering aid were tested to evaluate their use as sintering aid and the respective response upon temperature and density.

c) Sintering under electric field

This part of the work was carried out at University of Colorado at Boulder in collaboration with Prof. Rish Raj. A new attempt to sinter cobalt manganese oxide was tried applying electric field on the spinel to increase

its density at lower temperature and short time. Field assisted techniques are applied to sinter ceramic samples at lower temperatures since many years ago. It was studied, in the case of cobalt manganese oxide, the influence of direct current (DC) applied to the material. Through the application of electric field it was noted on the spinel a flash-sintering phenomena.

The phenomena of flash-sintering was previously reported by Prof. Raj in experiments with yttria stabilized zirconia. With the help of DC electric field fully dense cobalt manganese oxide spinel can be achieved at low temperatures and very short time.

2. THEORETICAL BACKGROUND

2.1. Introduction to Fuel Cells

The principle of the fuel cell was discovered by German scientist Christian Friedrich Schönbein in 1838 and published in *Annalen der Physik und Chemie* [1]. Based on this work, Sir William Robert Grove demonstrated the first fuel cell in the February 1839 edition of the Philosophical Magazine and Journal of Science [2]. Later on in 1842 Sir Grove sketched, also in the Philosophical Magazine and Journal of Science, his primitive fuel cell device that was pretty much similar to today's phosphoric-acid fuel cell [3]. Thirteen years after Grove sketched his device, in 1855, Willard Thomas Grubb further modified the original fuel cell design by using a sulphonated polystyrene ion-exchange membrane as the electrolyte. Three years later a fuel cell type "Grubb-Niedrach" was developed when Leonard Niedrach devised a way of depositing a catalyst for the necessary hydrogen oxidation and oxygen reduction reactions, in this case platinum, onto the sulphonated polystyrene ion-exchange membrane. "Grubb-Niedrach" was the first commercial use of fuel cell.

Later in 1959, Bacon and his colleagues demonstrated a practical five-kilowatt unit capable of powering a welding machine [4],[5]. In the 1960s, Pratt and Whitney licensed Bacon's U.S. patents for use in the U.S. space

program to supply electricity and drinking water (hydrogen and oxygen being readily available from the spacecraft tanks).

Nowadays energy is a very important trade. The world is always looking for more reliable, efficient, cheap and environmentally friendly energy. Since 70ies Fuels Cells are been quoted to be the power supply for the future. This is because the fuel cells are meant to produce green energy [6] from non-fossil fuels and release as side products non-polluting materials. Fuel cells can have a very broad efficiency range due to different configurations, designs types and fuels. It is common to see fuel cells with fuel-to-electricity efficiency as high as 55% that can be even increased by using hybrid systems [7]. Fuel cells have a very high efficiency if compared to engines that uses Carnot cycle, where the efficiency is 10-15% [8].

Hybrid systems are a combination of various energy-gathering systems, an example is showed in figure 1. Fuel cells normally work at higher temperatures than the ambient temperature. This is also related to internal reaction of oxidation-reduction that releases electrical energy and heat used in the fuel cell itself. The excess of heat produced can be used to heat a room or to produce hot water (through heat exchanging devices) and much more, thus saving energy [7].
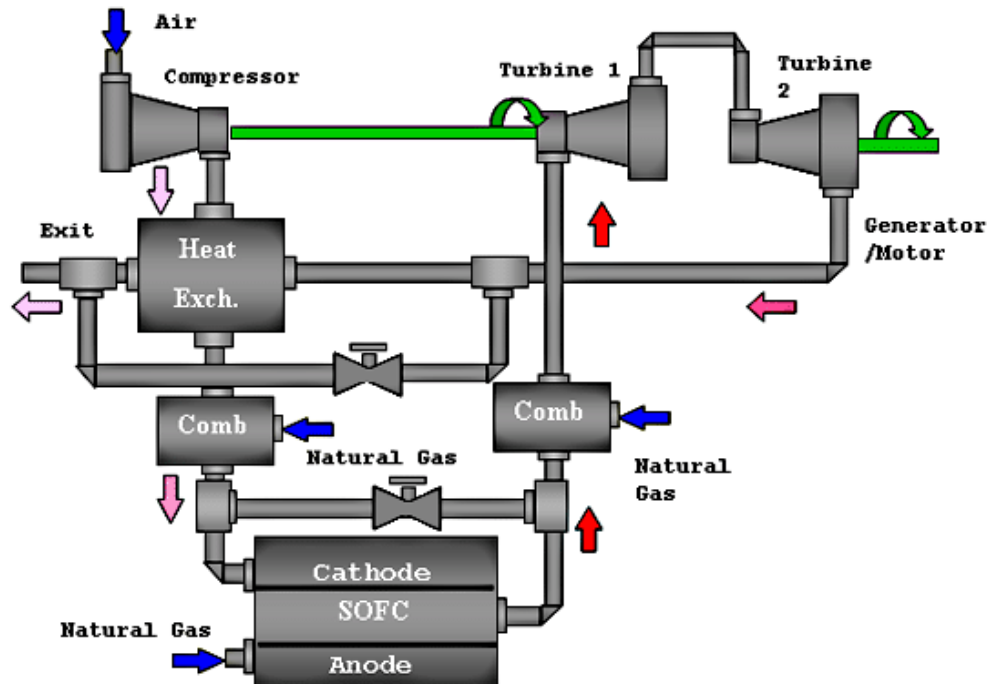
Figure 1 – Example of hybrid fuel cell-gas turbine system [7].

A basic work principle schema of a fuel cell is showed in figure 2. At the anode side fuel is oxidized with the help of a catalyst agent, thus producing free electrons and becoming positively charged; at the cathode side an oxidizing agent, usually oxygen, is dissociated by receiving the electron generated at the anode. The ions produced migrate through the electrolyte to recombine at the other side of the cell. The RedOx reaction between a fuel supply and an oxidizing agent generates electrical energy and heat. Many combinations of fuels and oxidants are possible.

24

HALF CELL REACTIONS

OXIDATION
$H_2 + O^{2-} \rightarrow H_2O + 2e^-$

REDUCTION
$O_2 + 4e^- \rightarrow 2O^{2-}$

e^- e^-

H_2

O^{2-}

H_2O

O_2
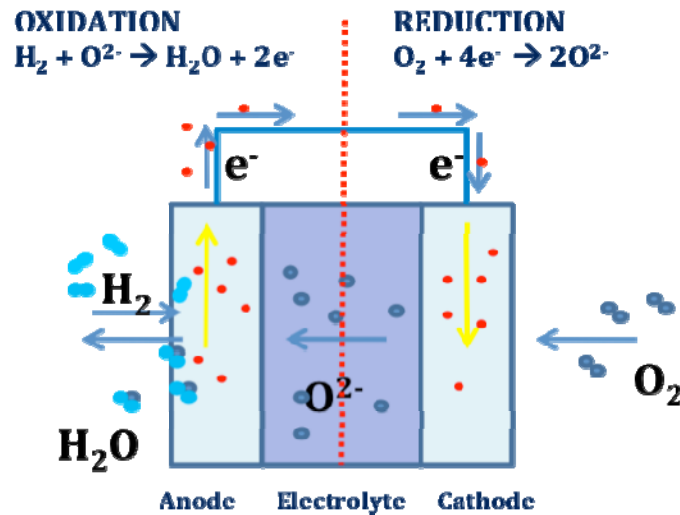
Anode   **Electrolyte**   **Cathode**

Figure 2 – Basic work principle of a fuel cell.

In practice, fuel cells cannot store energy like a battery, but in some applications, they can be combined to discontinuous power source systems such as solar or wind power that are connected with electrolyzers that convert energy to fuel and store it to be used by the fuel cell when needed. That is also known as energy storage system [9]. The overall efficiency (electricity to hydrogen and back to electricity) of such plants (known as round-trip efficiency) is between 30 and 50%, depending on conditions [9],[10]. While a much lead-acid battery might return about 90% of the total input, the electrolyzer/fuel cell system can store indefinite quantities of hydrogen, and is therefore better suited for long-term usage [10].

The most important element in a fuel cell is the electrolyte, which usually defines the type of fuel cell. According to the electrolyte type the different fuel cells can have various working temperatures, from 10°C (283K) up to 1000°C (1273K). Table 1 shows the different types of fuel cells and some of their characteristics.

Table 1 – Principal characteristics of various types of fuel cells [11].

Fuel Cell Type	Low temperatures fuel cells				High temperatures fuel cells	
	PEMFC	DMFC	AFC	PAFC	MCFC	SOFC
Electrolyte	Polymer	KOH or NaOH (aq.)	Alkaline	H_3PO_4	Molten Carbonate	Ceramic
Fuel used	H_2	CH_3OH	pure H_2	H_2	H_2, CO, CH_4	H_2, CH_4
Charge Carrier	H^+	OH^-	OH^-	H^+	$CO3^{--}$	O^{--}
Operating Temp.[°C]	25–120	50	65 - 220	120 - 200	650	700 - 1000
Qualified Power	100W-500kW	100mW-1kW	10-100kW	<10MW	100MW	<100MW
Efficiency (cell) [%]	50-70	20-30	60-70	55	55	60-65
Efficiency (system) [%]	30-50	10-20	62	40 Co-Gen:90	47	55-60
Interconnect	Carbon or metal	Metal	Metal	Graphite	Stainless steel or Nickel	Nickel, Ceramic or steel

2.1.1. Fuel cell efficiency

The thermal efficiency of an energy conversion device can be expressed as being the useful work done divided by the energy input. For a device that converts fuel chemical energy (Q_{chem}) to electrical work (W_{ef}) the efficiency expression (ε) then becomes [12],[13]:

$$\varepsilon = \frac{\dot{Q}_{chem}}{\dot{W}_{ef}} \qquad (1)$$

Based on the equation (1) one can say that the efficiency of a fuel cell is therefore dependent on the amount of power drawn from it. In addition, if more power is drawn that means more current is also been drawn increasing losses related to the current passage. Most losses manifest themselves as a voltage drop in the cell, so the efficiency of a cell is almost proportional to its voltage [12]. According to [13], a typical cell running at 0,7 V has an efficiency of about 50%, meaning that 50% of the energy content of the hydrogen is converted into electrical energy; the remaining 50% will be converted into heat. Depending on the fuel cell system design, some fuel might leave the system non-reacted, constituting an additional loss [13].

Fuel cells are not heat engines and so the Carnot cycle efficiency is not relevant to the thermodynamic efficiency of fuel cells [14].

2.2. Fuel Cell types

2.2.1. Proton exchange membrane fuel cells

Proton exchange membrane fuel cells (PEMFC) use a polymeric membrane as electrolyte, thus constituting a fuel cell. This type of fuel cell is also known as Polymer membrane fuel cell [15]. This electrolyte allows protons (hydrogen ions) from anode side to pass through it and recombine at the cathode side to produce electrical current, as showed in figure 3.
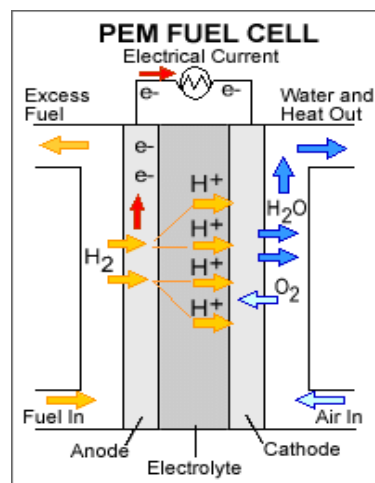

Figure 3 – Example of PEMFC [16].

The only liquid in this fuel cell is water, thus, corrosion problems are minimal. Usually the polymeric membrane applied to this cell is Nafion polymer. Typically, carbon electrodes with platinum are used for both anode and cathode, with either carbon or metal interconnections. The low operating temperature of the PEMFC allows a rapid start-up and, with the absence of corrosive cell constituents, avoids the need for exotic materials required in other fuel cell types [17].

2.2.2. Direct methanol fuel cells

Direct methanol fuel cells (DMFC) are a special category of proton-exchange fuel cells in which methanol is used as the fuel. A liquid solution of methanol and water is used as fuel. Pure methanol is not used to avoid cross-over phenomenon, which makes the methanol diffuses through the membrane without reacting. Cross-over remains a major factor in inefficiencies [17]. Figure 4 shows a simple sketch of a direct methanol fuel cell.

The reaction succeeded in the direct methanol fuel cell is the same that occur in the direct combustion of methanol. Equation 2 shows the reaction of methanol combustion:
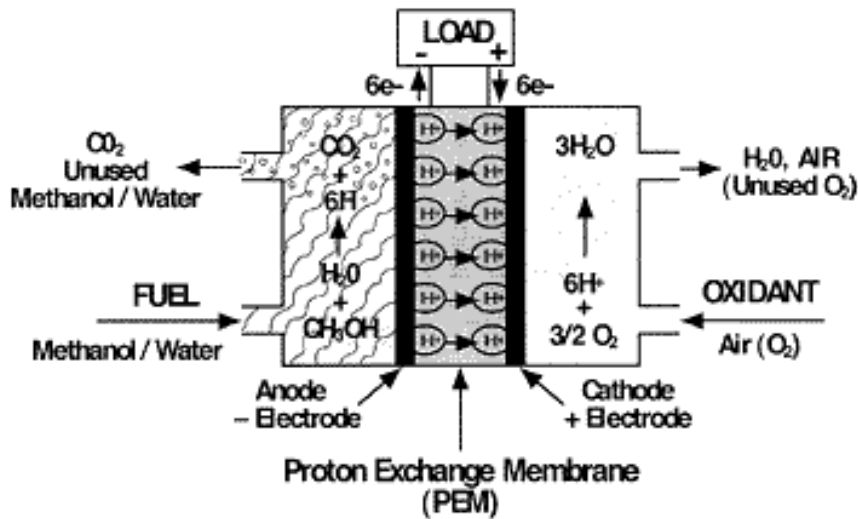
$$CH_3OH + \frac{3}{2}O_2 \rightarrow CO_2 + 2H_2O \tag{2}$$
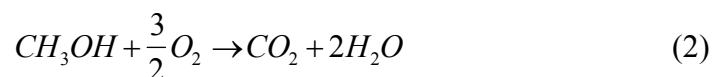
2.2.3. Alkaline fuel cells

Alkaline fuel cells (AFC) are one of the most efficient fuel cell, reaching 70% of efficiency [17]. Alkaline fuel cell was the fuel cell type that helped man to reach the moon; it was used in the Apollo Space Shuttle to generate electricity from hydrogen and oxygen pressurized and potable water. The electrolyte of alkaline fuel cell consists of a porous matrix filled with an aqueous solution of potassium hydroxide (KOH). The ions hydroxyls are, in this case, the working ions that migrate from one electrode to the other [19].

Any amount of CO_2 shall be avoided due to the risk of poisoning since the KOH is willed to form K_2CO_3. Usually pure hydrogen and pure oxygen are used in alkaline fuel cells. Due to the liquid characteristic of the electrolyte, once poisoned, the electrolyte can be replaced by new one, thus returning the cell to its original output. The need of CO_2 removal from the air (when it is used as oxidant) impact significantly on the size and cost of system [17]. figure 5 shows a schematic of AFC.
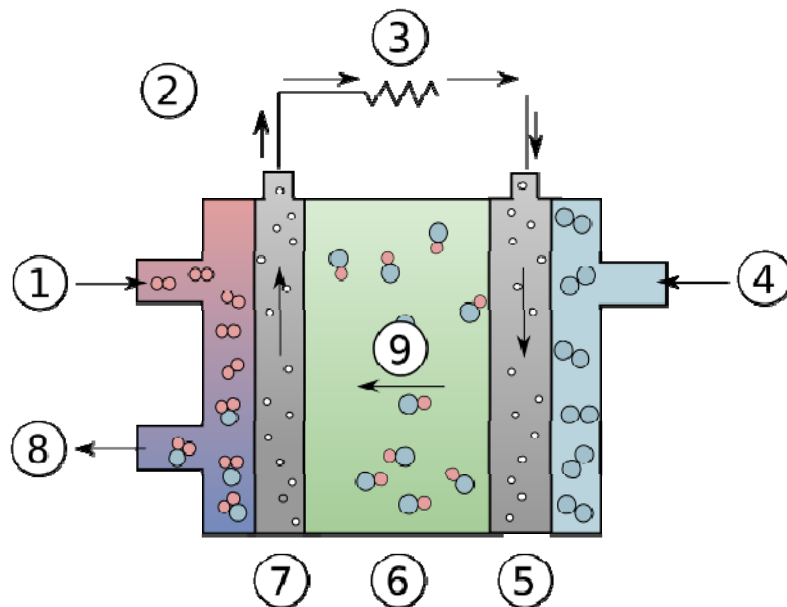
Alkaline Fuell Cell. 1: Hydrogen 2:Electron flow 3:Charge 4:Oxygen
5:Cathode 6:Electrolyte 7:Anode 8:Water 9:Hydroxyl Ions

Figure 5 – Schematic example of alkaline fuel cell [20].

2.2.4. Phosphoric acid fuel cells

Phosphoric Acid Fuel Cells (PAFC) use melted phosphoric acid as the electrolyte. Phosphoric acid is solid below 40°C; this type of cell operates at temperatures in range of 150-200°C, therefore is low-temperature fuel cell. Phosphoric acid fuel cell works like a proton exchange membrane fuel cell, where the protons (hydrogen ion) migrate through the electrolyte. The advantage of phosphoric acid fuel cell is that this type of fuel cell is not affected by CO_2 poisoning [17].
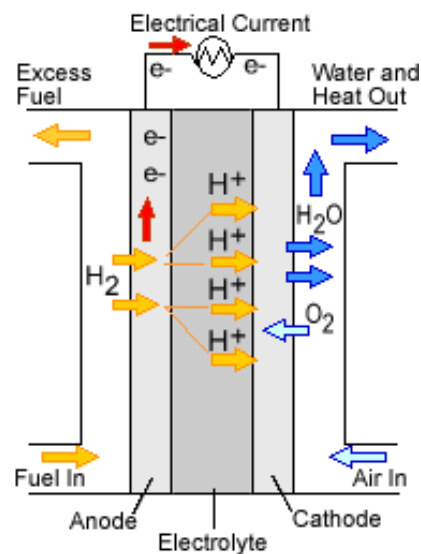

Figure 6 – Sketch of phosphoric acid fuel cell [16].

At lower temperatures, phosphoric acid is a poor ionic conductor, and CO poisoning of the platinum catalyst in the anode becomes severe. The use of concentrated acid minimizes the water vapour pressure, making water management relatively simple. The highly corrosive nature of phosphoric acid requires the use of expensive materials in the stack [17].

2.2.5. Molten carbonate fuel cells

Molten Carbonate Fuel Cells (MCFC) are considered high temperatures fuel cells, which works at temperatures above 650°C [17]. At this high temperature the alkali carbonates form a highly conductive molten salt, with carbonate ions providing ionic conduction [17]. Internal reforming is plausible in this type of fuel cell that can use hydrocarbons as fuel because its working temperature is considered high and there is no sensitivity to CO_2 poisoning. Molten carbonate fuel cells use as electrolytes molten carbonates mixtures, as the name says, suspended in a porous matrix [21],[22]. Molten carbonate fuel cells can reach efficiencies approaching 60%. When the produced heat is captured and used, overall fuel efficiencies can be as high as 85% [23]. The higher temperatures promote material problems, impacting on mechanical stability and stack life as well as impacting the fuel cell costs [17]. A schematic diagram of MCFC is showed in figure 7.
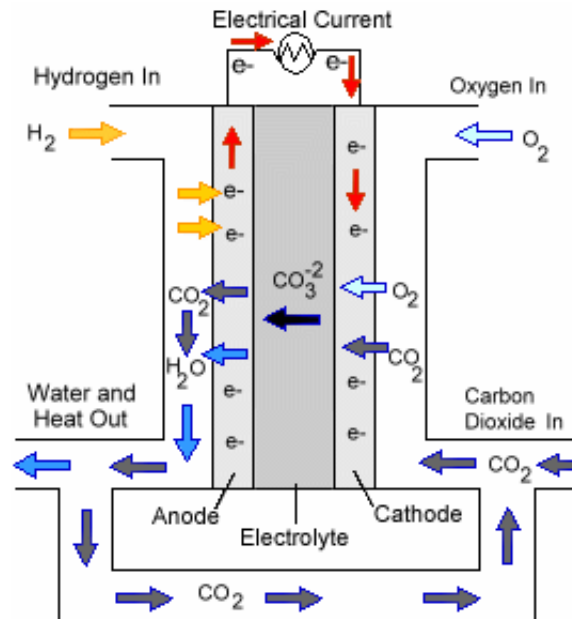
Figure 7 – Molten carbonate fuel cell diagram [16].

The oxidation reaction produces some carbonate losses that shall be refilled. Usually, recirculating carbon dioxide from the oxidation products promote the replenishing of carbonate [21].

Molten carbonate fuel cells can be used for reducing the CO_2 emission from coal fired power plants as well as gas turbine power plants [21],[22].

2.2.6. Solid oxide fuel cells

Solid Oxide fuel cells (SOFC) are the most common type of fuel cell. They are the most efficient devices yet invented for conversion of chemical fuels directly into electrical power [24]. They were idealized by Nernst and his colleagues at the end of the nineteenth century [24-26].

SOFCs contain a solid ceramic electrolyte, usually yttria stabilized zirconia, which serves as ion conductor at high temperatures [24],[26]. The usual working temperature of a solid oxide fuel cell varies from 600°C to 1000°C [24-26]. The high temperature depends on the thickness of the electrolyte, among other factors, and it needed to allow ion conductivity in the electrolyte [24],[27]. Working temperature depends also on the ionic conductivity desired for the cell electrolyte; more ionic conductivity better. The drawback is that with higher temperature more sophisticated, expensive and robust must be the cell materials. In addition, the high working temperature increases greatly the start-up time. Due to the high working temperature fuel internal reforming is likely possible thus increasing the flexibility of the fuel used, i.e. hydrogen, butane, methanol, and other petroleum products [24-26].

Solid oxide fuel cells have basically two different designs on stacks: planar and tubular (also known as Siemens-Westinghouse). Although the two basic designs of fuel cell, there are many variations of these two basic designs.

Practically each producer develops and applies its own design on the fuel cells. Figure 8 shows a graphical example of both type of design for fuel cell [28],[29].
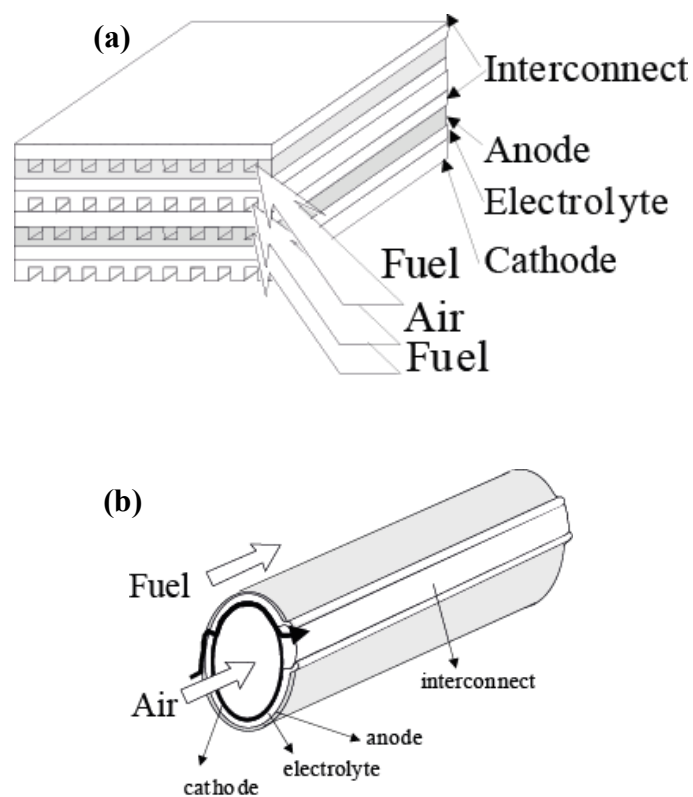
Figure 8 – Example of planar (a) and tubular (b) fuel cell design [28],[29].

Regardless the design used, five components are needed to put such a cell together: electrolyte, anode, cathode and two interconnect [24].

Tubular cells usually use the configuration of cathode supported cell whereas in the case of planar fuel cell it is usually produced in one of the following configurations: anode supported or electrolyte supported [28],[30]. The type of configuration will depends on which layer (material) the other components are stacked over. Figure 9 shows an example of electrolyte supported cell (a) and anode supported cell (b), the thickness presented is an indicative value and can vary from producer to producer.
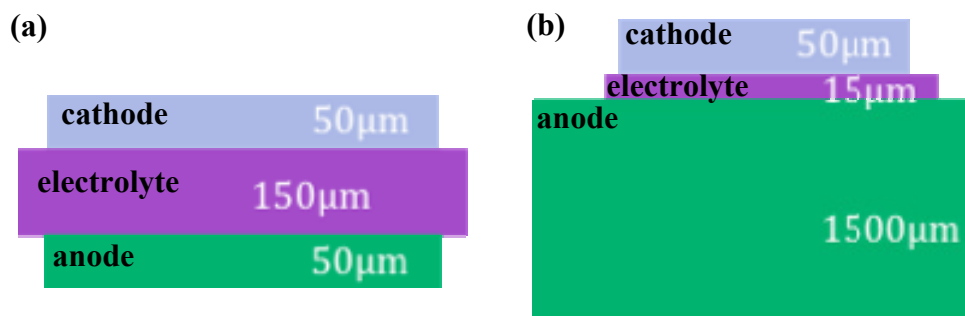
(a)

cathode   50μm

electrolyte   150μm

anode   50μm

(b)   cathode   50μm

electrolyte   15μm

anode

1500μm

Figure 9 – Example of planar cell designs (a) electrolyte supported cell (ESC) and (b) anode supported cell (ASC).

2.2.6.1. Electrolyte

The electrolyte is the usually treated as the core of the fuel cell, part because it is positioned in the middle of the cell; between the anode and the cathode, part because the type of fuel cell is determined by the type of electrolyte used (as previously explained) [31].

To be used as electrolyte in a solid oxide fuel cell some requirement on materials design are listed as follow [31]:

- ionically conductive (oxygen ion transport),
- electronically insulating,
- chemically stable at high temperatures, in oxidizing and in reducing environment,
- free of porosity,
- thermal expansion that matches electrodes,
- inexpensive materials.

Besides the well-known zirconia based materials as electrolytes many other ceramic-based materials are also used as electrolytes [24],[31]. Table 2 shows various examples of electrolyte materials [24],[31-33].

Table 2 – Examples of electrolyte materials.

Zirconia-based materials	Ceria-based materials	Lanthanum-based materials	Other Materials
YSZ	GDC	LSGM	BCY
SSZ	SDC	LSGMC	YSTh
CaSZ	YDC	LSGMF	YSHa
	CDC	LSGMCF	Bi oxide-based
		LaAlO$_3$ based	Pyrochlorores-based

2.2.6.2.   Anode

The anode is the electrode where the fuel is oxidized, thus the principal requirement is to be stable in the reducing environment [24],[28],[31],[34]. Porosity must be present to allow the fuel transport and the transport of the products of fuel oxidation. The anode must have also excellent electronic conductivity to carry the electrons from the electrochemical reaction to interconnect [28],[31],[34]. Good mechanical strength is also requirement, especially when the anode is used as support [28],[31],[34]. Anodes for solid oxide fuel cells are usually made into a cermet and more detailed requirements are [31]:

- electrically conductive,
- high electrocatalytic activity,
- avoid coke deposition,
- large triple phase boundary,
- stable in reducing enviroment,
- thickness compatible to the design (thin for ESC or thick for ASC),
- thermal expansion coefficient similar to adjacent components,
- chemically compatible with adjacent cell components.

Table 3 shows a list of possible materials for the anode of a solid oxide fuel cell [31].

Table 3 – Examples of materials used in the anode of solid oxide fuel cells.

Nickel Materials	Copper Materials	Lanthanum Materials	Other Materials
Ni-O/YSZ	$CuO_2/CeO_2/YSZ$	$La_{1-x}Sr_xCrO_3$	CeO_2/GDC
Ni-O/SSZ	CuO_2/YSZ	$La_{1-x}Sr_xCr_{1-y}M_yO_3$	TiO_2/YSZ
Ni-O/GDC	Cu/YZT	LST	Cobalt-based
Ni-O/SDC	$CuO_2/CeO_2/SDC$	LAC	Platinum-based
Ni-O/YDC			Ru/YSZ

2.2.6.3. Cathode

The cathode is the electrode where the oxidizing agent is reduced. The principal characteristic of this layer is that shall be oxidation resistant once it is always in contact with air (normally the oxidizing agent) at high temperature [24],[28],[31],[34]. Some of the characteristics required by the anode material also apply to the cathode material, i.e. electronic conductivity, porosity and others. In principle several mixed oxides satisfy the need of electronic conductivity and porosity for mass transport. Though, few of them are suitable to be used as cathode because the chemical incompatibility with electrolyte and thermal expansion coefficient does not match with other components [24],[28],[31],[34].

In order to be used as a cathode in solid oxide fuel cells the material shall obey some requirements:

- high electronic conductivity,
- chemically compatible with neighboring cell components,
- thickness compatible (thin enough to avoid mass transfer losses and thick enough to distribute the current generated),
- stable in oxidizing enviroment,
- large triple phase boundary,
- catalyze the dissociation of oxygen,
- high ionic conductivity,
- adhesion to electrolyte surface,
- thermal expansion coefficient similar to other SOFC materials,
- simple fabrication and relatively low cost.

Cathode materials are very common to be the reason for the solid oxide fuel to lose its performance. This happens because the cathode is susceptible to poisoning created by the migration of chromium species to the triple phase boundary of the cathode-electrolyte-air [35-37].

The choice of the cathode material depends on the chosen electrolyte material, the desired operating temperature, the cell design, and the specific ceramic fabrication methods [38],[39]. To exemplify how large is the range

of materials to be used as cathode in solid oxide fuel cells Table 4 show some examples of materials currently been used in SOFC [31].

Table 4 – Example of materials for cathode of solid oxide fuel cell.

Lanthanum Materials	Gadolinium Materials	Praseodymium Materials	Strontium Materials	Yttria Materials
LSM	GSC	PCM	SSC	YSCF
LSF	GSM	PSM	NSC	YCCF
LSC		PBC	BSCCu	YBCu
LSCF				
LSNC				
LSMCr				
LCM				
LSCu				
LSFN				
LNF				
LSCN				
LBC				
LNC				
LSAF				
LSCNCu				
LSFNCu				
LNO				

2.2.6.4.   Interconnect

Interconnect (also called bipolar plate) is the electric link between the cathode of one cell and the anode of the adjacent cell in a stack [31]. Interconnect also physically separates physically the two adjacent cells [28],[40]. The most severe requirements on the fuel cells are related to the interconnect [34]. Some design requirement for the interconnect are [31],[34],[40-42]:

- high temperature oxidation and reduction resistance (simultaneous fuel and oxidant gas exposure),
- stable under multiple chemical gas stream,
- nearly 100% electronic conductivity,
- low (or no) permeability for oxygen and hydrogen to minimize direct combination of fuel/oxidant,
- high density with no open or interconnected porosity,
- strong and high creep resistance,
- good thermal conductivity,
- phase stability on the working temperature range,
- low cost for materials and process,
- matching thermal expansion to other cell components,
- non reactivity with anode , cathode and sealing.

As presented above many are the requirements on interconnect and due to that few materials can sustain every requirement. Some material alternatives are shown in Table 5 [31],[40].

Table 5 – Example of materials for interconnect and coating on those.

Metals (base materials)	Ceramics (base materials) *no coating is required
chromium alloys	Lanthanum chromites
ferritic stainless steel	**Coating for metal base interconnect**
austenitic stainless steel	
iron super alloy	LSM
nickel super alloy	LCM
	LSC
	LSFeCo
	LSCr
	LaCoO3
	Co_2MnO_4

Although ceramic interconnect does not need coating the drawbacks that these materials suffer are limiting for their use [43],[44]:

- high sintering temperatures (1450-1600°C),
- high cost,
- no machinability and flexibility of shape.

Ceramic interconnect sintered at lower temperatures have lower density and, therefore, poor electronic conductivity [43],[44]. In addition, low sintering temperature of ceramic interconnect produce interconnect with open porosity [43],[44]. Another important drawback is that at low temperatures ceramic interconnect has poor electronic conductivity, thus making difficult the current passage at fuel cell start-up [43],[44].

Alternate materials to be used as interconnect are the metal based materials. In comparison with ceramic interconnect, metallic ones are stronger, easier to form, have higher thermal and electrical conductivities and negligible ionic conductivity [31]. However, metals must be protected against corrosion in oxidizing environments. Usually ceramic coatings are applied to the metallic interconnect to achieve this protection [35],[40],[41],[45]. For example, stainless steel that usually has high chromium content is often used as metal interconnect. Though, chromium tends to migrate to the triple phase boundary of cathode and promote the phenomenon of poisoning [46].

Among candidate materials in the metallic category is Crofer22 APU, a Fe-Cr based ferritic stainless steel with additional manganese (ThyssenKrupp VDM). This stainless steel cover pretty well the requirements of an interconnect and is largely used [47].

The use of bare Crofer22 APU is limited to the temperature where it is applied. Although the maximum workable temperature is rather high (~1000°C), above 800°C a thick chromium layer is formed [35],[48-50].

The formed chromium layer is deleterious to the performance of the fuel cell once it has lower electronic conductivity than bare stainless steel [35],[40]. In addition, the chromium oxide layer increases the amount of free chromium that can migrate to cathode and poison it.

2.2.6.5.   Coatings

Metallic interconnect usually requires a protective coating on the surface to protect against corrosion and to improve the lifetime of fuel cell [35].

Various coating materials were developed in order to reduce chromium evaporation. Initially they mostly considered perovskites layers on basis of lanthanum-strontium-manganite $(La,Sr)MnO_3$ or lanthanum-strontium-chromite $(La,Sr,)CrO_3$ [40],[41],[51],[52]. Subsequent tests were performed with spinel coatings based on cobalt manganese oxide specially $(Co,Mn)_3O_4$ [40-42],[47],[51],[53].

More recently [41],[45],[49],[54-56] started the use of Co_2MnO_4 spinel as barrier coating for interconnect. Cobalt manganese oxide spinel (Co_2MnO_4) is usually selected according to the high electrical conductivity and the good matching of thermal expansion coefficient coupled to stainless steel substrates [45],[57].

Since the use of spinel as coating shall be applied to relatively simple and large surfaces it is likely to coating procedure to be cheap and easy to coat

large areas in a industrial line process. The usual coating methods can vary from screen-printing, slurry-spraying, dipping, plasma spray and PVD [41],[56]. Some laboratory tests were also carried out using CVD which is much more expensive and not likely scalable to large surfaces [42].

2.2.7. Co_2MnO_4 spinel

Among various ceramic materials cobalt manganese oxide spinels are commonly used as protective layers because they have high electronic conductivity, are stable in oxidizing atmospheres, and have a thermal expansion coefficient close to stainless steel [55],[58]. In the case of cobalt manganese oxide spinel, microstructures with close pores are normally obtained, in a conventional sintering process, at temperatures of 1100°C or higher with dwell times of several hours [35],[49]. The use of such temperatures is not prohibitive from the point of view of instruments costs and technologies, but it is very excessive regarding the materials use. At these temperatures chromium species from stainless steel oxidize to form brittle phases that can crack and spall, moreover the chromium oxide formed is considerably less conductive then the stainless steel substrate [35],[40],[49].

2.3. Field assisted Sintering techniques

Novel techniques known as field assisted sintering techniques (FAST) have been recently used to produce advanced ceramics [59],[60]. There are many field assisted sintering techniques, each of them with their own sample characteristics, direction and application of the field, presence of and much more [59],[60].

Essentially, field assisted sintering techniques are methods that allow to sinter a material under an applied electric field. One of the primary use of an electric field was treated as Joule effect, where a current passes through a material generating heat (Figure 10).
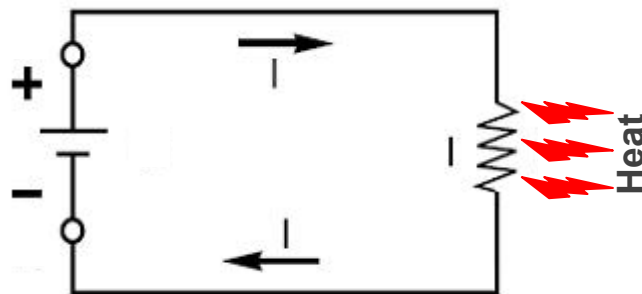
Figure 10 – Electrical diagram to exemplify heat generated by Joule Effect.

It is well known that in order to generate Joule effect, i.e. to heat a material, the material itself shall conduct electrons or ions [61]. The electrons flow

heats the material and, depending on the power applied, it reaches certain temperature capable to sinter itself (Direct Current Resistance Sintering) [60],[62].

To allow the sintering of non-conductive materials (such as aluminum oxide, titanium oxide, etc.) many other techniques have been developed. Inspired by the direct current resistance sintering, techniques like electric-discharge sintering (EDS), also known as spark sintering (SS), pulsed electric current sintering (PECS), plasma assisted sintering (PAS) and spark plasma sintering (SPS), among others, have been develop. Figure 11 shows a schematic difference between hot pressing and electric current assisted sintering (ECAS).
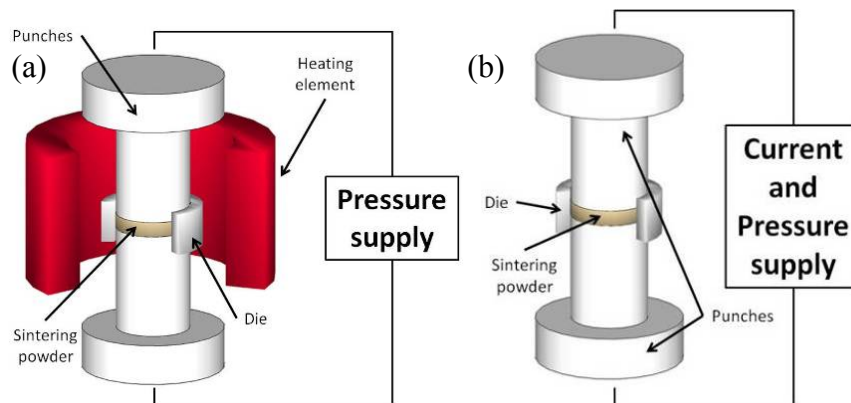
Figure 11 – Example of hot pressing (a) and electric assisted sintering (b) [60].

Techniques such as Spark Plasma Sintering use a mixed setup where the electrical heating is produced by the current flow through the die (in case of non-conductive samples) whereas the powder sample is also pressed. In this configuration the heat used to sinter the sample is applied the form indirect causing some energy losses. Figure 12 presents a basic spark plasma sintering setup.

Power supplier
pulse generator
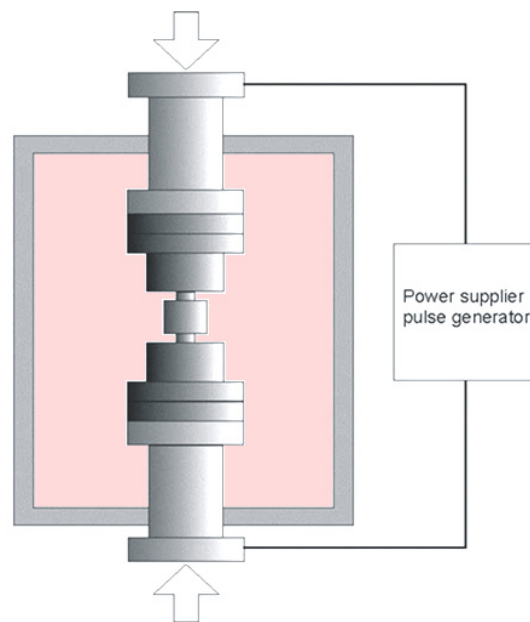
Figure 12 - Example of spark plasma sintering technique [64].

Sintering techniques can be assisted by pressure, as shown in figure 11(b), or they can be pressureless (Figure 13) [54],[63].
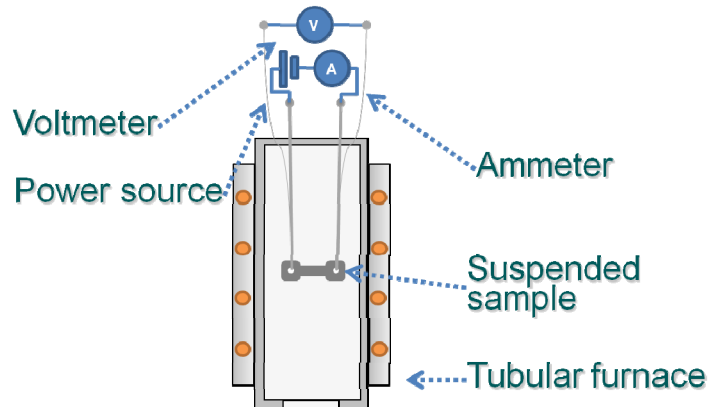
Figure 13 – Pressureless electric field assisted sintering.

To exemplify how the heat is applied to the sample in order to sinter it, figure 14 shows examples of conventional sintering method, spark plasma sintering and Flash-sintering.
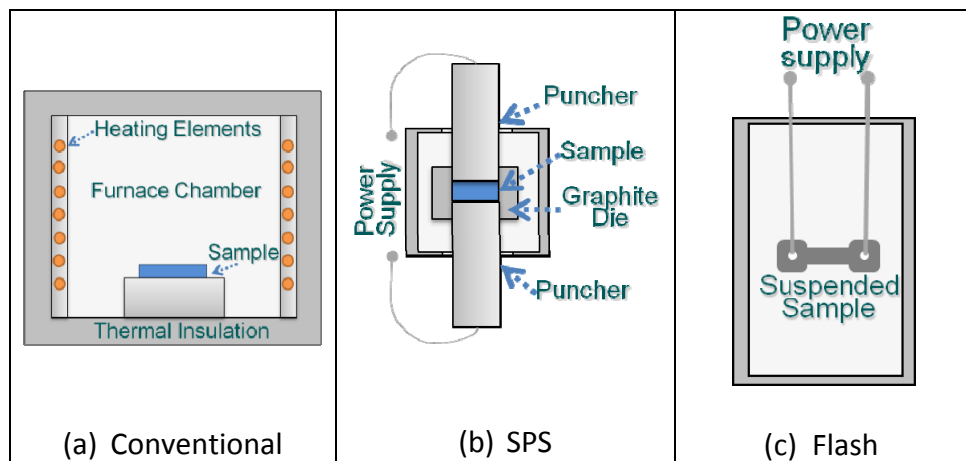
Figure 14 – Examples of heat transfer in (a) conventional furnace, (b) spark plasma sintering (SPS) and (c) pressureless flash-sintering.

It is clear that heat produced in the conventional furnace is also used to increase the temperature in whole furnace chamber (Figure 14(a)) thus wasting energy to heat the environment as well as the sample (indirectly). Spark plasma sintering applies heat directly to the die containing the sample thus avoiding the heat dispersion on furnace chamber (Figure 14(b)). The method of flash-sintering produces direct heating of the sample by applying current on it; this process increases the efficiency of the system and reduces losses due to heat waste (Figure 14(c)).

Further steps can be achieved by using pressureless and contactless field assisted sintering. This experiment was done by [65] in nanoparticles of silver, using AC (alternated current) and is shown in figure 15.
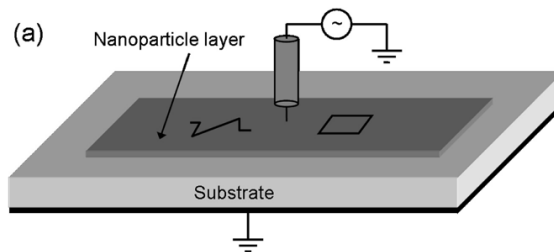
Figure 15 – Example of contactless electrical sintering. [65]

These electric current assisted sintering (ECAS) methods have been shown to reduce sintering times and temperatures by employing electromagnetic and electrical fields in combination with time, temperature and pressure.

Techniques that uses electromagnetic or electrical field to assist sintering are commonly called field assisted sintering techniques (FAST).

Recent studies have shown that direct current (DC) electrical fields applied to tetragonal 3 mol% yttria stabilized zirconia (3YSZ) and 8 mol% cubic yttria stabilized zirconia (8YSZ), which are ionic conductors, [63],[66],[67] can reduce the furnace temperature for sintering by hundreds degrees and the sintering time to just a few seconds [63],[67]. The enhancement in the sintering rate could be explained by slower rate of grain growth, as demonstrated by earlier work on fully dense specimens of 3YSZ, and by local Joule heating at grain boundaries [66],[68-70].

FAST processes may be used to lower the sintering temperature of Co_2MnO_4 and prevent the formation of Cr_2O_3 interlayer. In the present Chapter it will be shown that flash-sintering process can also be applied to Co_2MnO_4 spinel, which unlike yttria stabilized zirconia, is an electronic conductor. The sample is sintered without applying external pressure, and the experiments are carried out in a conventional furnace [54],[63],[67].

3. EXPERIMENTAL PROCEDURE AND RESULTS

Cobalt manganese oxide is an important material for increasing the lifetime of SOFC. In the present section, some studies about chromium oxide layer formation on Crofer 22 APU are shown; methods to produce an optimal Co_2MnO_4 powder are discussed and compared with commercial powders nowadays available; studies about sintering aid of Co_2MnO_4 are conducted and novel sintering techniques are presented.

Cobalt manganese spinel in form of powder is needed in order to be applied as coating on stainless steel substrates to protect them against excessive chromium oxide layer formation and also to avoid migration of chromium from the interconnect to the cathode. Among many reasons powder spinel is needed because: in powder form possibilities to apply the coating are broader (i.e. slurry-spray, screen-printing, dipping, etc), processing parameters are more controllable, possible to form thin layer and the characteristics of the powder command the layer properties.

3.1. Oxide layer formation on Crofer 22 APU

Crofer 22 APU is widely used as metallic interconnect to SOFC. It is usually coated with Co_2MnO_4 spinel and pre-oxidized at temperatures in the range of 800-900°C for 2h [35],[45],[49],[71]. However, this temperature is not sufficient to sinter the Co_2MnO_4 spinel layer to its full density or to produce a close porosity structure. Therefore, the following study has the purpose to understand the maximum possible temperature that can be applied to the Crofer 22 APU coated with Co_2MnO_4 spinel without the formation of sensible chromium layer.

Metal sheets of Crofer 22 APU were coated with gel-combustion produced Co_2MnO_4 spinel by using slurry-spray technique. The Co_2MnO_4 spinel was suspended in ethanol and homogenized for 15 min in a Shaker-Mixer Turbula®.

Coated pieces were submitted to thermal treatment at different temperatures (no heated, 900°C, 950°C and 1000°C). The isotherm time was 2 h for every sample. After thermal treatment the samples were embedded perpendicular (in a way to observe the cross-section of the coating), polished and observer in scanning electron microscopy.

The results for every temperature were compared to the green sample to evaluate the formation of Cr-rich layer as functions of temperature. Figure 16 shows the cross-section of Crofer 22 APU after different treatments.

[red line= Cr; green line = Mn; blue line= Fe; pink line=Co]
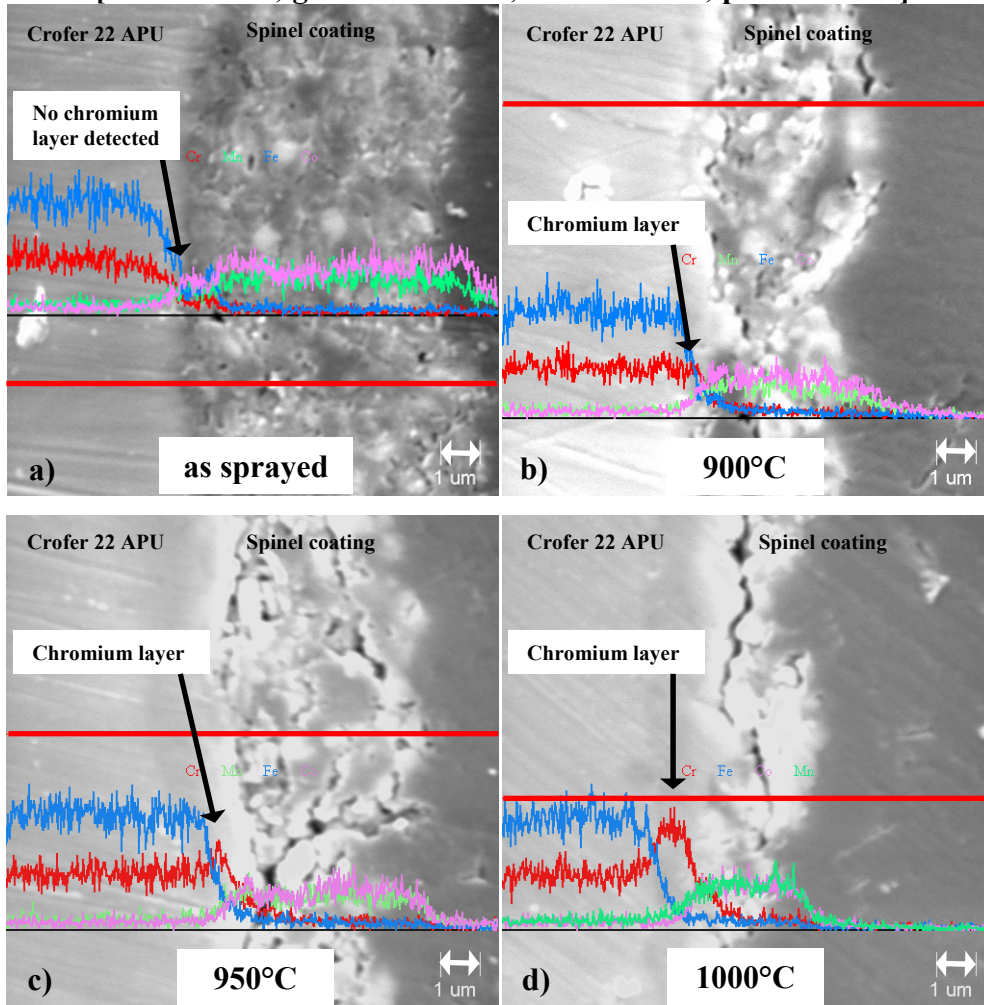
Figure 16 – Shows SEM micrographs of thermal treated Crofer 22 APU coated with Co2MnO4 spinel by slurry-spray method.

In figure 16 chromium layer formation is evidenced by the line-scan realized along the surface of the sample. In all samples the horizontal red line is where the line-scan measurement was done. The colour spectra represent the amount of each element along the line-scan.

Coating uniformity or sintering in this experiment was not considered since the purpose was to evaluate the chromium layer formed. Figure 16(a) shows a sample with no thermal treatment realized. Line scan does not show any considerable change in the chromium content on the interface of Crofer 22 APU and coating.

It became clear that when Crofer 22 APU is submitted to temperatures above 900°C a sensible chromium layer is formed figure 16(b). Increasing the thermal treatment temperature increases also the thickness of formed layer figure 16(c,d).

Although temperature of 1000°C or above promotes a better densification of the coating, it turn to be unsuitable to sinter and densify Co_2MnO_4 spinel coating on Crofer 22 APU. Above 1000°C the thickness of the formed layer can achieve 1 μm or more what is contrasting with the other requirements of the coating (i.e. high electrical conductivity, low chromium content on interface). Based on these results new approaches to lower the sintering temperature and to increase the density were done.

3.2. Synthesis of Co$_2$MnO$_4$ spinel powder

In addition to the properties already described in the previous chapter, the produced Co$_2$MnO$_4$ spinel powder must satisfy some requirements to be used as protective layer [28],[41],[42],[51],[58] like:

- Zero open porosity– to improve mass barrier effect;
- Compatible thermal expansion coefficient – to avoid cracks in the coating due to the thermal cycles;
- Low sintering temperature – to reduce chromium layer formation on the interconnector.

The phase to be obtained must be the spinel $A^{2+}B_2^{3+}O_4^{2-}$ [72] in order to guarantee the best electrical conductivity and barrier effect. Main compounds shall be cobalt and manganese; iron impurities are accepted because the material will coat stainless steel. There shall be no chromium impurities that could migrate to the cathode and deposit on the catalyst thus poisoning the fuel cell [46].

3.2.1. Production Methods

Some production methods were tested and evaluated regarding the obtained phases, specific surface area (that influences directly the sintering behaviour) and sinterability (sintering temperature and density). The obtained characteristics were compared to those of some commercial spinels. The obtained results were also used in the successive parts of the present research work.

3.2.1.1. Solid-state reaction

This method is probably the most widely used method for the preparation of polycrystalline solid-like powders [73]. It is a straightforward method to easily produce complex powder from mixtures of raw materials; on other hand, relative high temperatures shall be applied to the powder in order to achieve the desired structure [73],[74].

Thermodynamic and kinetic factors are very important in solid-state reactions: therefore high temperature must be applied to the mixture to promote inter-diffusion of atoms [73]. Since the kinetic of the process is very low, atoms need an input of very high amount of energy to gain mobility enough to break bonds and reform them to create a new structure or material. Very long time (many hours or days) are also often applied to

the reaction because even at high temperatures inter-diffusion is very low [73].

If thermally activated, atoms from one component migrate to the other to produce a new structure. The produced powder is strongly dependent on the characteristics of raw materials. Impurity in the raw materials will influence the final product by adding extraneous atoms to the structure thus creating obstacles to the powder mobility and even producing non-desirable phases [73]. Powder with high surface area reacts in shorter time and produces smaller final particles. When high temperatures are applied, larger particles are often yielded [73],[74].

In the present method, cobalt manganese oxide spinel was produced by mixing cobalt oxide (Co_2O_3) (12926, Sigma-Aldrich) and manganese oxide (MnO) (377201, Aldrich) at 1:1 molar ratio of raw oxides. The powder mixture was homogenized in ball milling for 48 h. The obtained mixture was calcined at 900°C for 24 h with heating rate of 10°C/min. The obtained powder was roughly ground in mortar and then in a Shaker-Mixer Turbula® for 24 h. Figure 17 shows a flowchart that explains the solid-state production method.
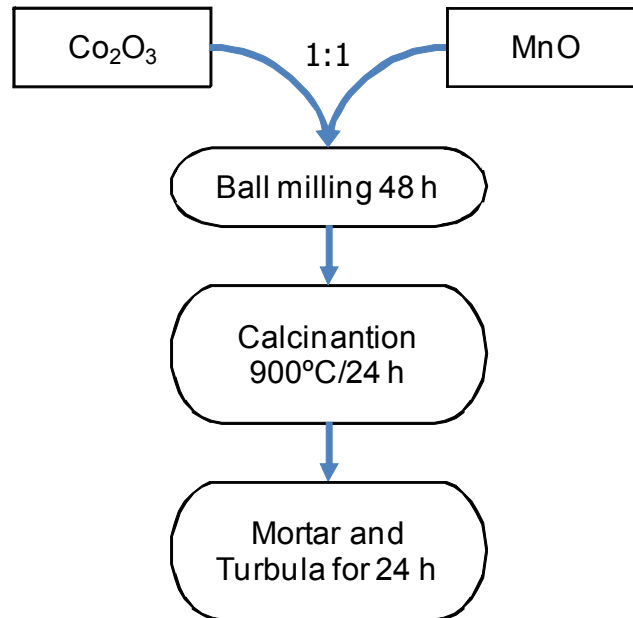
Figure 17 – Flowchart of production method solid-state reaction.

3.2.1.2. Gel-combustion

Many materials such as yttrium iron garnet, lanthanum nickel oxide perovskites and aluminates, among others, are produced by combustion methods [28],[74-76]. Gel-combustion method consists of a rapid oxidation of a fuel with large release of gases. The nitrates are the cations source for the reaction, whereas urea is used as fuel. A gelling agent such as ethylene-glycol is used to avoid solidification of the fuel, which makes the combustion more uncontrollable [75]. Combustion synthesis techniques are

relatively simpler and are more reliable route to synthesize complexes compounds in comparison with solid-state reaction because of the very simple setup and lower temperatures [28],[76].

Cobalt(II) nitrate hexahydrate ($Co(NO_3)_2 \cdot 6H_2O$) (36418, Alfa Aesar, 98%) was diluted in distilled water to obtain solutions with 3 M cobalt. In the same manner, manganese (II) nitrate hydrate, ($Mn(NO_3)_2 \cdot xH_2O$) (87848, Alfa Aesar, 99.98%) was diluted in distilled water to obtain solutions with 3 M Mn. The obtained solution of cobalt nitrate was mixed with the obtained solution of manganese nitrate with 2:1 Co/Mn molar ratio and stirred for 120 min at 60°C. Urea was slowly added to the stirring solution in the proportion of 4 times the sum of the nitrates moles [28],[76],[71]. The solution was heated to ~100°C and, with continuously stirring, kept for 4 to 6 h, until a viscous consistency was obtained. Ethylene glycol (0.33% with respect to total amount of solution) was added to the solution to jellify it. When the solution became a gel it was carried to a muffle furnace at 350°C and let combust. Gel-combustion method is illustrated in figure 18.
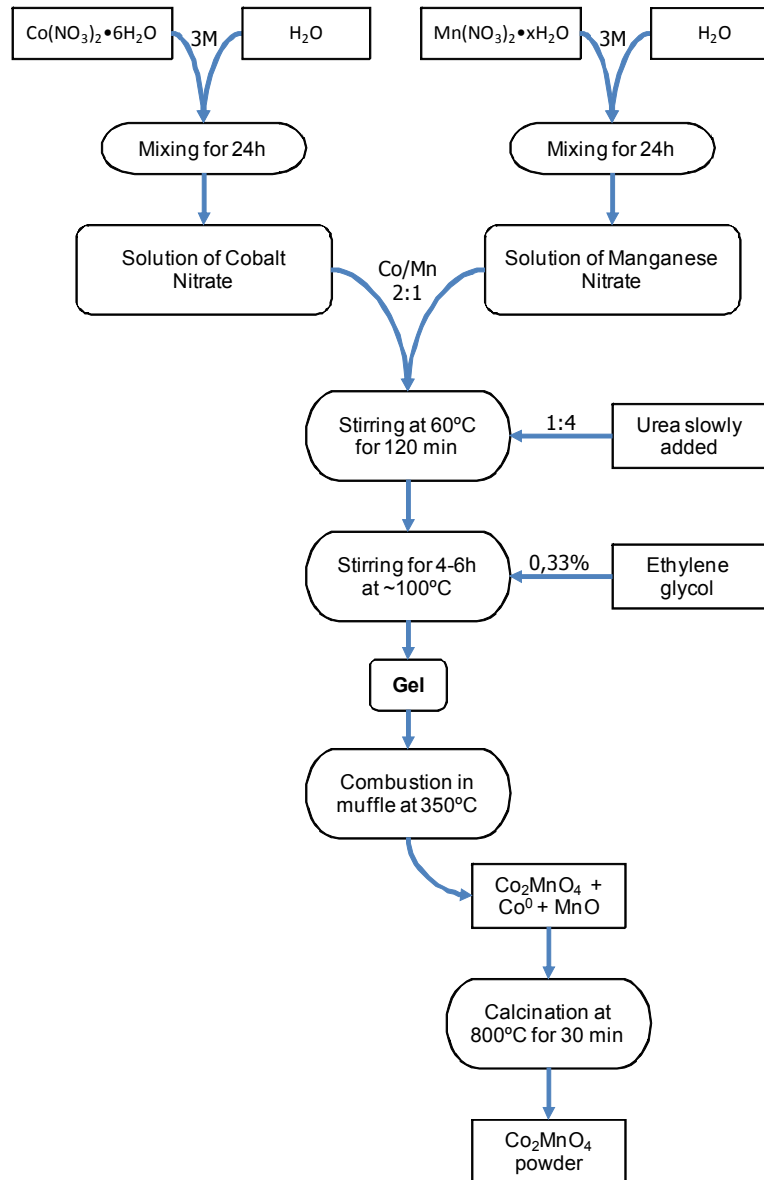
Figure 18 – Illustration of the gel-combustion method.

According to several authors [71],[77-81] the theoretically total combustion reaction is:

$$2Co(NO_3)_2 + Mn(NO_3)_2 + 12CH_4N_2O + 11O_2 \rightarrow$$
$$\rightarrow Co_2MnO_4 + 12CO_2 + 15N_2 + 24H_2O$$

(1)
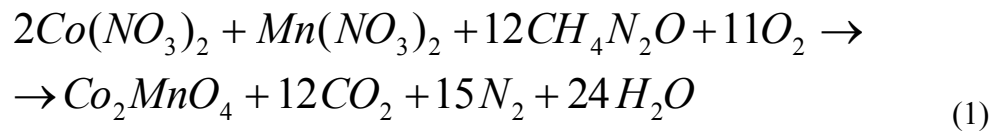
There is a large increase in volume when compared to the original volume of liquid. Because the by-products of the reaction are inert gases in water, the method is also environmental friendly. Equation 1 shows that there is a large amount of escaping gas denoting the combustion of the reactants. Because of the large amount of escaping gases the obtained product formed has the appearance of a foamy ceramic with a porous network and no mechanical resistance; therefore, it crawled right after the synthesis and was easily ground with a mortar. Since the obtained product had still some metallic cobalt and excess of manganese oxide after production, the powder was calcinated at 800°C to oxidize the remaining metallic part and conclude the reaction. This process is also illustrated in the figure 18. After calcination the powder was ground in a Shaker-Mixer Turbula[®] for 2 h.

3.2.1.3. Co-precipitation

Co-precipitation method was used to produce activated cobalt manganese oxide [73],[82]. By using co-precipitation method it is possible to achieve high degree of homogenization on mixing; an intimate contact between the grains of reactants are built, this will allow to produce small particle sizes and also speed up the reaction rate of the process [73].

Precursors of high reactivity were used in order to obtain fine particles, which could sinter at lower temperatures. Manganese nitrate was used as precursor and cobalt oxyhydroxide (CoOOH) was synthesized according to [82],[83].

In order to synthesize cobalt oxyhydroxide, cobalt(II) sulfate heptahydrate ($CoSO_4 \cdot H_2O$) (C6768, Sigma-Aldrich, ≥99%) was firstly diluted in water and stirred at 60°C. Sodium hydroxide (NaOH) (S5881, Sigma-Aldrich, ≥98%) 1M was added to the previous solution and stirred for 30 min. Hydrogen peroxide (H_2O_2) (500ml) was added drop wise to the whole solution that was kept for 6 h at pH 4. The resulted suspension was filtered, washed and dried [82]. The synthesis of cobalt oxyhydroxide is showed in figure 19.
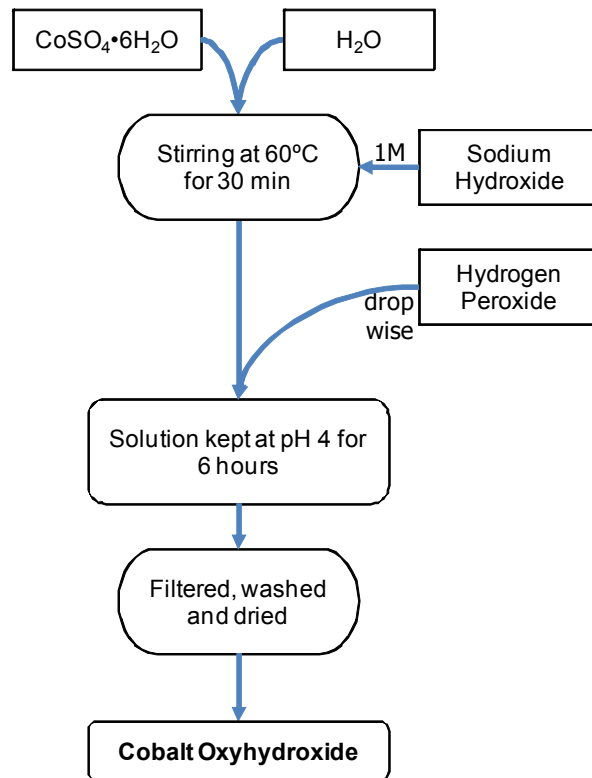
Figure 19 – Cobalt oxyhydroxide production method.

The resulting cobalt oxyhydroxide was mixed with manganese (II) nitrate hydrate, $(Mn(NO_3)_2 \cdot xH_2O)$ – 99,98%, 87848, Alfa Aesar – in distilled water; the pH was adjusted to 4 using nitric acid. The solution was evaporated in water bath for 3 h then calcinated in muffle furnace at 250°C for 2 h. Low calcination temperature is possible due to the high reactivity and small particle sizes of the production process [73]. The resulting cobalt

manganese oxide was ground in a ball milling for 24 h [83]. Figure 20 show the co-precipitation process flowchart to better understand the process used.

```
┌─────────────────────────┐      ┌─────────────────────────┐
│   Cobalt Oxyhydroxide   │      │   Mn(NO₃)₂•xH₂O         │
└─────────────────────────┘      └─────────────────────────┘
                                     ┌──────────────────┐
                                     │   Nitric Acid    │
                                     └──────────────────┘
              ┌──────────────────┐        adjust pH
              │  Water solution  │
              │      pH=4        │
              └──────────────────┘
              ┌──────────────────┐
              │  Evaporation in  │
              │ water bath for 3h│
              └──────────────────┘
              ┌──────────────────┐
              │  Calcination at  │
              │ 250ºC for 2 hours│
              └──────────────────┘
              ┌──────────────────┐
              │    Co₂MnO₄       │
              │     powder       │
              └──────────────────┘
```
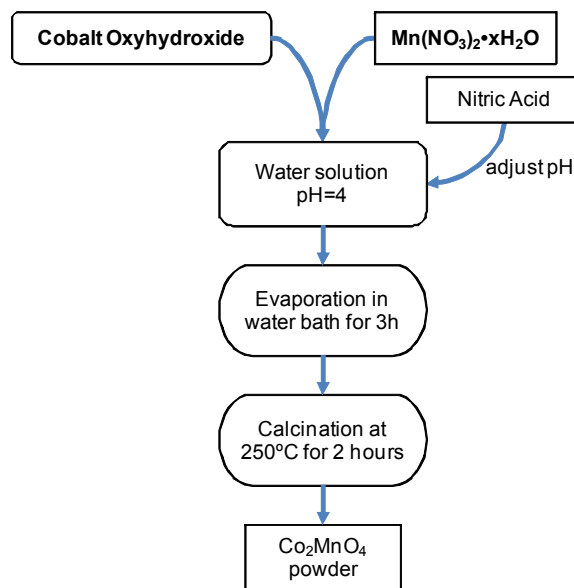
Figure 20 – Co-precipitation process flowchart

3.2.1.4.   Reverse Micelle

Reverse micelle consists in spheroidal aggregates produced when a surfactant is dissolved in an organic solvent [84-86]. The reverse micelles are produced by rapid agitation of the surfactant and the organic solvent [86]. Initially a 0,5 M microemulsion of AOT (Dioctyl sodium

sulfosuccinate) (Aldrich, 98%) in η-heptane (Sigma-Aldrich, HPLC grade) was prepared. To avoid precipitation of undesired compounds, a solubility products table was consulted and the most suitable reactant salts to produce Co_2MnO_4 were metal sulfates.

A saturated aqueous solution (Solution I) of reactant salts – cobalt (II) sulfate heptahydrate (C6768, Sigma-Aldrich, 99%) and manganese (II) sulfate monohydrate (M7634, Sigma-Aldrich, 99%) – is produced. A second solution of precipitating agent (Ammonium hydroxide solution, 5.0N, NH_4OH, 318612, Fluka) in water is also produced. The solution of reactant salts and the solution with precipitation agent are mixed, separately, with the microemulsion (AOT in η-Heptane) and left in ultrasound bath for 10 min. Resulting microemulsions were reactant salts within the reverse micelle (microemulsion I) and precipitating agent within the reverse micelle (microemulsion II). The two produced microemulsions were mixed together under strong constantly stirring for 10 min. Due to Brownian motion both reverse micelle types collide to each other and mix their content resulting in reverse micelles with reactant salts and precipitate agent. After the stirring, ethanol was added to the resulting microemulsion to extract the organic solvent and the surfactant by breaking the micelles. The suspension was centrifuged to extract the solid precipitated. The result was an amorphous and contaminated powder of Co_2MnO_4 spinel and surfactant+organic solvent. The powder was filtered and washed with ethanol until it became

free of surfactant. Figure 21 shows the flowchart of the spinel production by reverse micelle method.
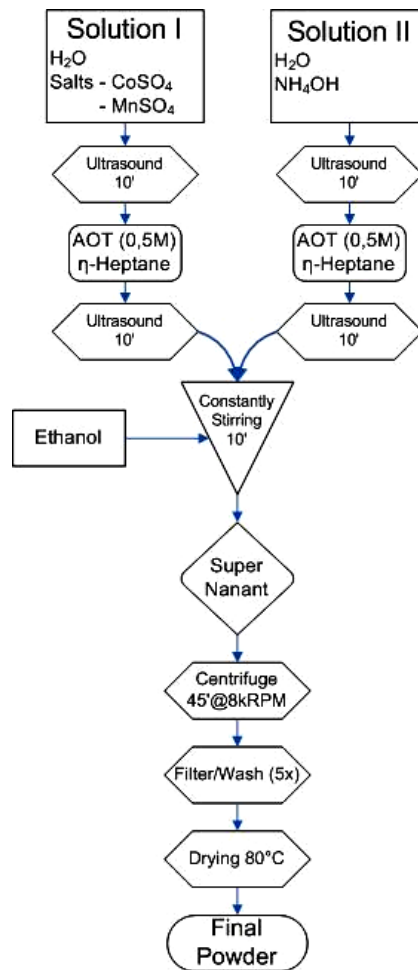
Figure 21 – Flowchart of the reverse micelle production procedure.

To assure the oxidation reaction of the powder, hydrogen peroxide was added to the powder after the production. No calcination was realized with this material to avoid particle growth and/or pre-sintering.

3.2.1.5.   Commercial powders

When this project was started there were no available Co_2MnO_4 spinel commercial powders at industrial scale; only some powders sample were available. By the time the project ran, various producers took the line for the production of Co_2MnO_4 spinel. Commercial powders were used as comparison standards for the self-produced materials. The produced materials were compared with two available commercial Co_2MnO_4 spinels. Spinel from the producer A, HC Stark, Germany, had SSA=3,2 m^2g^{-1}, particle size of d_{50}=1,12 μm and commercial price is around 350 EUR/kg [catalogue producer A]. Spinel from the producer B, Seimi, Japan, had SSA=20,2 m^2g^{-1}, particle size of $d_{50} \geq 0,50$ μm and commercial price over 500 EUR/kg [catalogue producer B]. Table 6 shows the data of commercial spinel to easy comparison between them.

Table 6 – Details on the properties of commercial spinel.

	SSA [m^2g^{-1}]	d_{50} [μm]	Cost [€/kg]
Producer A	3,2	1,12	350
Producer B	20,2	≥0,50	500

3.2.2. Discussion

3.2.2.1.   Solid-state reaction

Spinel powder produced by solid-state reaction presented specific surface area by BET of 0,8 m²/g, particle size of d_{50}=16 µm and homogeneous structure. These data show that cobalt manganese oxide spinel produced by solid-state reaction presented properties unworthy for the scope of this work, which is to produce dense layer at lowest temperature possible. Table 7 shows a comparison between some properties of the produced spinel and the commercial spinels. It is clear that the specific surface area of solid-state spinel is much lower than commercial. In addition, obtained particle size is much greater for the solid-state powder, at least one order of magnitude bigger.

Table 7 – Comparative data of solid-state reaction powder and commercial spinels.

	SSA [m^2g^{-1}]	d_{50} [µm]
Solid-state powder	0,8	16
Producer A	3,2	1,12
Producer B	20,2	≥0,50

Figure 22 shows SEM image of the powder produced by solid-state reaction; this micrograph confirms the data shown in the Table 7 and shows a dispersed particle size distribution.
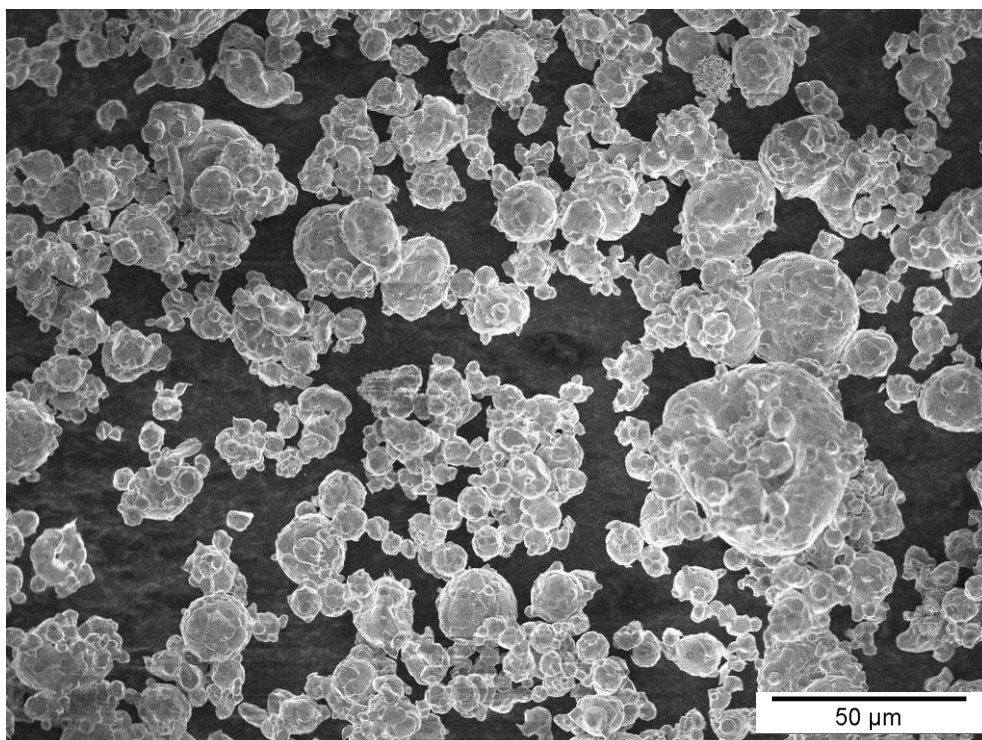
Figure 22 – Micrograph of a solid-state reaction produced powder.

XRD analysis showed that solid-state reaction effectively produced spinel phase from two raw oxide powders. The obtained powder was single Co_2MnO_4 phase as shown in figure 23.
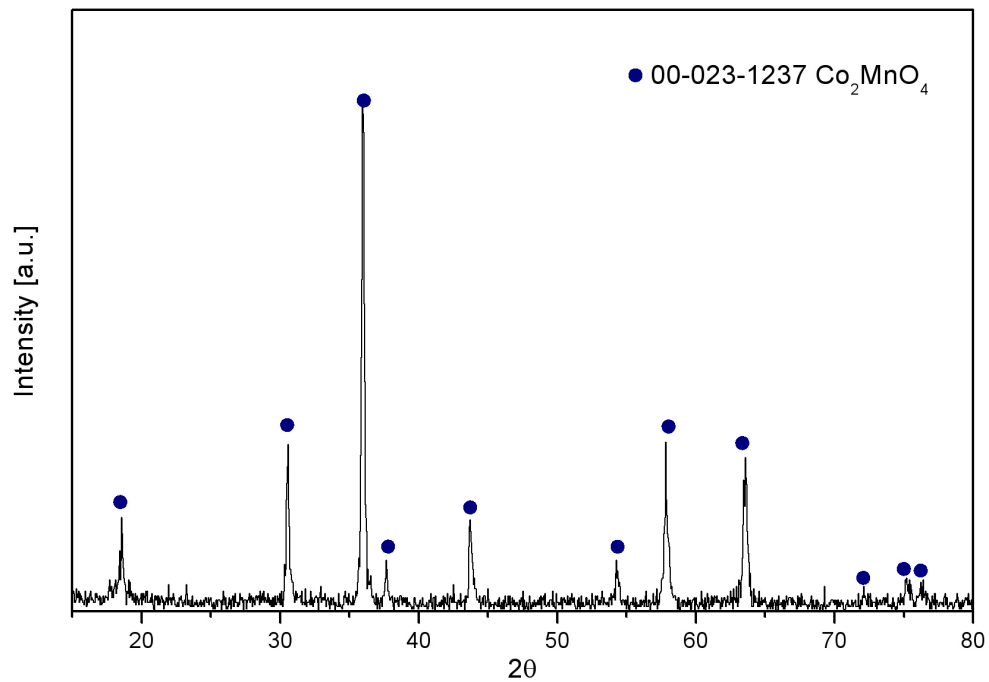
Figure 23 – X-ray diffraction pattern of solid-state reacted spinel.

Sintering behaviour has evaluated by optical and/or contact dilatometry and SEM analysis. Dilatometric curve is show in figure 24 and shows a relatively very high sintering temperature ~1100°C for the powder produced by solid-state reaction method; a limited densification is also noted in the same figure. The high sintering temperature drives the materials produced by this method to be not suitable to be used as barrier coating for SOFC interconnects.
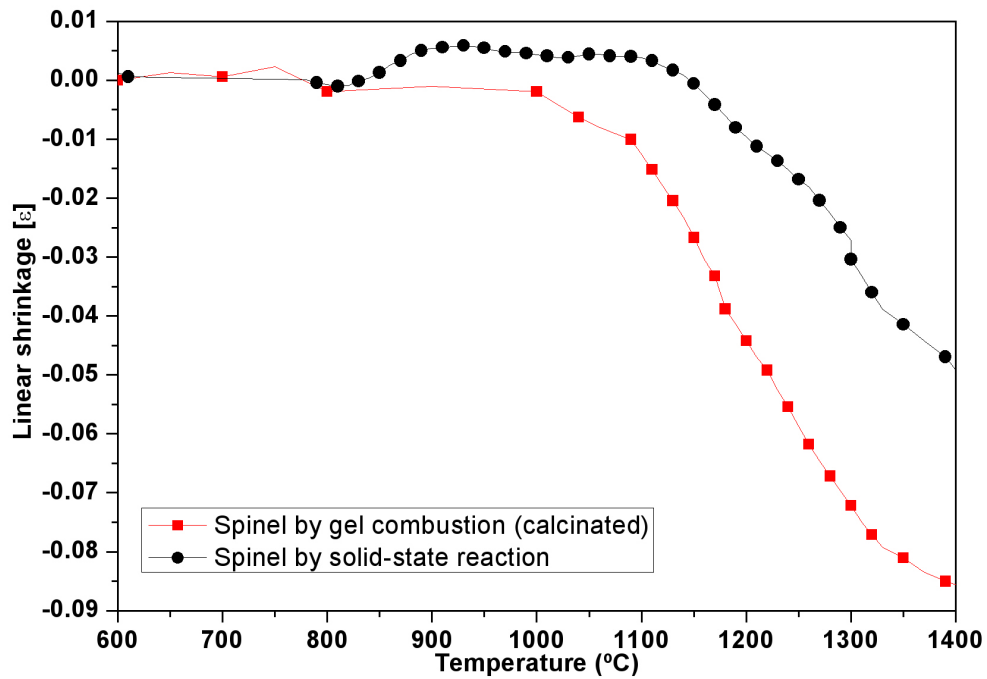
Figure 24 – Sintering behaviour of solid-state production method.

SEM image of the sintered spinel sample produced by solid-state method, (Figure 25) shows high porosity trapped within the sample after sintering at 1400°C. Pores appear to be much interconnected and with larger size. Remaining porosity makes this sample unsuitable to be used as barrier coating.
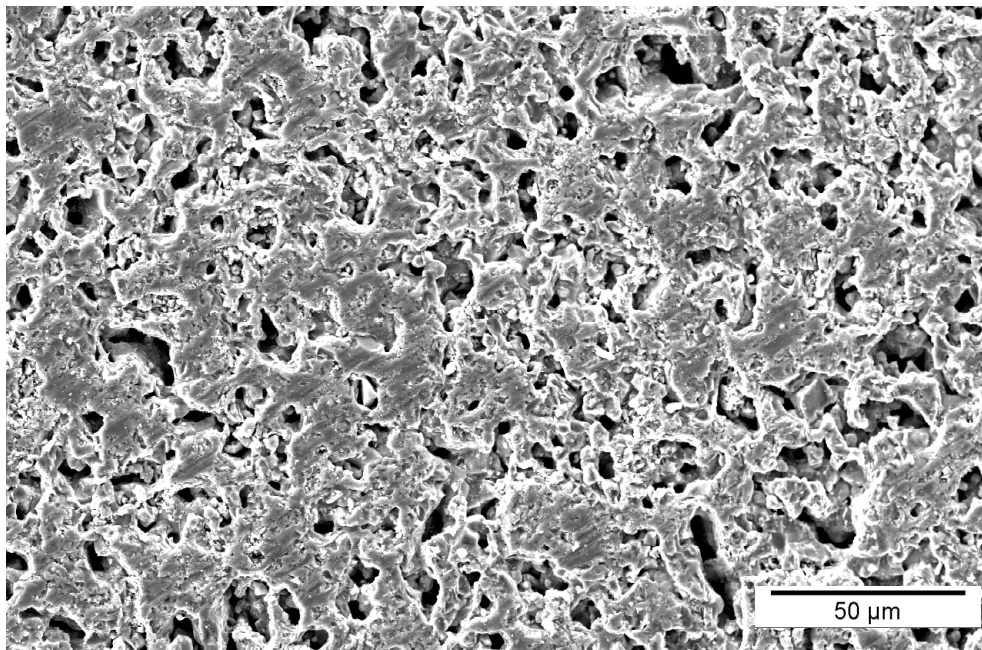
Figure 25 – SEM micrograph of sintered sample from solid-state production method.

Although the solid-state reaction produced spinel with desired phase characteristics, its sintering behaviour was not good enough because even at high temperature high porosity remains in the material. Furthermore, sintering temperature is relatively high when compared with commercial or more technological methods.

3.2.2.2. Gel.combustion

Gel-combustion powders presented a highly porous structure. This is due to the gas outlet during the synthesis. Figure 26 shows a SEM micrograph of gel-combustion powder as produced.
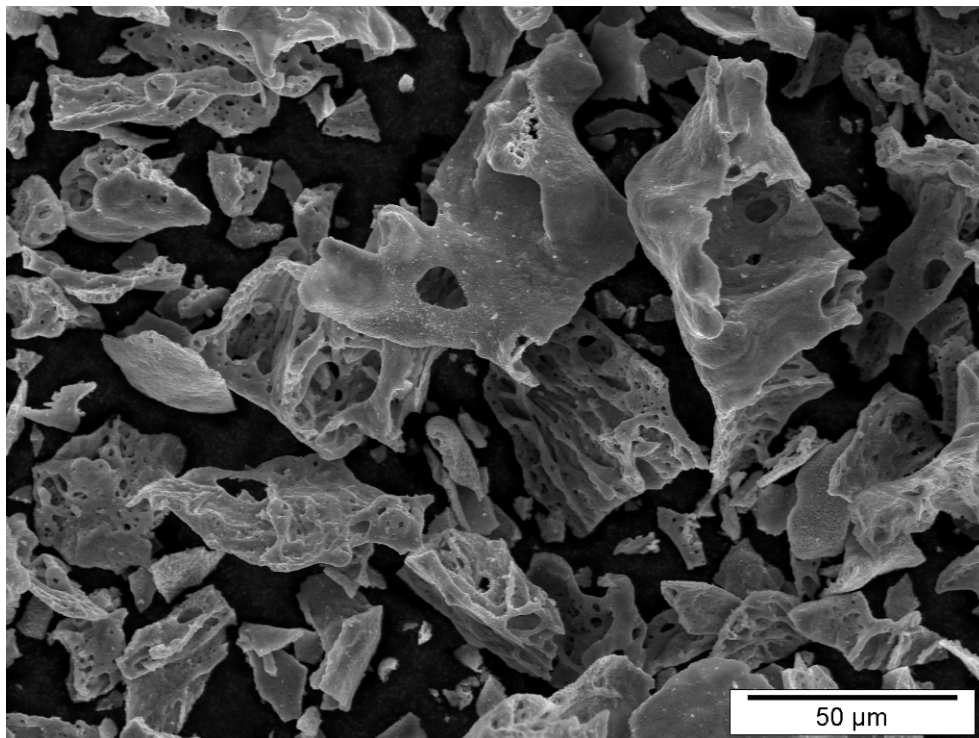
Figure 26 – SEM micrograph of gel-combustion as produced powder.

Powder particles had irregular shapes with particle size of roughly d_{50}=40 μm, before any treatment. Specific surface area measured by BET was 11,5 m²/g. Table 8 shows a comparison between some properties of the spinel powder produced by gel-combustion method and the commercial ones.

Table 8 – Comparative data between gel-combustion powder and commercial spinels.

	SSA [m^2g^{-1}]	d_{50} [μm]
Gel-combustion powder	11,5	~ 40 (as produced)
Producer A	3,2	1,12
Producer B	20,2	≥0,50

The high specific surface area can be explained by the high gas release in the gel-combustion process that produces very porous structure with high specific surface area and no defined shape, at first the material was a spongy structure with virtually no mechanical resistance.

X-ray diffraction pattern of "as produced" (no calcination) and calcinated gel-combustion powder are shown in figure 27. Because the gel-combustion process promotes the combustion of nitrates the result material can be partially reacted. Thermodynamically speaking, manganese oxide has higher Gibbs free energy variation if compared with cobalt oxide. Not all the cobalt nitrate was combusted in the reaction and some of the cobalt remained as metallic cobalt. Therefore, it is possible to observe in the plot (Figure 27-a)

some remaining amount of metallic cobalt and the excess of manganese oxide that will be converted to spinel oxide during the calcination process. Throughout the calcination process more energy is given to the system, this allowing the remaining cobalt to react with manganese oxide and form Co_2MnO_4 spinel. It is possible to observe in figure 27-b that after calcinations the produced phase is Co_2MnO_4, as predicted.
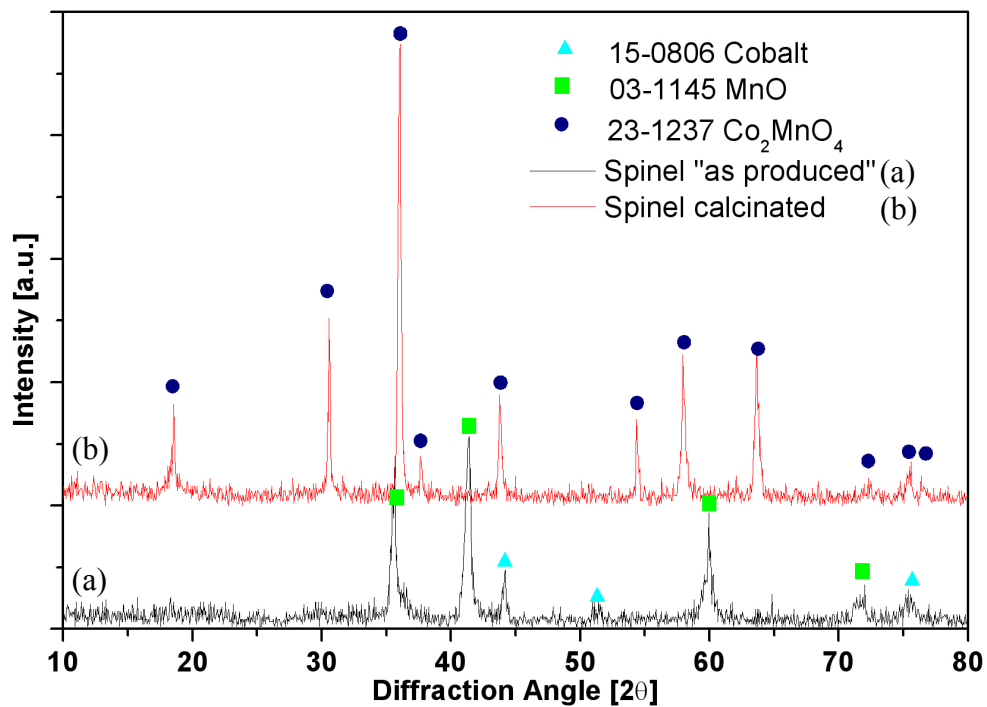
Figure 27 – X-ray diffraction pattern of gel-combustion method "as produced" and calcinated

Sintering behaviour of spinel is showed in figure 28. One can see that the sintering behaviour is quite similar to that corresponding to the powder produced by solid-state reaction. It is supposed that such similar behaviour can be associated to the similar specific surface area and chemical stability of spinel powders.
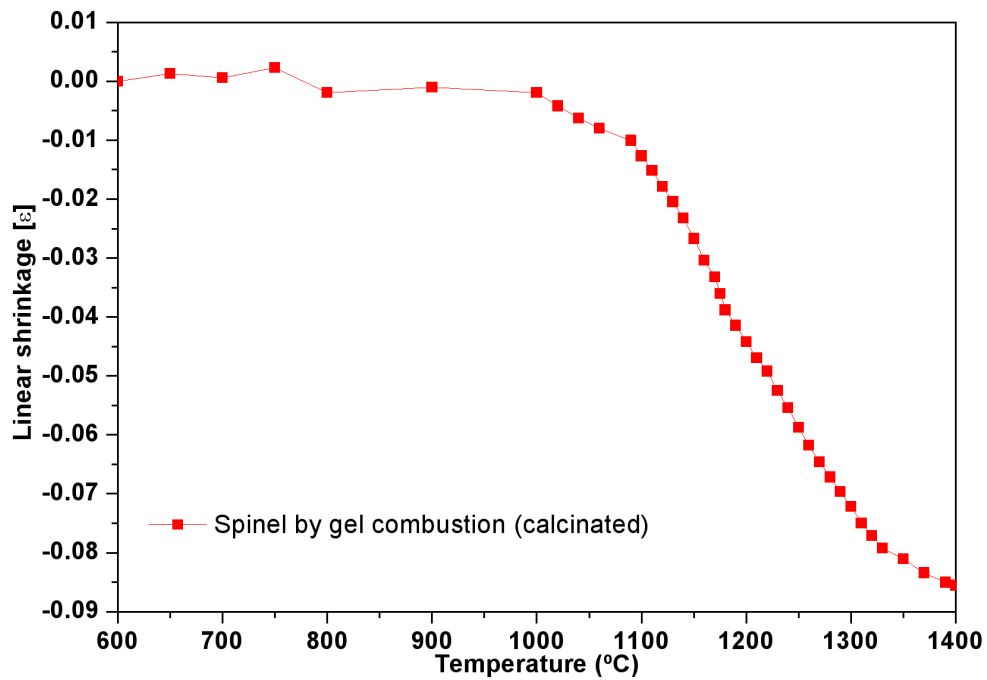
Figure 28 – Sintering behaviour of the spinel produced by gel-combustion method.

3.2.2.3.   Co-precipitation

Cobalt oxyhydroxide with high activity was successfully produced as showed in figure 29. The lower intensity peaks in the x-ray pattern of the cobalt oxy-hydroxide is reasonable because no calcination process is expected in the production method. Therefore, very small particle size of the material also contributed to the lower intensity of the cobalt oxyhydroxide peaks.
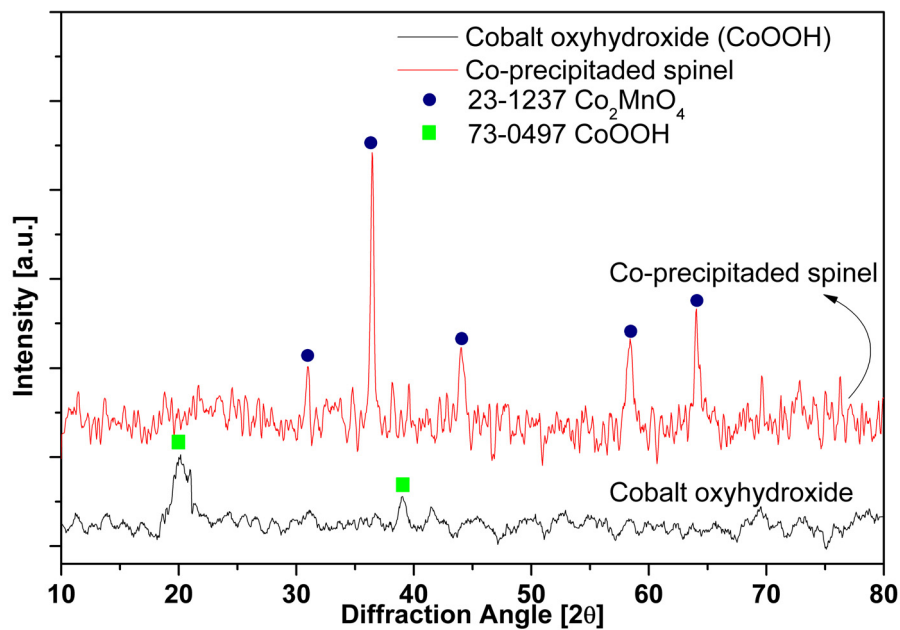
Figure 29 – X-ray diffraction patterns for cobalt oxyhydroxide and co-precipitated spinel.

Cobalt manganese oxide produced by co-precipitation method presented only the desired phase (Co_2MnO_4) as showed in figure 29. Also in the case of cobalt manganese oxide produced by co-precipitation method, the small particle size contributed to the lower peaks in the x-ray pattern.

Sintering behaviour and sintering temperature were analysed by dilatometry shown in figure 30.
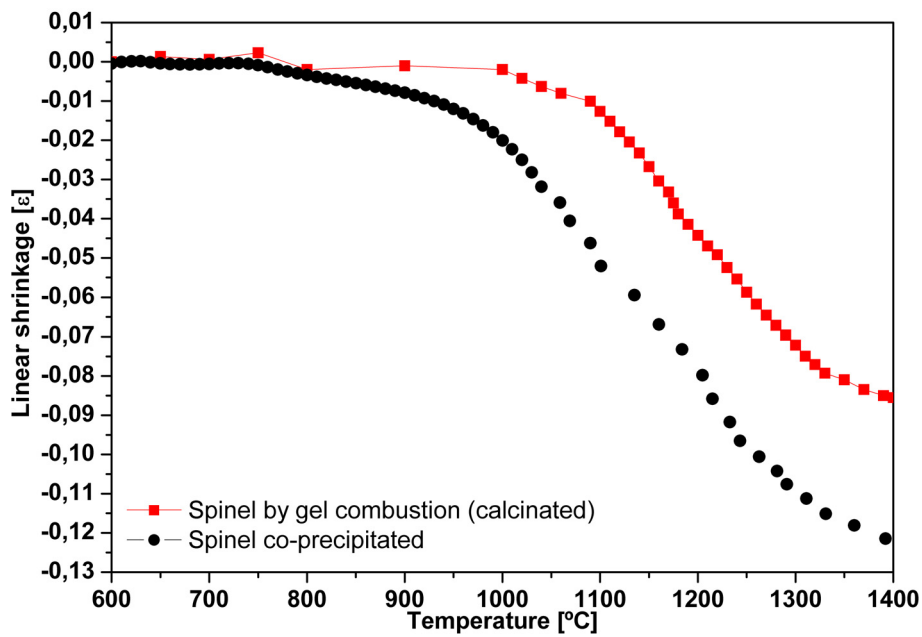
Figure 30 – Sintering behaviour of co-precipitated spinel.

It is possible to observe that sample produced by co-precipitation method possesses a sintering temperature of ~950°C. The very high specific surface

area (SSA=55 m^2g^{-1}) of the produced spinel can explain this sintering behaviour. Figure 31 shows SEM micrograph of the produced spinel powder. It is possible to see that the particles agglomerate very easily and tend to form agglomerates smaller than 50 µm. It is stated that the particle size produced by co-precipitation is smaller than 1 µm (Figure 31).
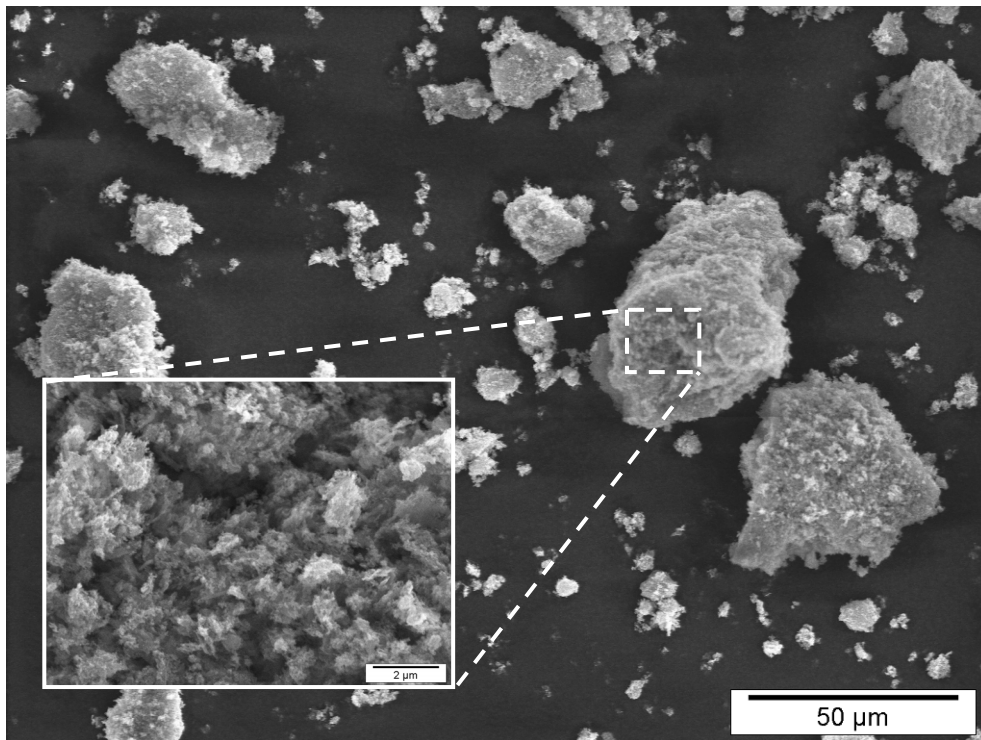
Figure 31 – SEM micrograph of the spinel powder produced by co-precipitation method.

3.2.2.4.   Reverse micelle

Spinel powder obtained by reverse micelle was the finest powder produced its specific surface area measure by BET was 65 m^2g^{-1}. X-ray diffraction of the reverse micelle powder showed that before any heat treatment i.e. calcinantion or sintering, the material is highly amorphous as one can see in figure 32(a).
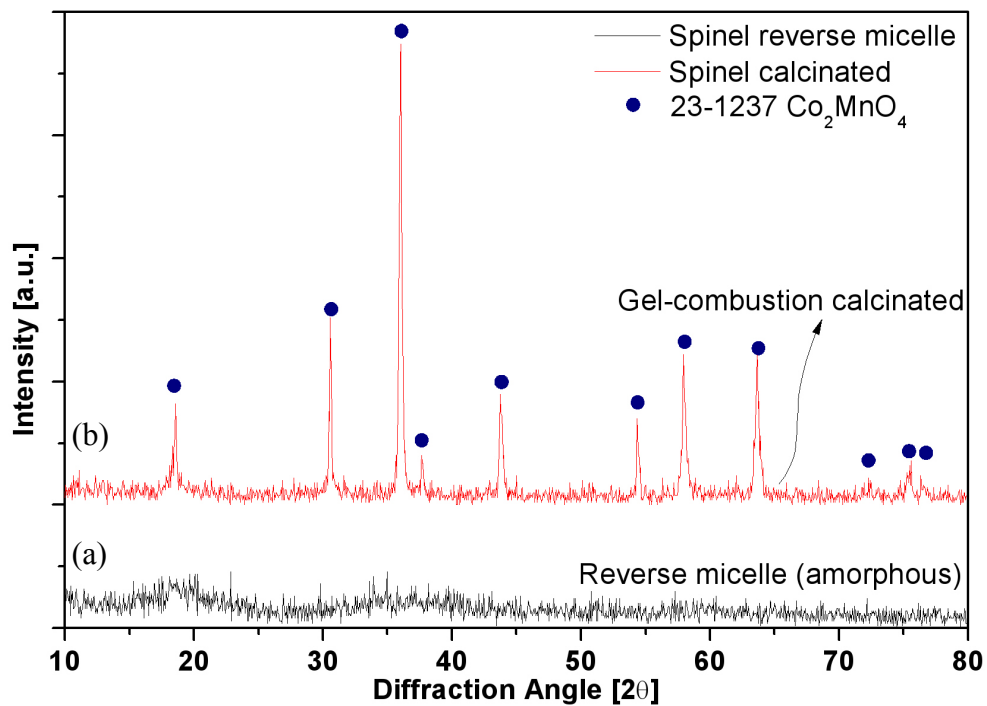
Figure 32 – X-ray diffraction pattern of reverse micelle spinel "as produced".

After the sintering process the reverse micelle material was again analyzed by x-ray diffraction to evaluate the resulting phase. It is supposed that the spinel by reverse micelle become well crystalline after the sintering process as shown in figure 33(a). It is possible to observe that other phases than pure Co_2MnO_4 appear. It is explained that above 950°C cobalt manganese oxide starts to decompose in complex phases of cobalt manganese oxide $[(Co,Mn)(Mn,Co)_2O_4]$ as well as cobalt oxides (CoO) [87].
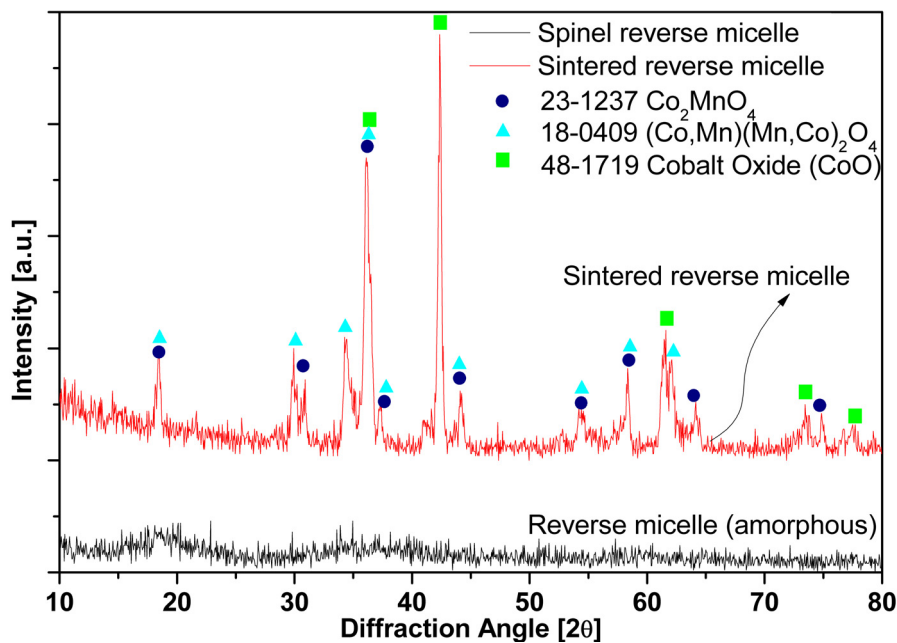
Figure 33 – X-ray diffraction of sintered reverse micelle spinel.

Sintering behaviour of reverse micelle was analyzed and dilatometric plot is shown in figure 34; one can observe that sintering temperature is much lower than the ordinary spinel. The shrinkage starts slowly from the beginning with an increase of shrinkage after 950°C. This behaviour is associated with the very high specific surface area and limited particle size of reverse micelle spinel powder.
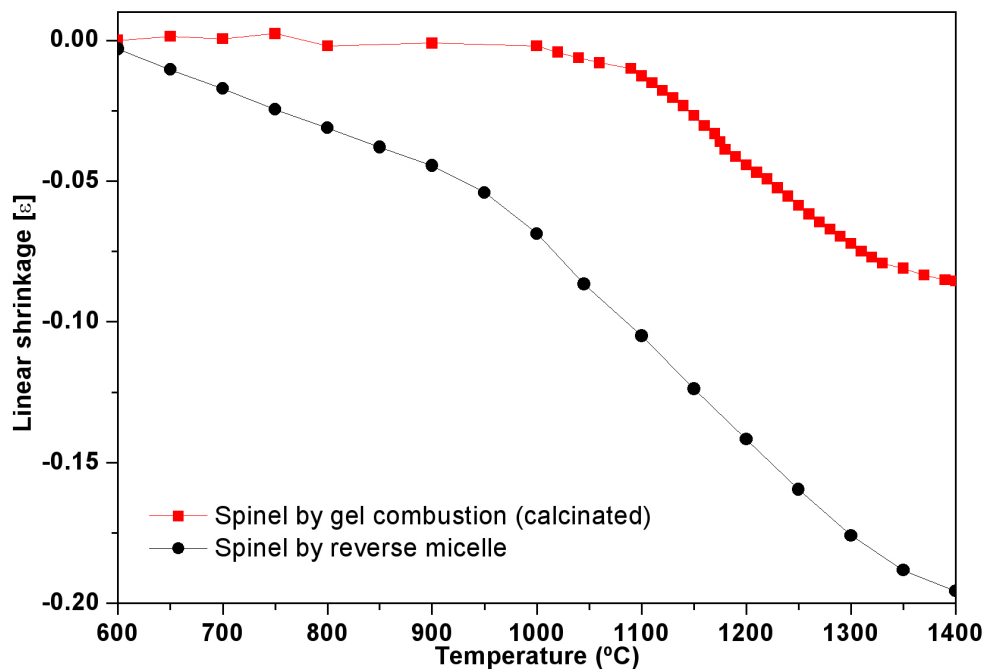
Figure 34 – Sintering behaviour of reverse micelle.

Figure 35 shows SEM micrograph of reverse micelle spinel powder. As well as the powder produced by co-precipitation, it agglomerates intensively. The agglomerates had irregular shape and size very variable but smaller than 60 μm.
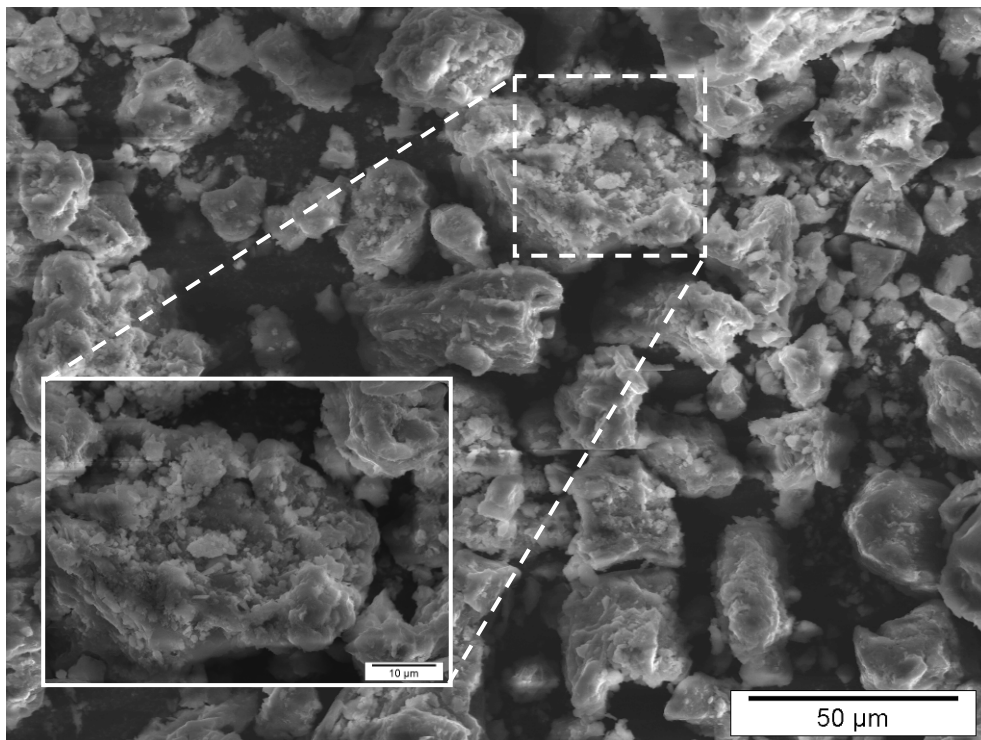
Figure 35 – SEM micrograph of non-sintered reverse micelle spinel.

3.2.2.5. Commercial spinel

Commercial spinel from producer A and B presented sintering behaviour as showed in figure 36. It is possible to observe the different trend of the sintering behaviour for the commercial spinel and the gel-combustion. Commercial spinels show reasonable lower sintering temperatures and faster shrinkage rate due to their very smaller particle size and very bigger specific surface area.
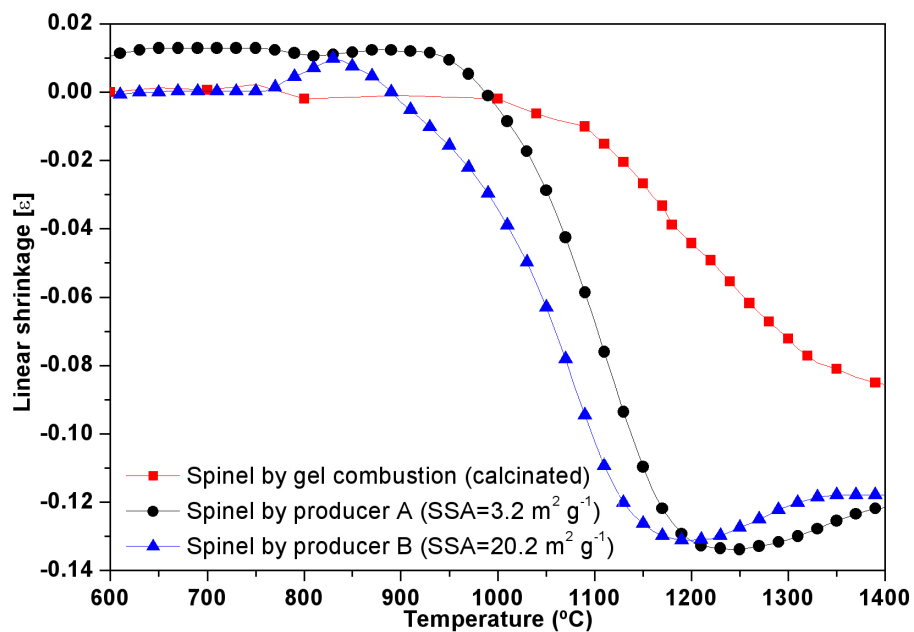
Figure 36 – Sintering behaviour comparison between gel-combustion and commercial spinels.

Sintering behaviour of the commercial spinel from producer B showed much low sintering temperature and much higher shrinkage when compared with producer A and other production methods.

It is possible to observe in figure 37 that spinel powder from producer A presents very homogeneous particle shapes (practically spherical particles) and the particles are highly porous.
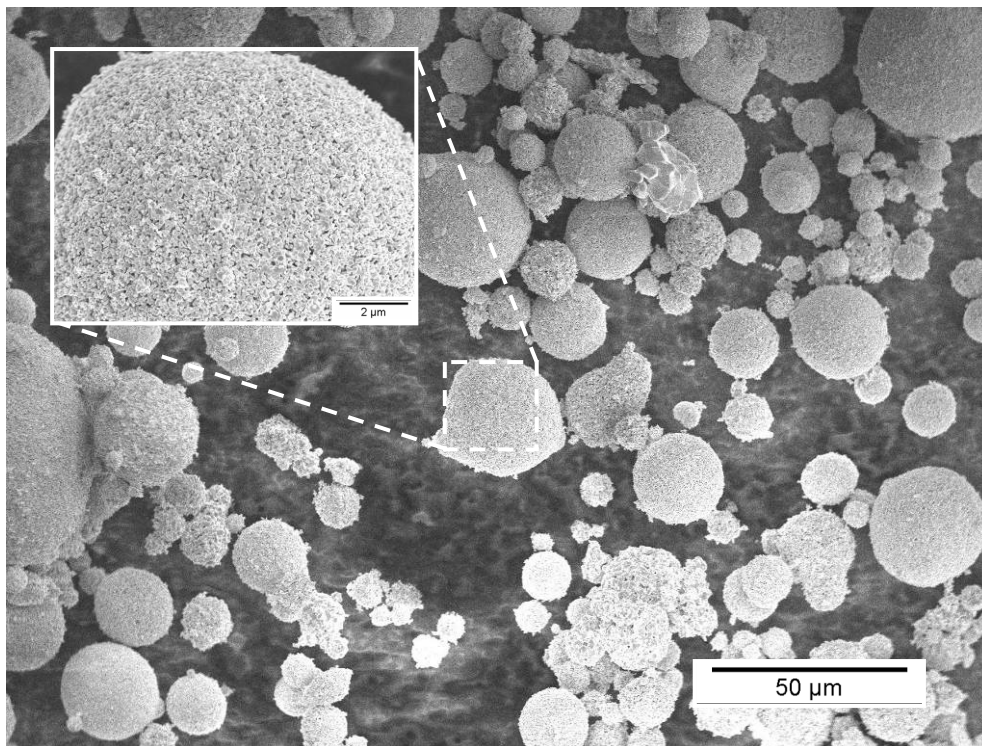
Figure 37 – SEM micrograph of spinel powder from producer A.

Similarly to what happens with reverse micelle and co-precipitation spinel, the material from producer B has a very small particle size and a very large specific surface area responsible for powder agglomeration. Figure 38 shows a micrograph of the spinel powder of the producer B.
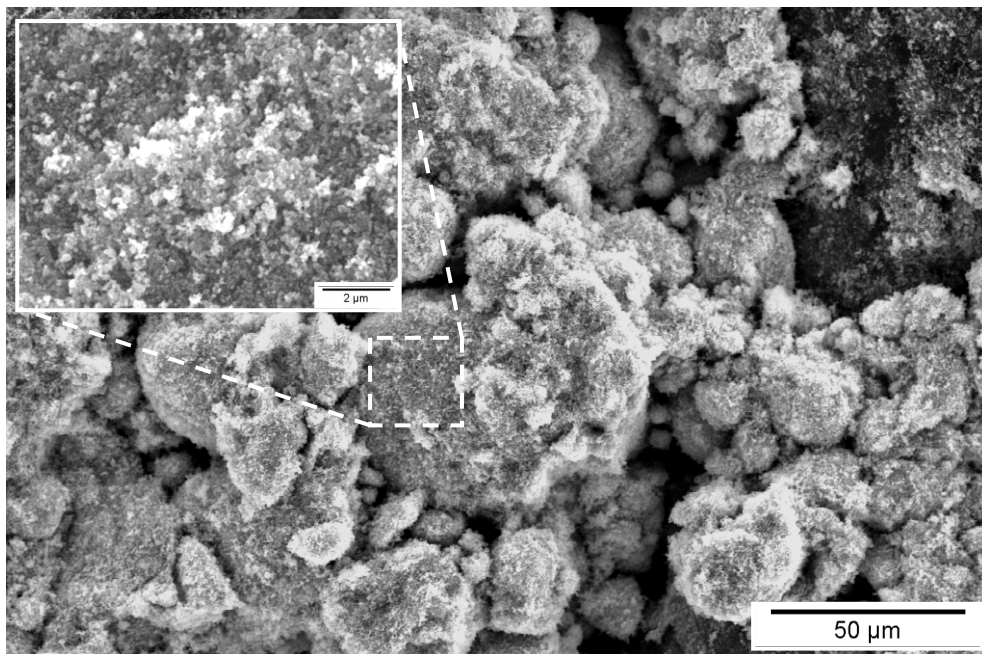
Figure 38 – Micrograph of spinel supplied from producer B.

3.2.3. Summary

Cobalt manganese oxide spinel was successfully produced by all method proposed (solid-state reaction, gel-combustion, co-precipitation and reverse micelle).

Each method promoted particular properties on the produced spinel, showed different complexities in the production and final cost for industrial application.

Solid-state method was the cheapest and less complex method but the properties achieved with the powder produced by this method did not satisfy the requirements of sinterability.

Gel-combustion method was reliable, relative simple, scalable and productive method to synthesize cobalt manganese spinel with acceptable results. With gel-combustion method was possible to produce reasonable large amount of powder at low cost and using common reactants.

Co-precipitation method produced high activated spinel with better sintering performance than gel-combustion but in detriment needed an intermediate step, production of cobalt oxyhydroxide, which made it more complex method.

Reverse micelle showed the best sintering behaviour, probably because the powder produced presented very large SSA. A disadvantage on this method was the more uncommon reactants, many intermediate steps and very low

productivity (many liters of reactants were needed to produce very few milligram of product).

3.3. Sintering aids for Co_2MnO_4 spinel

Sintering aids are widely used in a very broad range of materials and process. They can act by lowering the sintering temperature acting as catalyst for the diffusion process or forming liquid-phase that facilitate the diffusion and promote the shrinkage of particles [88].

Various promising sintering aids were attempted to improve the sinterability of Co_2MnO_4 spinel. The materials were chosen either by their similarity with the properties of Co_2MnO_4 spinel or by their previous use as sintering aids in other types of ceramics. Among the various materials tested as sintering aids, some of them showed interesting results to be presented here: antimony oxide (Sb_2O_3) doped tin oxide (SnO_2), iron copper oxide spinel (Fe_2CuO_4), niobium oxide (Nb_2O_5) and lithium fluoride (LiF). Each one was chosen because particular properties were noted, as described below.

Co_2MnO_4 powder (particle size ~10 μm), produced by gel combustion method (according to procedures described in the previous chapter) was first characterized in terms of chemical analysis, powder X-ray diffraction, specific gravity and specific surface area (by BET technique). Chemical analysis with ICP-AES showed the presence of cobalt, manganese and oxygen; the measured molar ratio of Co/Mn was 1,98. Specific gravity was 5,78 g cm^{-3}. Specific surface area measured by BET method was 3,3 m^{2}g^{-1}. Figure 39 shows X-ray pattern of the Co_2MnO_4 spinel powder.

Table 9 – Details of the precursor spinel used in this chapter.

Co/Mn	1,98
Density	5,78 g cm^{-3}
SSA	3,3 m^{2}g^{-1}.
d$_{50}$	~10 μm
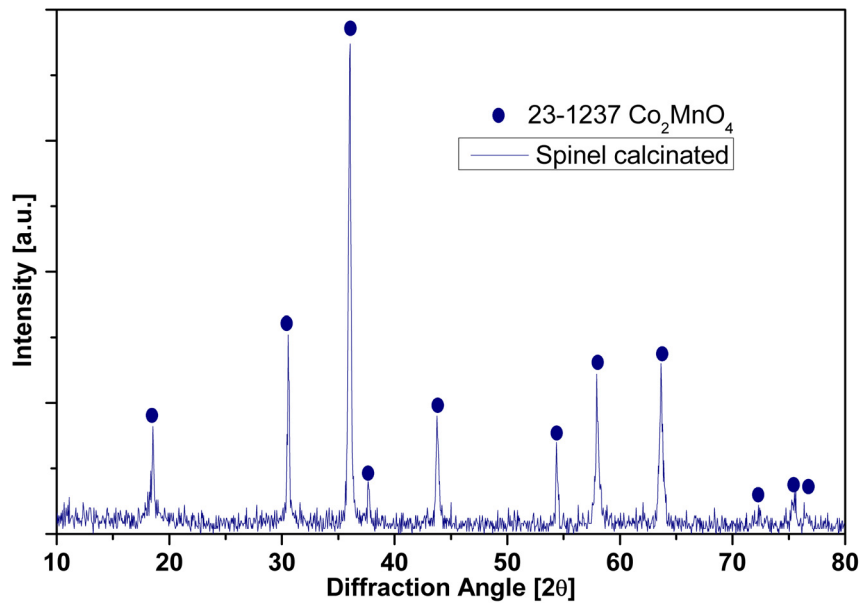
Figure 39 – X-ray diffraction pattern of Co$_2$MnO$_4$.

The spinel powder was mixed and homogenized with various sintering aids previously related (antimony oxide doped tin oxide, iron copper oxide spinel, niobium oxide and lithium fluoride). An agate mortar was used to ground and mix the powders. The resulting mixture was pressed into

circular pellets (13 mm diameter) with a pressure of ~280 MPa. Produced pellets were then subjected to dilatometric analysis.

The specimens were then analyzed with a dilatometer to evaluate at what temperature the sintering process occurs. After dilatometric analysis the samples were analyzed with SEM to evaluate the final microstructure.

3.3.1.1.   Antimony oxide doped tin oxide

Tin oxide is an intrinsic semiconductor with energy of band gap equal to 3,6 eV. After doping with 5-wt% of antimony oxide it gets new properties and is then called antimony doped tin oxide. Antimony oxide doped tin oxide (ATO) is a ceramic semiconductor with band gap of 0,14 eV and with the same structure of tin oxide (rutile-cubic). It has been previously used as conductive path in insulating glaze to generate heat by Joule effect in high-voltage electrical insulators [89].

ATO can form needle like σ phase that can act as sintering/densification aid; similar to what happen to aluminium oxide (Al_2O_3) when magnesium oxide is added (MgO) [90]. The principle is that the needle phase limits grain boundary mobility and avoids pore trapment [91-93].

Tin oxides were also studied in [51] and were reported to be good barrier against chromium evaporation/diffusion. In addition, indium doped tin oxide showed excellent electrical conductivity at low temperatures [51].

Based on that, tin oxide was studied as sintering aid for cobalt manganese oxide.

Antimony doped tin oxide was employed because it was easily available and its properties have been previously studied [89]. The antimony doped tin oxide was produced in the laboratory by solid-state reaction method according to [89].

X-ray diffraction analysis (Figure 40) showed only SnO_2 phase (PDF# 21-1250) for antimony doped tin oxide because at low doping level (smaller than 17%) the antimony is completely embedded in the tin oxide structure. Figure 40 shows x-ray diffraction pattern for antimony oxide and pure tin oxide for comparison purpose. The expected response of this doping on X-ray analysis would be a shift in the peaks position but it only happens when the doping is higher than 17%, as related in [89],[94].
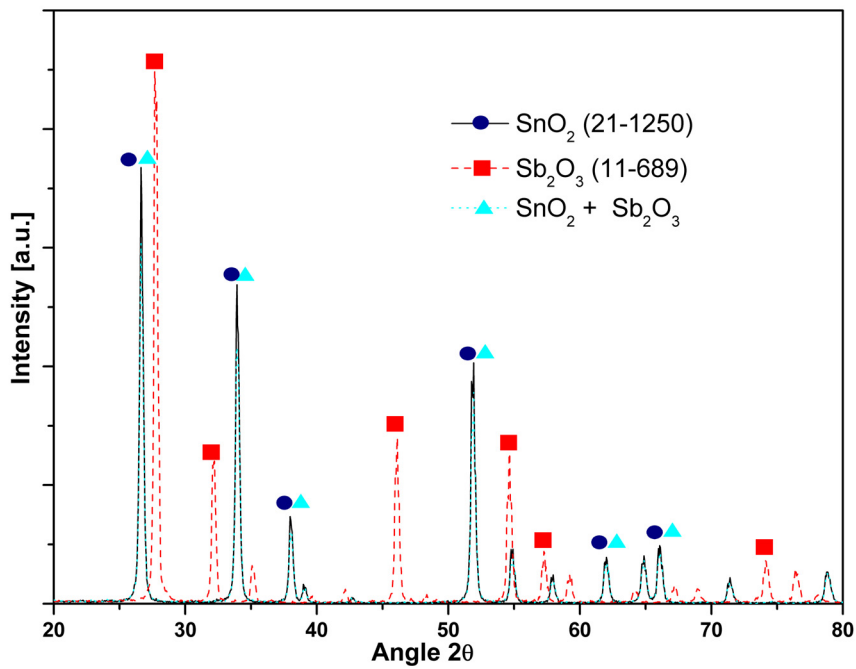
Figure 40 – X-ray diffraction of antimony doped tin oxide

3.3.1.2.   Iron Copper Oxide Spinel

The iron copper oxide spinel (Fe_2CuO_4) has the same (spinel) structure of cobalt manganese oxide but possesses lower melting and sintering temperature [95-98]. Some attempts have been done to use Fe_2CuO_4 directly as protective coating in SOFC. The drawback of Fe_2CuO_4 is that it

decomposes at high temperatures and has a very low melting point temperature as well [95].

Iron copper oxide material was synthesized in the same manner as the cobalt manganese oxide; by gel-combustion method using iron (III) nitrate nonahydrate (Fe(NO$_3$)$_3$•9H$_2$O) (31233, Sigma-Aldrich, ≥98%) and copper(II) nitrate hemi(pentahydrate) (Cu(NO$_3$)$_2$•2,5H2O) (12837, Sigma-Aldrich, ≥98%) as cations source, urea and ethylene glycol as fuel materials [95]. The production of iron copper oxide followed the same criteria and procedure used to produce cobalt manganese oxide, as explained in the previous chapter. The obtained powder was again a foamy shaped form with dark red-brownish colour.

Figure 41 shows the x-ray diffraction pattern for the produced iron copper oxide spinel. This analysis was carried out on the as produced powder, with no heat or chemical treatment. It is possible to observe that, in the same manner as cobalt manganese oxide, the produced iron copper oxide remains with some unreacted phases (metallic copper and iron oxide).
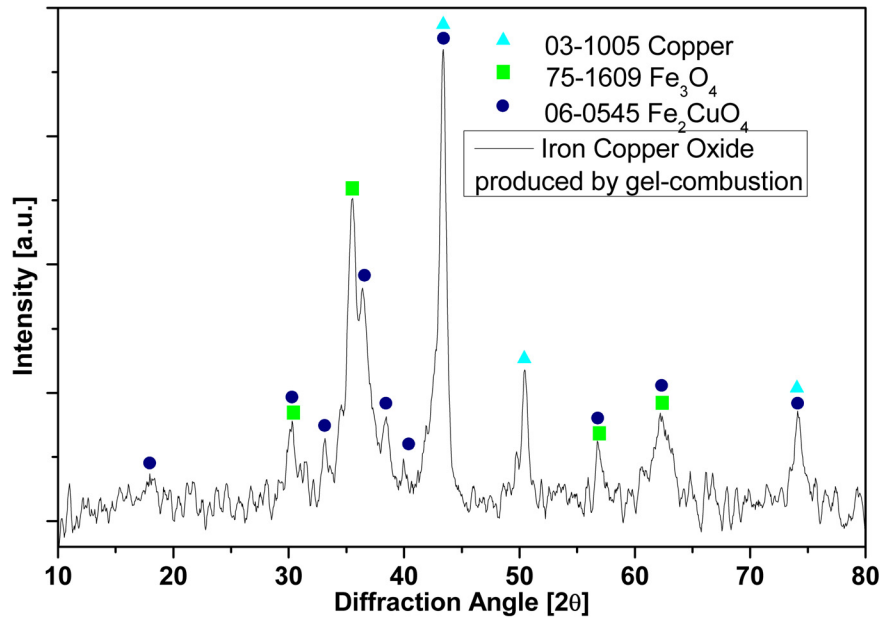
Figure 41 – X-ray diffraction of the produced iron copper oxide.

3.3.1.3. Niobium Oxide

Niobium oxide is commonly used as sintering aid in the ceramic community [99-101] as well as aid to increase materials conductivity [102],[103]. It is used as liquid-phase-sintering aid and can form liquid phases in the sintering process, which accelerats the sintering process by increasing atom mobility, diffusivity and therefore grain boundary mobility [99]. Commercially available niobium (V) oxide (Nb_2O_5) (208515, Aldrich, 99.9%) was mixed with pure cobalt manganese oxide and studied in this experiment.

3.3.1.4.   Lithium Fluoride

In addition, the use of lithium fluoride (LiF) as sintering aid promotes liquid-phase sintering that decreases the sintering temperature and increases the final density [104-107].

A disadvantage is the formation of a second phase created by the liquid that remains at the grain boundary. Liquid phase produced during the sintering could promote many different effects on the material. It could remain in small clusters located at the grain boundary (Figure 42(a), form a continuous film (Figure 42(b)) or segregate in one preferential direction (Figure 42(c)).

In the present work it is attempted to obtain behaviour like in figure 42(a) where the LiF phase remains in small clusters that will not interfere significantly with the conductivity of spinel. A continuous phase of lithium fluoride is disliked because lithium fluoride is a high electric insulating material. Since the use of Co_2MnO_4 spinel requires a high electric conductivity, the formation of continuous insulating phase would avoid the use of this material as conductive coating.
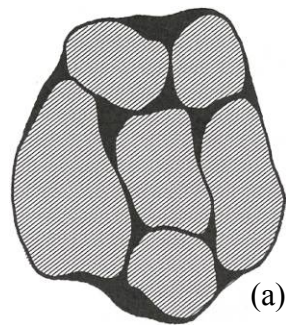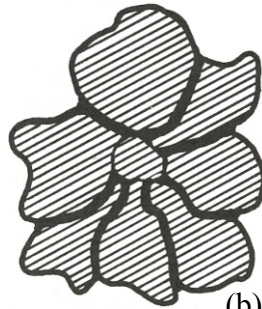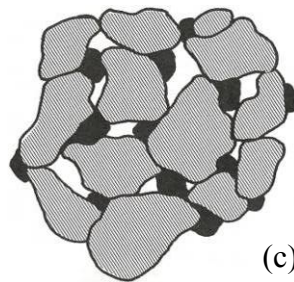
Figure 42 – Example of distribution of liquid on agglomerates[88].

3.3.2. Discussion

3.3.2.1.   Antimony oxide doped tin oxide

Regarding the use of antimony oxide doped tin oxide as sintering aid it was noted that its use produced very small highly dispersed pores that are visibly interconnected; for this reason it is not suitable to be used as barrier coating. Figure 43 shows the SEM micrograph of the cobalt manganese oxide with 5-wt% antimony doped tin oxide as sintering aid.
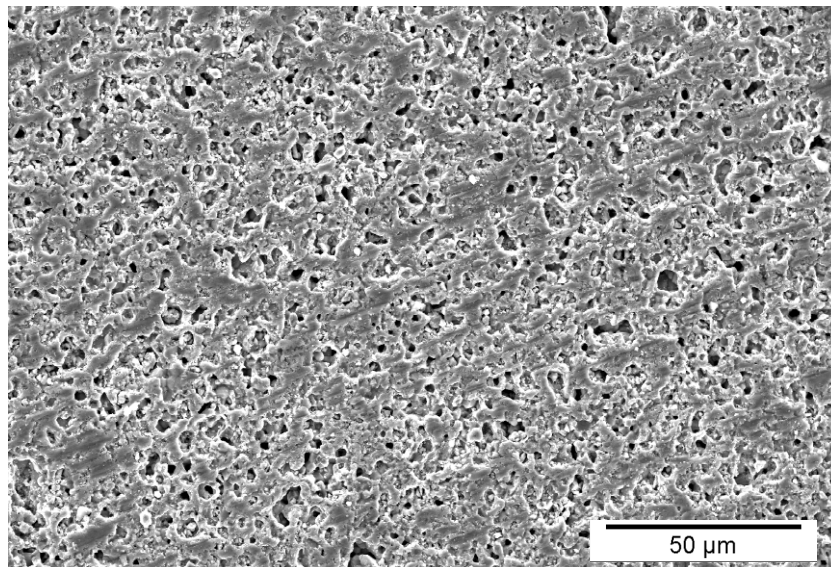
Figure 43 – SEM micrograph of Co2MnO4 with 5wt% ATO as sintering aid.

Dilatometric analyses (Figure 44) showed that the use of antimony doped tin oxide made the spinel to sinter faster but the sintering process starts at relatively higher temperatures. The spinel with antimony doped tin oxide showed high fine porosity. In spite of the high porosity, the material sintered with antimony doped tin oxide had high shrinkage when compared with other sintering aids.
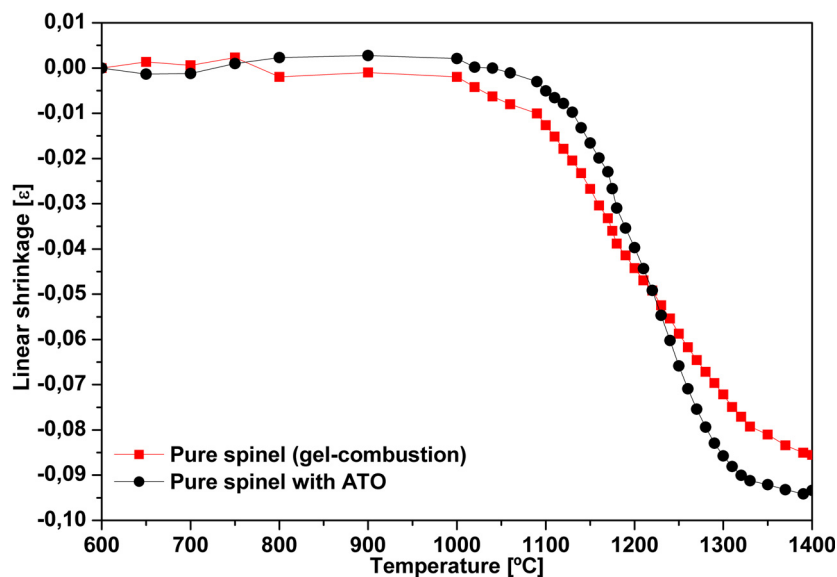
Figure 44 – Dilatrometric analysis of antimony doped tin oxide as sintering aid.

Figure 45 shows the shrinkage rate derived from the shrinkage plot in figure 44. One can observe that the sintering process starts around 1050°C (the

value was computed at the point the curve deviate from the horizontal axis, i.e., in other words, starts to shrink) for both materials.
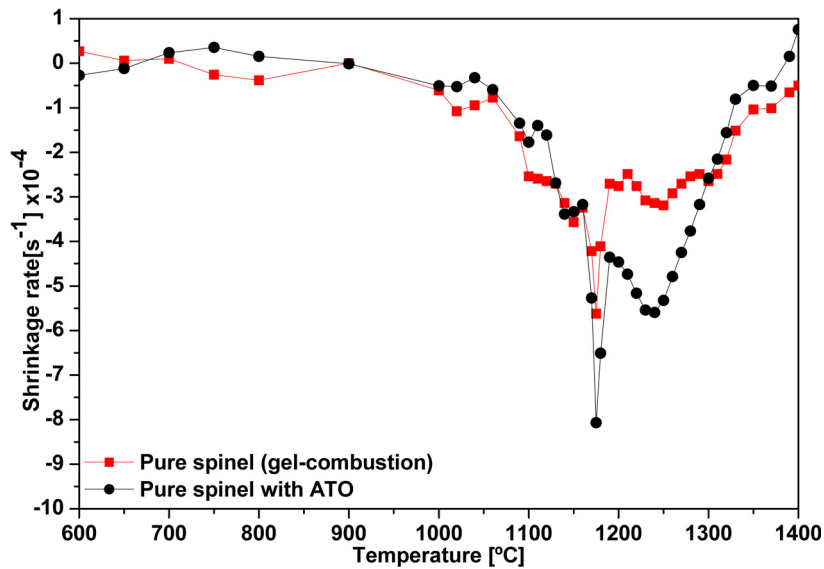
Figure 45 – Shrinkage rate of the spinel with antimony doped tin oxide

Pure spinel presents smooth and continuous shrinkage in contrast to spinel with ATO which shows the same behaviour of pure spinel until certain point when its shrinkage rate was increased abruptly. The reasons for the high shrinkage rate remain unclear and since a material with this high porosity is unlike for the purpose of our project, this behaviour was not further studied.

3.3.2.2.   Iron Copper Oxide Spinel

The spinel with iron copper oxide as sintering aid showed a microstructure with huge pores. Conversely, the solid part of the sample appears to be denser than any other. SEM micrograph of cobalt manganese oxide with iron copper oxide is shown in figure 46. The characteristic porosity is visible.
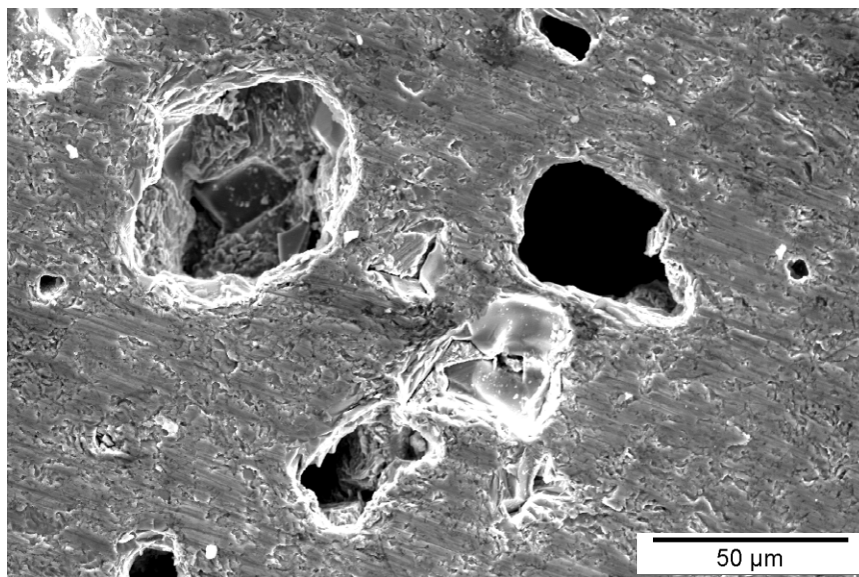
Figure 46 – SEM micrograph of the spinel sintered with iron copper oxide.

The shrinkage behaviour of iron copper oxide (Figure 47) was neither linear nor homogeneous because the sintering and melting point of iron copper

oxide is low ~1000°C. Therefore, a first expansion (probably due to the reaction of remained copper and iron oxide to form iron copper oxide spinel) occurs followed by a drop in the shrinkage caused by the melting of iron copper oxide. It is possible that with increase in temperature a gas released from iron copper oxide is generated and trapped into cobalt manganese oxide structure originating the huge pores shown in figure 46.
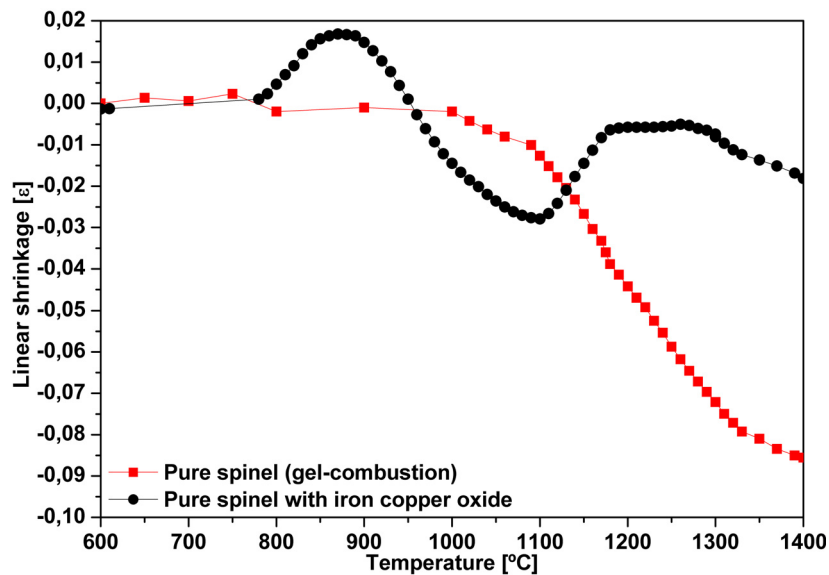
Figure 47 – Dilatrometric analysis of iron copper oxide as sintering aid.

The shrinkage rate of iron copper oxide matches its dilatometric trend, figure 48. All reactions occur at low rate compared with the sintering of

antimony doped tin oxide or pure spinel. The highest shrinking rate occurs at ~950°C which is close to the melting point of pure iron copper oxide.
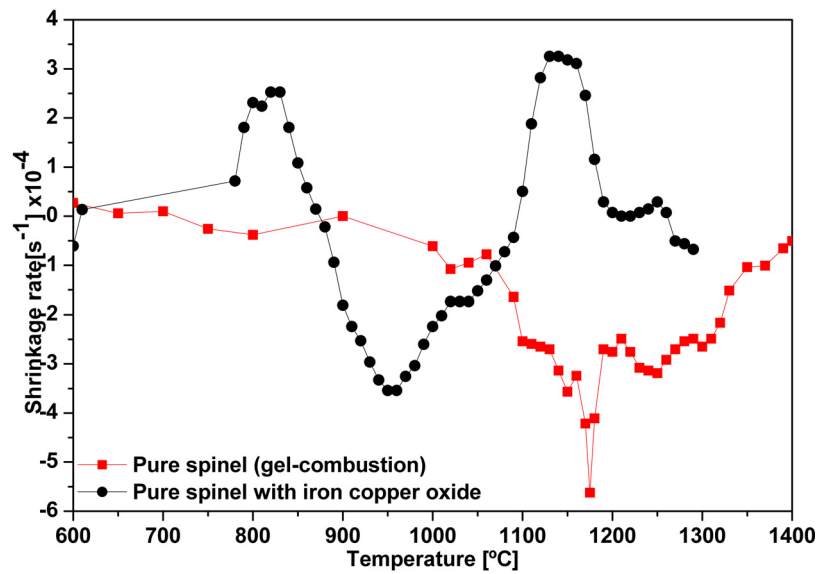
Figure 48 – Shrinkage rate of the spinel with iron copper oxide.

3.3.2.3.　　　Niobium oxide

Niobium oxide was very suitable to be used as sintering aid; the microstructure shown in the figure 49 shows high level of consolidation. It is possible to see some closed pores and a dense surface.
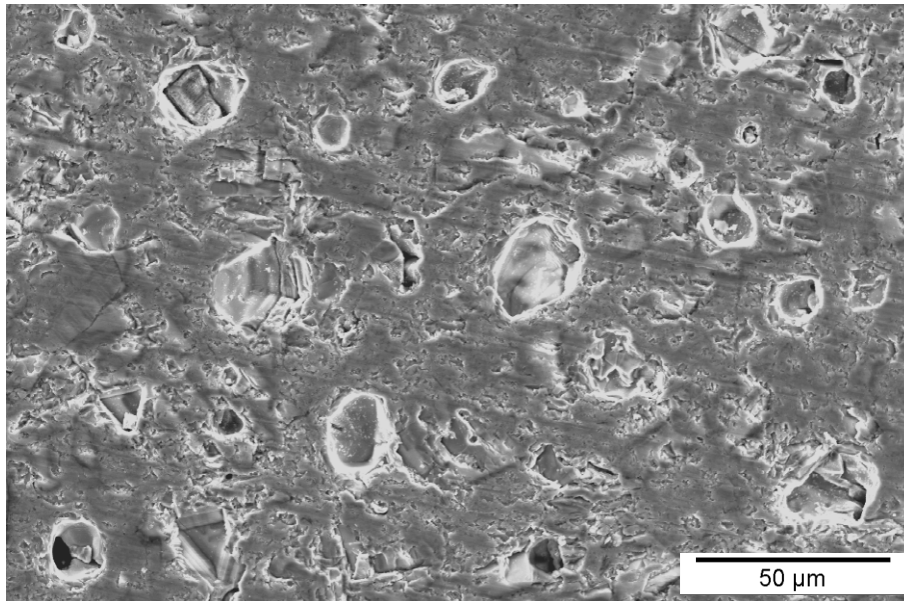
Figure 49 – SEM micrograph of sintered sample that used niobium oxide as sintering aid.

According to shrinkage versus temperature plot (Figure 50), niobium oxide promoted a slight expansion of the sample (about 1%) from 750°C up to 950°C followed by the usual shrinkage due to the sintering. Niobium oxide promotes the sintering process at lower temperature than the pure spinel. Another good point was the produced dense microstructure which is very likely for the scope of the work. Niobium oxide reduced of about 150°C the sintering temperature of the spinel, as can be seen in figure 50.
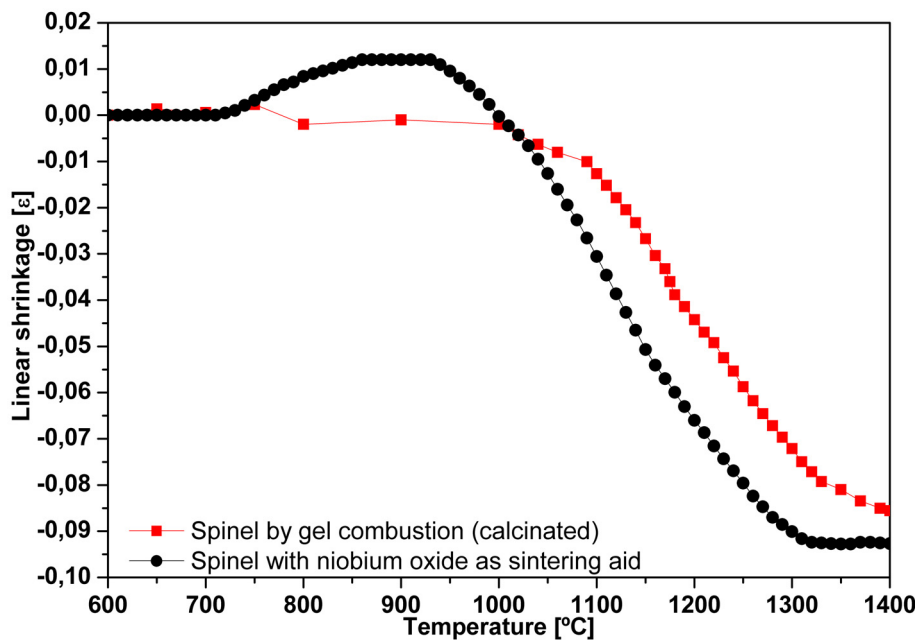
Figure 50 – Dilatrometric analysis of niobium oxide as sintering aid.

One can more clearly see that the shrinkage rate presented in figure 51 shows that the sintering process staring at around 900°C in contrast to 1050°C for pure spinel. There are also two peaks for maximum shrinking rate, one around 975°C and the second around 1150°C, which is almost the same temperature for the maximum shrinkage rate of pure spinel.
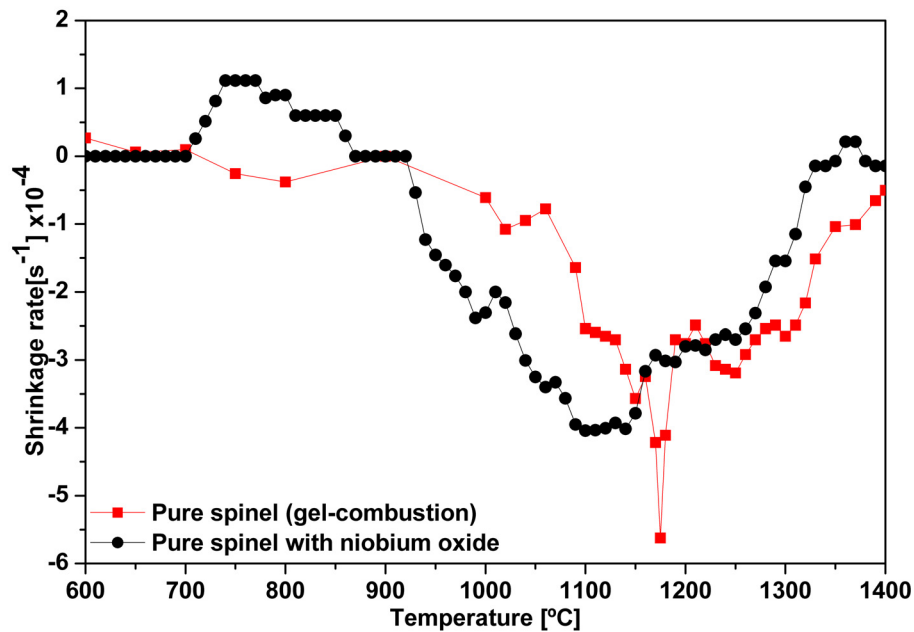
Figure 51 – Shrinkage rate of the spinel with niobium oxide.

3.3.2.4. Lithium Fluoride

Figure 52 shows dilatometric plot of pure spinel and spinel with various amount of lithium fluoride (LiF) (10, 20 and 30 wt%). The highest temperature used was chosen on the basis of previous work [49] where it was shown that temperatures above 1000°C induce damage to the stainless

steel. In addition, such temperature produces the formation of a thicker layer of chromium oxide.
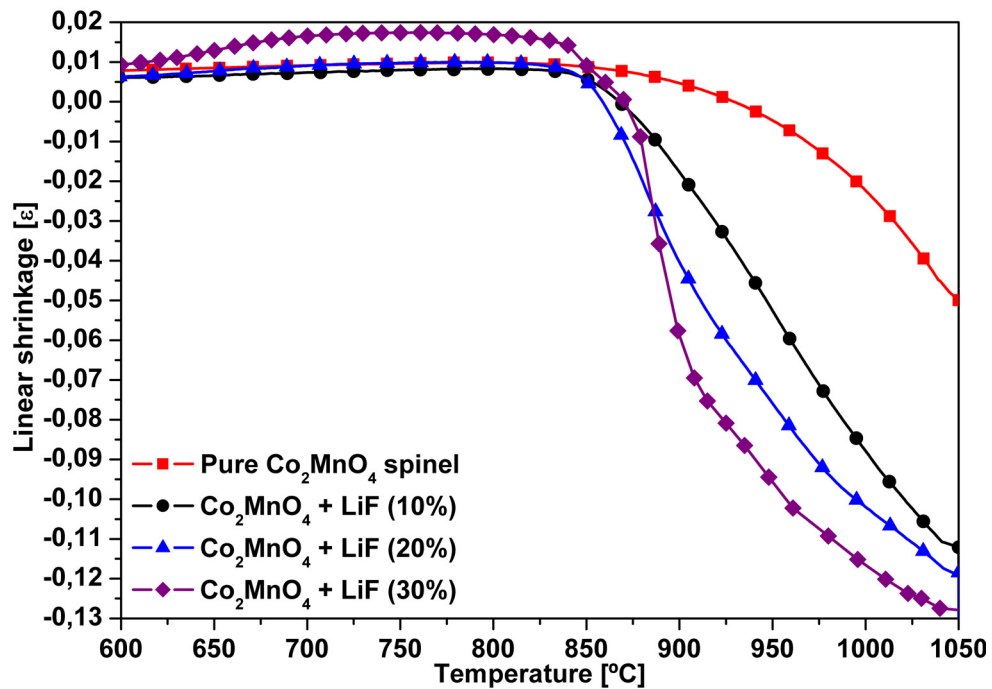
Figure 52 – Dilatometric analysis of spinel with lithium fluoride.

Pure Co_2MnO_4 starts to shrink continuously from approximately 1050°C (Figure 52) with a slow rate, though (Figure 53). With small addition of lithium fluoride the shrinkage increases and starts at much lower temperature (845°C), which is the melting point of lithium fluoride (Figure 53).
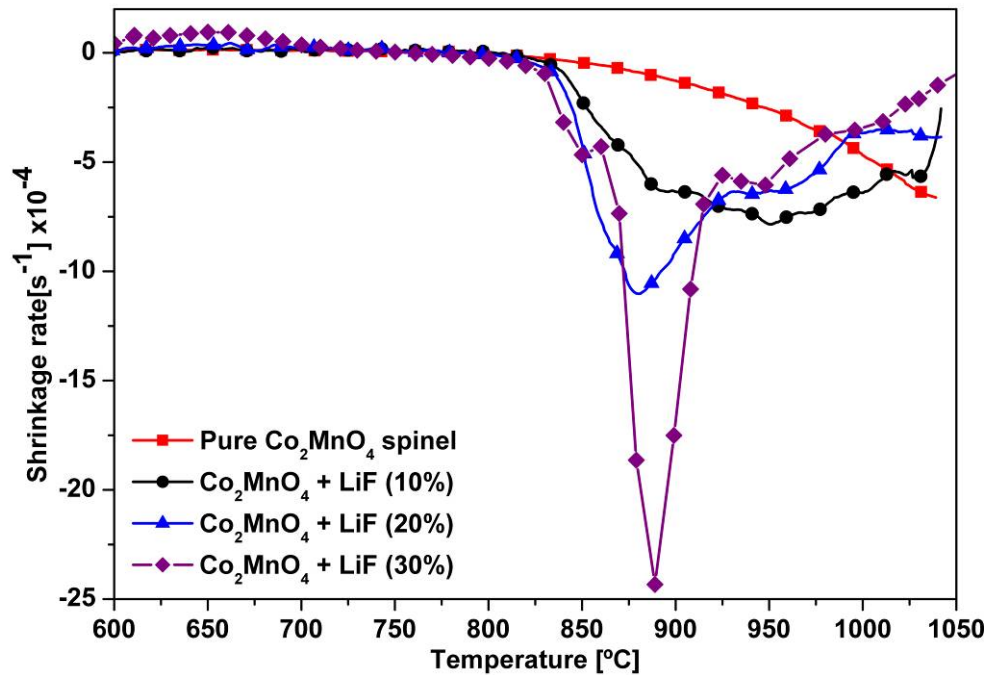
Figure 53 – Shrinkage rate of spinel with lithium fluoride.

The very fast shrinkage of spinel with 30 wt% LiF is very good for practical uses but the high amount of lithium fluoride phase worsens the desired properties of the spinel material. The final properties are worsened because lithium fluoride is known as very insulating material; therefore, in the case of conductive coating, it may be used at low concentration. High concentration of lithium fluoride might form insulating phases and reduce the overall electronic conductivity of the final set-up.

111
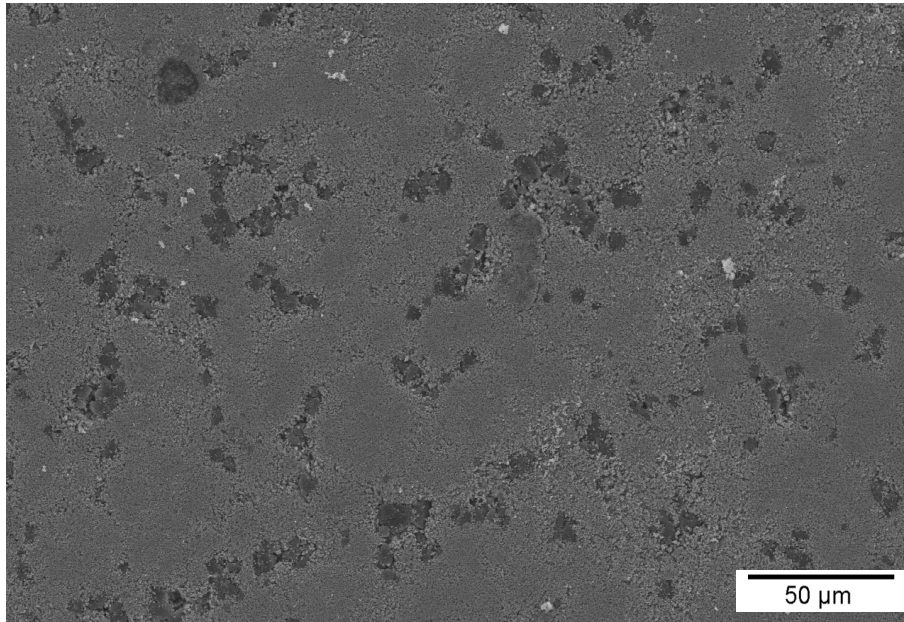
Figure 54 – SEM micrograph of green sample with 20-wt% of LiF as sintering aid.

The microstructure of green materials are shown in figure 54. It is possible to observe the well-dispersed particles of lithium fluoride (dark phase) in the matrix of spinel (brighter phase) for all concentrations of lithium fluoride in respect to spinel.

Figure 55 shows the fracture surface of spinel sintered with lithium fluoride. It is possible to observe some residual porosity. However, the pores are small and apparently that they are not interconnected.
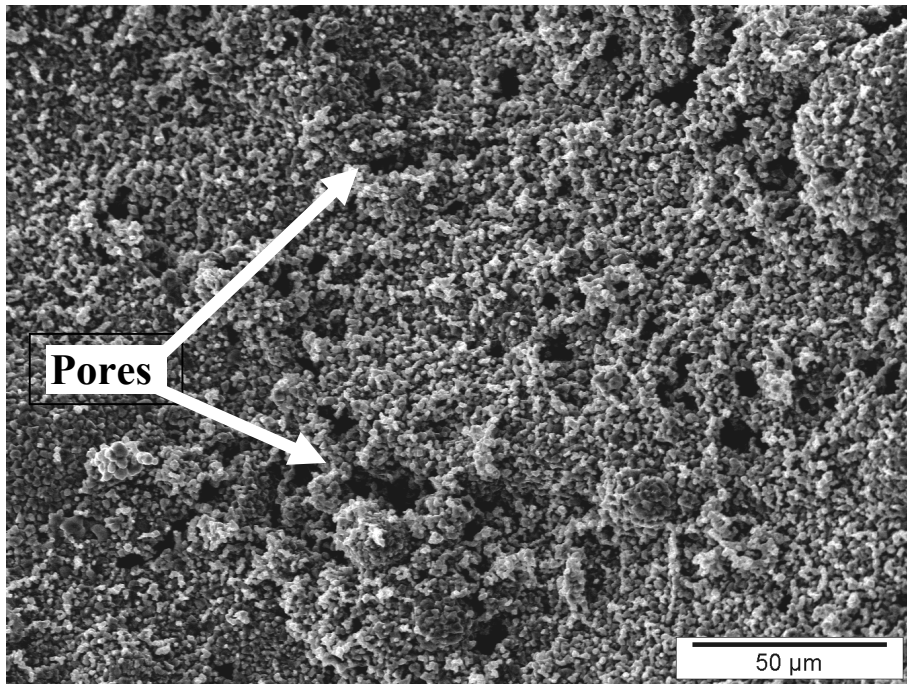
Figure 55 – SEM micrograph of sintered sample with 20-wt% of LiF as sintering aid

3.3.3. Summary

Among all the tested sintering aids, the one with best sintering performance (temperature related) was lithium fluoride because it promotes the onset for the sintering at the lowest temperature; however, lithium fluoride is the most insulating material making it not well suitable to be used in materials which will need to conduct electricity.

Niobium oxide showed the best performance regarding the density. Its sintering temperature was somewhat lower than the pure spinel but the reduction was not so evident (from 1200°C for pure spinel to 1050°C for spinel with niobium oxide). On the other hand, the density of the obtained microstructure was the highest and closest microstructure among the sintering aid.

Iron copper oxide spinel produced a very dense phase with a huge coalescence of pores. Thus, the produced microstructure presented very big pores, which make this sintering aid undesirable for barrier uses even if sintering temperature was sensibly low.

Although the faster sintering process promoted by antimony doped tin oxide as sintering aid for cobalt manganese oxide, this materials produced a highly porous microstructure. The produced microstructure could be well used as filter since the produced pores have well uniform sizes and are homogeneous dispersed.

3.4. Sintering under DC electric field

Ceramic interconnectors can be also based on perovskite structures of $LaCrO_3$ and they are most commonly used in SOFC applications though they suffer from various drawbacks [43],[44]. To avoid these drawbacks, the use metal interconnect is more promising but they must be protected from oxidizing and reducing environments. Thus, Co_2MnO_4 spinel is used as ceramic coating. A novel method to sinter Co_2MnO_4 was developed and is presented in this work.

3.4.1. Materials and Methods

Powder of Co2MnO4 spinel (particle size ~10 μm, with a specific surface area of 3,3 m^2g^{-1}) was used to carry out the experiment on DC electric field sintering. A solution of binder (B-1000, Duramax, Dow Chemical, USA) in water was produced in order to obtain 3 wt% of binder in respect to the powder. Powder was added to the solution of binder to obtain a suspension where, for a better homogeneity, excess of water was used. The suspension was mixed by mechanical stirring and let to dry in air at 85°C for 24 h. The obtained material was an agglomerate of powder and binder, which was ground in a mortar. The ground powder was pressed in a stainless steel die

into dog-bone shaped specimens. The specimens had utile dimensions according to shown in figure 56. The active section was 21 mm long with a rectangular cross-section 3,27 ± 0,02mm wide and 1 ± 0,08mm thick, the last measure depending on the amount of powder used during pressing.
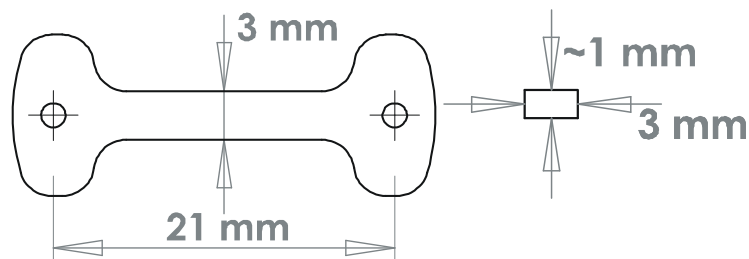
Figure 56 – Frontal draw of dog-bone sample and cross-section of gauge section.

The pressure of compaction was ~280 MPa. These specimens had a relative green density of 55,6% ± 1,2%.

Sintering was performed in a vertical tubular furnace as described in previous works [54],[63],[67] and shown in figure 57.

The sample was suspended with two (thick) platinum wires (0,25 mm diameter) that were used to carry the current from outside the furnace to the sample inside it. The connection from the power supply to the platinum wires was done with compatible high gauge insulated copper cables. A second pair of thin wires (0,127 mm diameter) was used to measure the

voltage applied to the sample. As in the 4 points method, this second pair of wires did not draw any current.
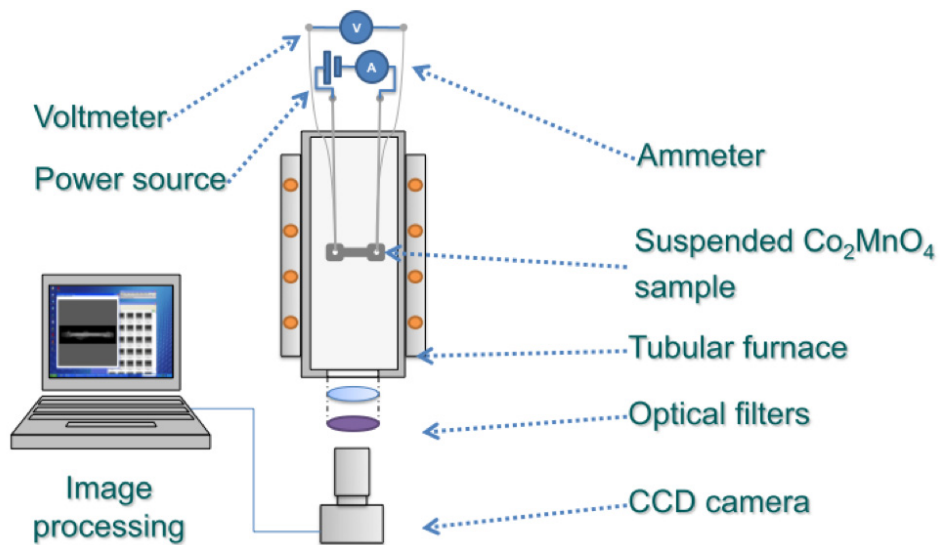
Figure 57 – Set-Up used on the flash-sintering experiment.

A constant voltage was applied to the specimen during a sintering experiment while the furnace temperature was increased at $10°C·min^{-1}$, up to $1200°C$.

The shrinkage was calculated by measuring, with a CCD camera placed underneath the furnace, the distance between the electrodes that hold the sample, as in [54],[63],[67]. Optical filters were used to protect the camera

and to avoid distortions in the images due to the thermal radiation. Figure 58 shows the equivalent circuit used in the experiment.

P – Sorensen DLM 80-13
A – Keithley 2000
V – Keithley 6517B

"A" and "V" are
connected to a computer
for data storage.
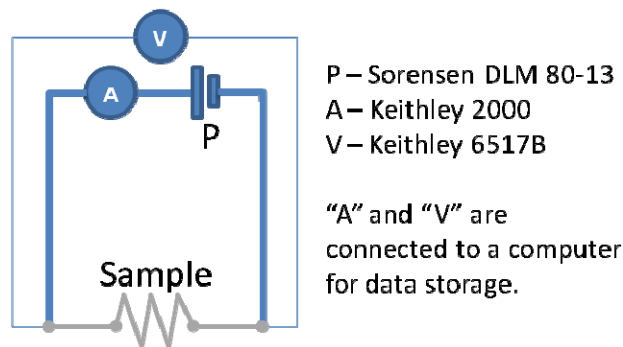
Figure 58 – Electrical diagram of the circuit used in the experiment.

Sorensen DLM 80-13 supplied the power to the applied field by applying a constant voltage to the sample. The current was measured with a Keithley 2000 digital multimeter and the voltage with a Keithley 6517B digital electrometer. The acquisition system (multimeter and electrometer) was connected to a computer for sampling and storing the data at a sampling rate of 10 Hz.

Pictures of the sample where taken during the experiment and its length were measured to evaluate the shrinkage occurred. Figure 59 shows an example of a pictures sequence.
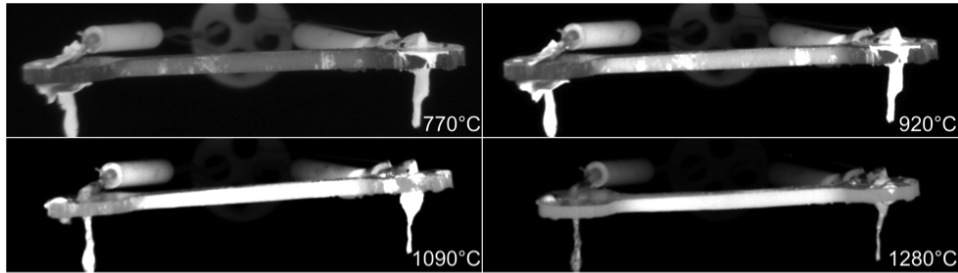
Figure 59 – Example of images taken during the experiment.

3.4.2. Discussion

Once pictures were taken every second, the measure of the sample gauge at each temperature interval was recorded and a plot of the true strain (shrinkage) versus temperature was produced. Each experiment was conducted at fixed applied voltage. The voltage was applied from the moment the furnace heating cycle starts. The true strain was calculated according to $\varepsilon = ln\left(l/l_0\right)$, where l is the time dependent length of the gauge section and l_0 is the initial gauge length. Figure 60 shows a dilatometric plot under various electric fields.

119
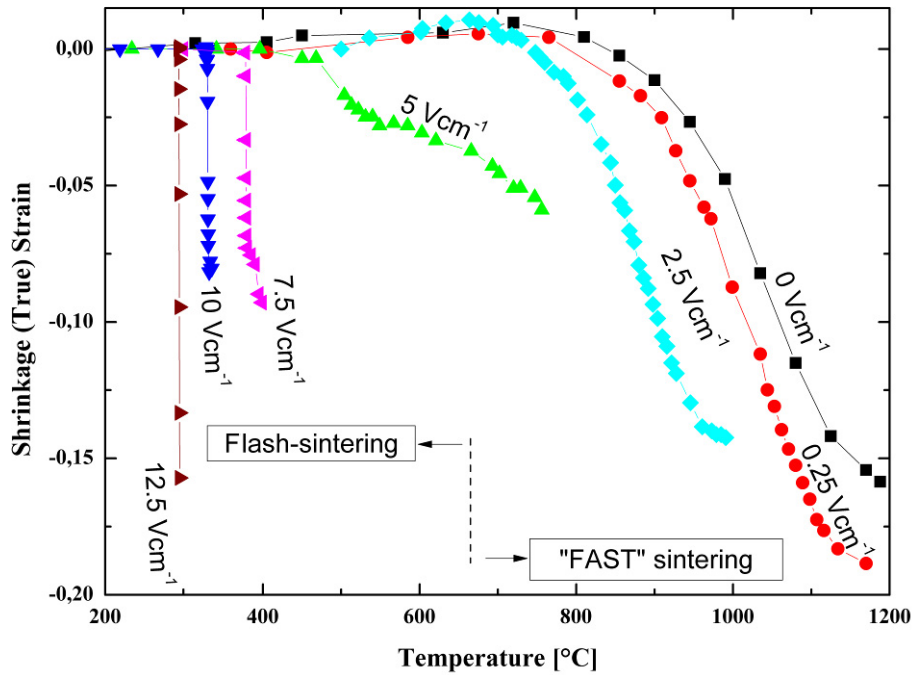
Figure 60 – Linear shrinkage with different fields as a function of furnace temperature. Heating rate is 10°C/min.

The 0 Vcm^{-1} specimen was consider as the control for the experiment since it shows the behaviour currently seen in conventional sintering. The sample sinters up to 1200°C and its microstructure contains open porosity as shown in figure 63.

The results in figure 60 show two distinct regions. When the applied electric field is below 2,5 Vcm^{-1}, the sintering rate increases gradually with applied

field; this behaviour is known as FAST (field assisted sintering). However, above 7,5 Vcm^{-1} sintering occurs in a few seconds which is a characteristic of flash sintering [54],[63],[67]. The temperature for the onset of sintering decreases when the field is increased. In the middle region, between 2,5 Vcm^{-1} and 7,5 Vcm^{-1}, the behaviour is unstable: several experiments were conducted at 5,0 Vcm^{-1} and in each case the sample broke in a similar fashion near the connection to the platinum electrode. We are unable to explain such unusual behaviour in the transition from FAST to flash sintering, which is peculiar for Co_2MnO_4 spinel, although something related to the contact resistance is thought to be the reason for the observed event.

Figure 61 shows a graph of maximal temperature reached during sintering with and without electric field. The data bring the temperature of the furnace in which the sample was sintered and it was measured using thermocouple. The maximum temperature refers to the temperature which the sample finish the sintering process, in other words, it is the temperature where the sample stops to shrink with and without electric field. Observing this graph it is easier to understand the role of the electric field in the decreasing of sintering temperature of cobalt manganese spinel.
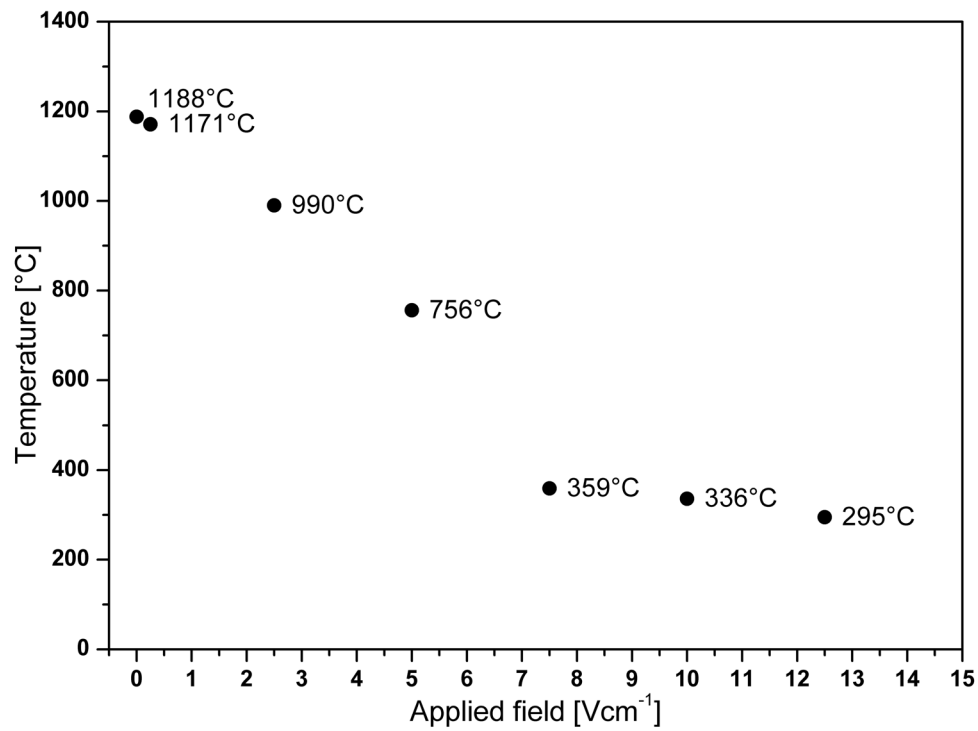
Figure 61 – Maximal temperature reached during sintering.

In the case of flash-sintering, consolidation occurs almost instantly (≥7,5 Vcm⁻¹, figure 60) as seen by the nearly vertical drop in the slope of the shrinkage curves. The temperature to reach maximum density drops from ~1200°C to ~ 400°C with a field of 7,5 Vcm⁻¹, and then to ~300°C with a field of 12,5 Vcm⁻¹.

The sintering rates, derived from the linear shrinkage data, are plotted in figure 62. The sintering rates for FAST sintering are shown in the inset since they are nearly two orders of magnitude slower than for flash-sintering: ~ 139 s versus ~ 0,66 s.
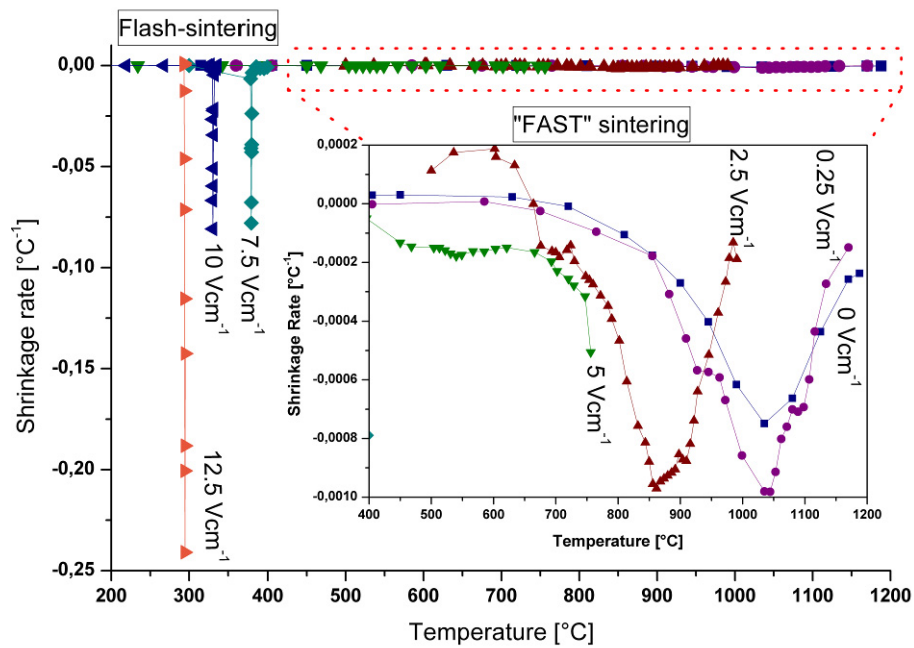
Figure 62 – Shrinking rate for each applied electric field.

Sample for SEM micrographs were prepared in two ways. The sample sintered without an electric field (the 0 Vcm^{-1}), which contained significant

porosity was fractured and the fracture surface examined in the SEM, figure 63. In the other method the samples were cross-sectioned and polished; the surfaces were thermally etched by annealing at 1150°C for 1h to delineate the grain boundaries (Figure 63). The grain boundaries in these micrographs are revealed by differences in the topography of the crystallites that are contained by them. The surfaces of the crystallites vary in their shape and depth because their etching rates vary with orientation. Micrographs for specimens sintered at 0 Vcm^{-1}, 0,25 Vcm^{-1} and 10 Vcm^{-1} are shown. In the same picture is also possible to see that the grain shapes are isotropic, that is, the unidirectional nature of the applied field does not produce a directional texture to the grain size. Grain sizes were measured by linear intercept method and obtained values were 17,9±0,2 μm, 18,3±0,1 μm and 18,7±0,2 μm, respectively to 0 Vcm^{-1}, 0,25 Vcm^{-1} and 10 Vcm^{-1}. By increasing the electric field it is noted that the porosity decreases. The specimens sintered under electrical field contained closed porosity, a characteristic that is important for SOFC interconnect applications. Whereas the specimens sintered with no electric field show open pores.
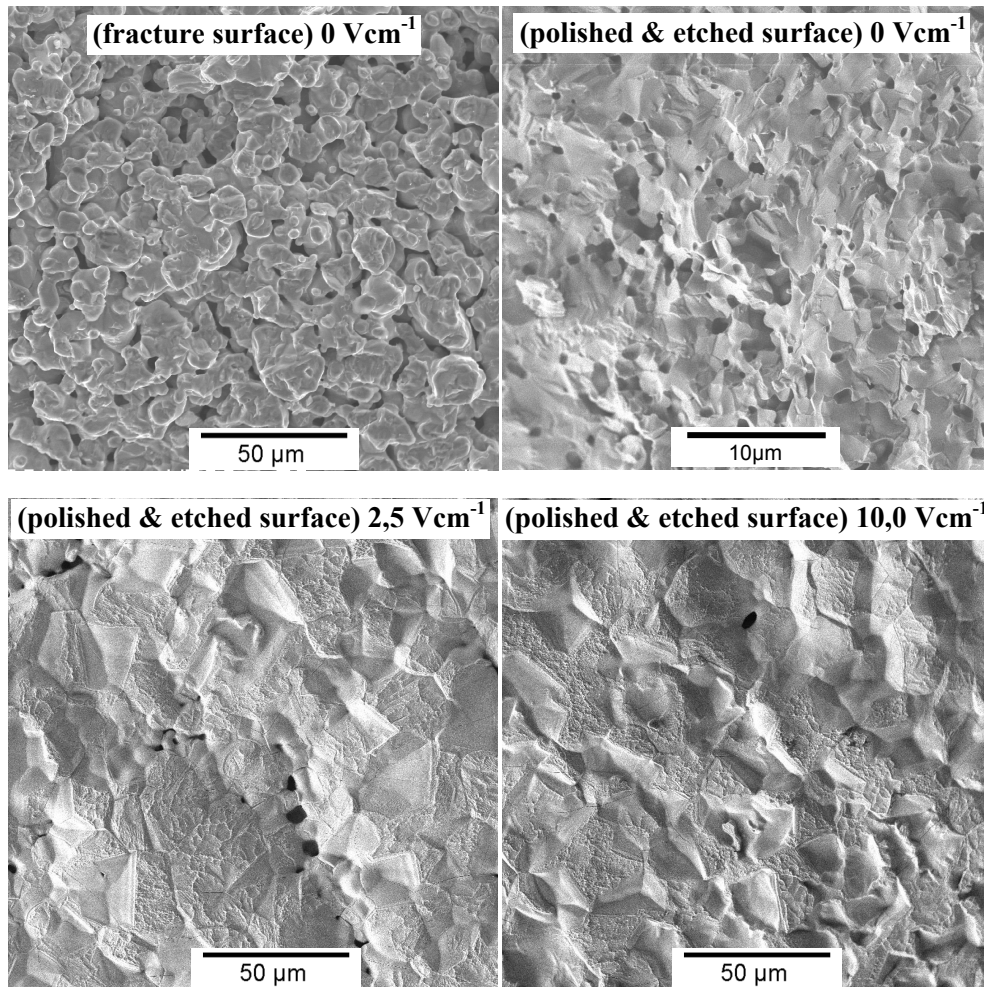
Figure 63 – Scanning electron micrographs (in secondary electron scattering mode) of samples sintered with 0 Vcm[-1], 2,5 Vcm[-1] and 10 Vcm[-1].

The power dissipation as a function of temperature from the sintering experiments is shown in form of Arrhenius plot in figure 64. The power was calculated from the product of the DC current passing through the sample and the voltage as measured by the thin wires, in the 4-point's method, as described earlier.
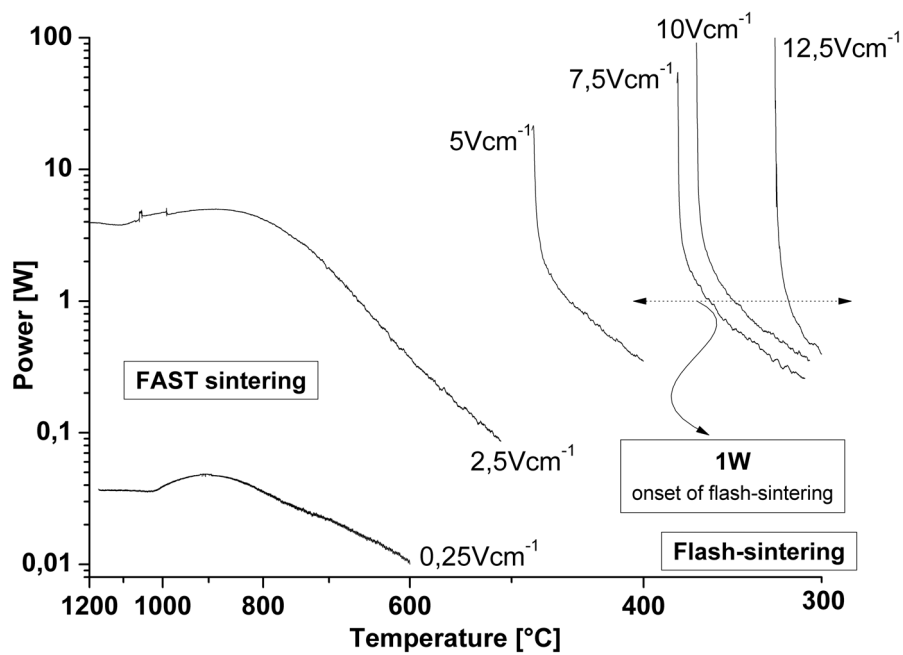
Figure 64 – Power dissipation as a function of temperature.

Careful examination of figure 64 shows that flash sintering occurs in the range of 0,5 – 4 W, with a threshold in the 1–2 W range.

It is possible to observe three different regions, FAST sintering $\leq 2,5$ Vcm^{-1}, transition region between 2,5 Vcm^{-1} and 7,5 Vcm^{-1} and flash-sintering $\geq 7,5$ Vcm^{-1}. The phenomenon of flash–sintering manifests itself as an instability in the power dissipation in the sample (by remembering that the experiments are carried out at a constant applied voltage). A similar behaviour was observed in the experiments with 3YSZ [67]. A possible explanation for this behaviour is that grain boundaries, formed by contact between particle-particle, suffer local Joule heating, thereby raising the rate of diffusional transport, as explained by [67],[108]. The argument is that power dissipation is localized at particle-particle junctions and grain boundaries because their electrical resistance is far greater than that of the grain matrix. This effect is especially pronounced in the early stages of sintering where the small contact area at particle–particle interfaces raises the local resistance and hence the temperature, thereby precipitating flash–sintering effect.

In the flash-sintering regime, the power dissipation increases abruptly, as was the case with 3YSZ and 8YSZ experiments reported earlier. It is interesting to note that the onset of flash sintering occurs at about the same power level (~1 W) as in the case of the 3YSZ and 8YSZ experiments.

When comparing yttria stabilized zirconia, which is a ionic conductor, with cobalt manganese spinel, which is a mixed ionic/electronic conductor, flash sintering occurs at lower field and temperatures, although the current is higher. The overall power dissipated at the onset of flash sintering, however, remains about the same at ~1 W (both experiments had the same specimen dimensions). While 3YSZ (ionic conductor) required a field ≥ 60 Vcm^{-1}, Co_2MnO_4 required only $\geq 7,5$ Vcm^{-1} to produce flash-sintering, a difference attributed to the different conductivity of the two materials: the current was much greater for the spinel. As a matter of fact, in 3YSZ experiments the circuit was designed to limit the current to 0,50 A but this limit was increased to 13 A for the experiments with Co_2MnO_4.

The X-ray diffraction spectra for the as received powder and the flash-sintered specimen (in this instance at a field of 12,5 Vcm^{-1}) are given in figure 65. The diffraction peaks from these two specimens are highly congruent, leading to the conclusion that the flash sintering process did not produce an intrinsic change in the structure of the spinel.
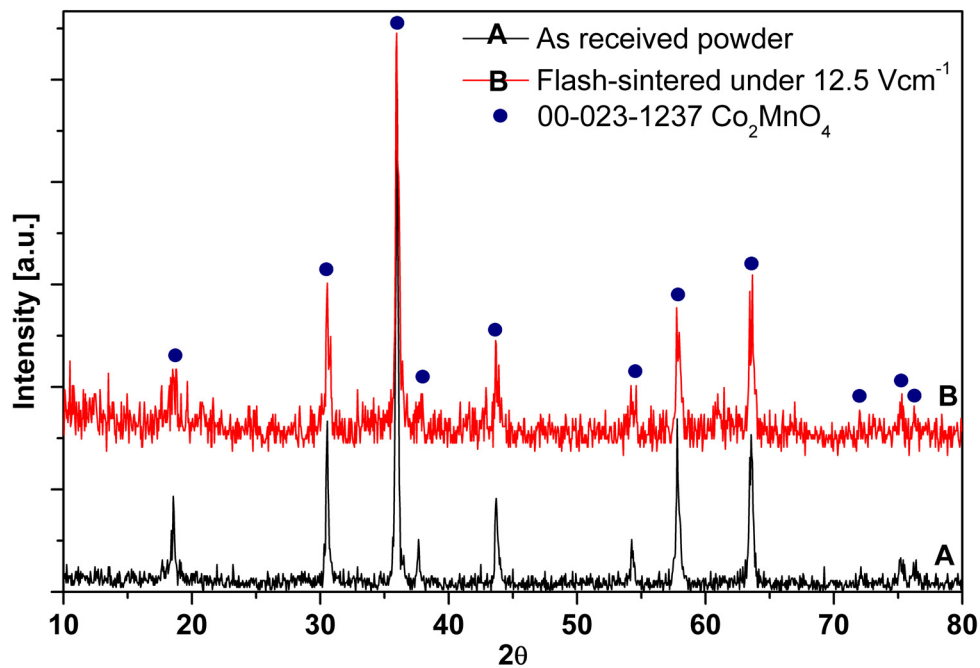
Figure 65 – X-ray diffraction pattern of cobalt manganese oxide powder and sintered under electric field.

3.4.3. Summary

In conventional sintering of Co_2MnO_4 neck growth begins at about 800°C, and full densification is achieved at temperatures near 1300°C [49]. Applying modest DC electrical fields of 12,5 Vcm^{-1} in pressure–less sintering, it was possible to achieve closed porosity at temperatures of only

300°C. The sintering process last just a few seconds that is in the mode of flash sintering. At lower fields the sintering rate was increased gradually by increasing the applied field, similar to the phenomenon known as field assisted sintering (FAST). At a certain field a transition region between flash and FAST sintering was also denoted implying that a limitation of FAST sintering would occur. The sintering rates in flash-sintering are nearly two orders of magnitude faster than in FAST, not taking into account the much lower sintering temperatures. It is postulated that higher electrical resistance of grain boundaries and particle–particle contacts concentrates the power dissipation at interfaces, therefore increasing the rate of diffusional transport in a giant manner.

Grain growth behaviour is also different between flash and FAST sintering. What is also important is that in the case of 3YSZ FAST sintering could be explained by the reduced rate of grain growth under an applied field [69]. However, the grain size is not significantly reduced, indeed in the case of Co_2MnO_4 it appears to be enhanced. The grain growth explained suggest that a new mechanism for this phenomenon should be consider since the flash sintering appears to have multiple causes.

The implementation of flash-sintering in the production of Co_2MnO_4 impermeable coatings on stainless steel for SOFC application seems to be possible. An effort toward this direction must be taken from research institutes and industries. The lower processing temperatures, and ultrafast

sintering times would prevent the formation of undesirable chromium oxide interlayers in the manufacturing process, therefore increasing coating quality and fuel cell life time.

4. CONCLUSION

Since the cobalt manganese oxide spinel is used as coating on stainless steel, the sintering temperature is very important. Temperature above 900°C provoke formation of thick chromium-rich layer, which is deleterious for long-term stability of fuel cell because high probability of chromium poising of cathode.

Cobalt manganese oxide spinel was successfully produced by all methods proposed (solid-state reaction, gel-combustion, co-precipitation and reverse micelle). Reverse micelle produced finest particles, with highest specific surface area and very reactive, although the production in large scale by this method is cost-prohibitive.

Gel combustion was the most reliable method. Due to the simplicity of the method and ordinary reagents it can be easily scalable industrially. In addition, the productivity of this method was one of the highest obtaining, at the same time small particles, in large amount.

Lithium fluoride as sintering aid promoted the highest decrease in the onset of Co_2MnO_4 sintering. The drawback in the use of lithium fluoride is that this material is highly insulating.

Niobium oxide showed the best performance regarding the density of obtained microstructure. Moreover, the used of niobium oxide reduce in ~200°C the sintering temperature of Co_2MnO_4.

Applying DC electrical fields of 12 V cm^{-1} in pressure-less sintering, it was possible to achieve closed porosity at temperatures of only 300°C. the sintering process last just a few seconds, phenomenon known as "flash-sintering".

The lower processing temperatures, and the fast sintering time would prevent the formation of undesirable chromium oxide interlayer in the manufacturing process of Co_2MnO_4 coating. The feasibility of a straightforward sintering process of cobalt manganese oxide spinel by means of applied DC electrical field was therefore demonstrated and is encouraging further research.

The implementation of flash-sintering in the production of Co_2MnO_4 dense coatings on stainless steel for SOFC application seems to be possible, and more effort toward this direction in encouraged.

5. REFERENCES

[1]   C.F. Schönbein, "Beobachtungen über das elektromotorische Verhalten einiger Metallhyperoxyde, des Platins und des passiven Eisens," *Annalen der Physik und Chemie*, vol. 119, 1838, pp. 89-103.

[2]   W.R. Grove, "On voltaic series and the combination of gases by platinum," *Philosophical Magazine Series 3*, vol. 14, 1839, p. 127.

[3]   W.R. Grove, "On a gaseous voltaic battery," *Philosophical Magazine Series 3*, vol. 21, 1842, p. 417.

[4]   T. Bacon, "Alkaline primary cells," U.S. Patent 2716670, August 30, 1955.

[5]   T. Bacon, "Porous nickel electrode," U.S. Patent 2928783, March 15, 1960.

[6]   M. Woods and M. Bernstein, "200-fold boost in fuel cell efficiency advances "personalized energy systems"," Aug. 2010.

[7]   R.A. Roberts and J. Brouwer, "Dynamic Simulation of a Pressurized 220 kW Solid Oxide Fuel-Cell–Gas-Turbine Hybrid System: Modeled Performance Compared to Measured Results," *Journal of Fuel Cell Science and Technology*, vol. 3, 2006, p. 18.

[8]   T. Baumeister, *Marks' standard handbook for mechanical engineers*, New York ;;London: McGraw-Hill, 1995.

[9]   D.U. Eberle and D.R. von Helmolt, "Sustainable transportation based on electric vehicle concepts: a brief overview," *Energy & Environmental Science*, vol. 3, 2010, p. 689.

[10]   C.P. Garcia, B. Chang, D.W. Johnson, D.J. Bents, V.J. Scullin, and I.J. Jakupca, *Round Trip Energz Efficiency of NASA Glenn Regenerative Fuel Cell Szstem*, Long Beach, California, USA: 2006.

[11]   "Ali, S. A., The Role of Fuel Cells in Generating Clean Power and Reducing Greenh."

[12]   W.G. Colella, R.J. Timme, J. Brouwer, and N.M. Sammes, "Fuel cell efficiency can exceed 50% at peak power," *Journal of Power Sources*, 2011.

[13]   J. Benziger, M. Satterfield, W. Hogarth, J. Nehlsen, and I. Kevrekidis, "The power performance curve for engineering analysis of fuel cells," *Journal of Power Sources*, 2005.

[14]   J. Kunze and U. Stimming, "Electrochemical Versus Heat-Engine Energy Technology: A Tribute to Wilhelm Ostwald's Visionary Statements," *Angewandte Chemie International Edition*, vol. 48, 2009, pp. 9230-9237.

[15]   A.D. Le and B. Zhou, "A general model of proton exchange membrane fuel cell," *Journal of Power Sources*, vol. 182, 2008, pp. 197-222.

[16]   "FCT Fuel Cells: Types of Fuel Cells," Mar. 2011.

[17] N. Syred and A. Khalatov, Eds., *Advanced Combustion and Aerothermal Technologies*, Dordrecht: Springer Netherlands, 2007.

[18] "DTI Energy Inc. -- DMFC exclusive liscensor -- Direct Methanol Fuel Cell Process," Mar. 2011.

[19] I. Sprague and P. Dutta, "Role of the diffuse layer in acidic and alkaline fuel cells," *Electrochimica Acta*, 2011.

[20] "Alkaline fuel cell - Wikipedia, the free encyclopedia."

[21] J. Milewski, J. Lewandowski, and A. Miller, "Reducing CO_2 emission from a coal fired power plant by using a molten carbonate fuel cell," *Chemical and Process Engineering*, vol. 30, 2009, pp. 341-350.

[22] J. Milewski, T. Świercz, K. Badyda, A. Miller, A. Dmowski, and P. Biczel, "The control strategy for a molten carbonate fuel cell hybrid system," *International Journal of Hydrogen Energy*, vol. 35, 2010, pp. 2997-3000.

[23] A. Dicks, "Molten carbonate fuel cells," *Current Opinion in Solid State and Materials Science*, vol. 8, 2004, pp. 379-383.

[24] S. Singhal, *High-temperature solid oxide fuel cells : fundamentals, design, and applicatons*, New York: Elsevier Advanced Technology, 2003.

[25] S. Singhal, "Ceramic Fuel Cells for Stationary and Mobile Applications," *American Ceramic Society Bulletin*, Nov. 2003, pp.

9601-9610.

[26] H. Möbius, "On the history of solid electrolyte fuel cells," *Journal of Solid State Electrochemistry*, vol. 1, 1997, pp. 2-16.

[27] E. Ivers-Tiffée, A. Weber, and D. Herbstritt, "Materials and technologies for SOFC-components," *Journal of the European Ceramic Society*, vol. 21, 2001, pp. 1805-1811.

[28] D. Montinaro, "Synthesis and Processing of Oxides Powders for Solid Oxide Fuel Cells (SOFC) Production," PhD Thesis, University of Trento, 2007.

[29] H. Yokokawa, N. Sakai, T. Horita, and K. Yamaji, "Recent Developments in Solid Oxide Fuel Cell Materials," *Fuel Cells*, vol. 1, 2001, pp. 117-131.

[30] F. Tietz, "Materials Selection for Solid Oxide Fuel Cells," *Materials Science Forum*, vol. 426-432, 2003, pp. 4465-4470.

[31] K. Wincewicz and J. Cooper, "Taxonomies of SOFC material and manufacturing alternatives," *Journal of Power Sources*, vol. 140, 2005, pp. 280-296.

[32] B.C. Steele and A. Heinzel, "Materials for fuel-cell technologies," *Nature*, vol. 414, Nov. 2001, pp. 345-352.

[33] S. Haile, "Materials for fuel cells," *Materials Today*, vol. 6, 2003, pp. 24-29.

[34] S. Singhal, "Advances in solid oxide fuel cell technology," *Solid*

State Ionics, vol. 135, 2000, pp. 305-313.

[35] W. Liu, X. Sun, E. Stephens, and M. Khaleel, "Life prediction of coated and uncoated metallic interconnect for solid oxide fuel cell applications," *Journal of Power Sources*, vol. 189, 2009, pp. 1044-1050.

[36] M. Tucker, H. Kurokawa, C. Jacobson, L. Dejonghe, and S. Visco, "A fundamental study of chromium deposition on solid oxide fuel cell cathode materials," *Journal of Power Sources*, vol. 160, 2006, pp. 130-138.

[37] X. Chen, B. Hua, J. Pu, J. Li, L. Zhang, and S.P. Jiang, "Interaction between (La, Sr)MnO$_3$ cathode and Ni–Mo–Cr metallic interconnect with suppressed chromium vaporization for solid oxide fuel cells," *International Journal of Hydrogen Energy*, vol. 34, 2009, pp. 5737-5748.

[38] A. Stambouli, "Solid oxide fuel cells (SOFCs): a review of an environmentally clean and efficient source of energy," *Renewable and Sustainable Energy Reviews*, vol. 6, 2002, pp. 433-455.

[39] M. Cologna, "Advances in the Production of Planar and Micro-Tubular Solid Oxide Fuel Cells," PhD Thesis, University of Trento, 2009.

[40] S. Fontana, R. Amendola, S. Chevalier, P. Piccardo, G. Caboche, M. Viviani, R. Molins, and M. Sennour, "Metallic interconnects for

SOFC: Characterisation of corrosion resistance and conductivity evaluation at operating temperature of differently coated alloys," *Journal of Power Sources*, vol. 171, 2007, pp. 652-662.

[41] X. Chen, P. Hou, C. Jacobson, S. Visco, and L. Dejonghe, "Protective coating on stainless steel interconnect for SOFCs: oxidation kinetics and electrical properties," *Solid State Ionics*, vol. 176, 2005, pp. 425-433.

[42] P. Piccardo, R. Amendola, S. Fontana, S. Chevalier, G. Caboches, and P. Gannon, "Interconnect materials for next-generation solid oxide fuel cells," *Journal of Applied Electrochemistry*, vol. 39, 2009, pp. 545-551.

[43] F. Tietz, "Components manufacturing for solid oxide fuel cells," *Solid State Ionics*, vol. 152-153, 2002, pp. 373-381.

[44] W. Zhu and M. Yan, "Perspectives on the metallic interconnects for solid oxide fuel cells," *Journal of Zhejiang University Science*, vol. 5, 2004, pp. 1471-1503.

[45] M. Bertoldi, T. Zandonella, D. Montinaro, A. Quaranta, and V. Sglavo, *Coatings for Ferritic Steels: How to prevent Cr-Evaporation and Maitain a Low Contact Resistance?*, 2007.

[46] S.C. Paulson and V.I. Birss, "Chromium Poisoning of LSM-YSZ SOFC Cathodes," *Journal of The Electrochemical Society*, vol. 151, 2004, p. A1961.

[47] C. Collins, J. Lucas, T. Buchanan, M. Kopczyk, A. Kayani, P. Gannon, M. Deibert, R. Smith, D. Choi, and V. Gorokhovsky, "Chromium volatility of coated and uncoated steel interconnects for SOFCs," *Surface and Coatings Technology*, vol. 201, 2006, pp. 4467-4470.

[48] S. Chandra-Ambhorn and S. Ieamsupapong, "Evaluation of Crofer 22 APU Stainless Steel used as Interconnect in Solid Oxide Fuel Cells Oxidised in Dry and Humidified Cathode Atmospheres," *AIJSTPME*, vol. 3, 2010, pp. 29-34.

[49] A.L. Prette and V. Sglavo, "Densification of $MnCo_2O_4$ protective coatings for SOFC interconnectors," Jan. 2009.

[50] ThyssenKrupp VDM, *Crofer 22 APU: Material Data Sheet*, 2008.

[51] Z. Yang, G. Xia, G. Maupin, and J. Stevenson, "Conductive protection layers on oxidation resistant alloys for SOFC interconnect applications," *Surface and Coatings Technology*, vol. 201, 2006, pp. 4476-4483.

[52] J.Y. Kim, N.L. Canfield, L.A. Chick, K.D. Meinhardt, and V.L. Sprenkle, "Chromium Poisoning Effects on Various Cathodes," *Ceramic Engineering and Science Proceedings*, Hoboken, NJ, USA: John Wiley & Sons, Inc., 2008, pp. 129-138.

[53] M. Bateni, P. Wei, X. Deng, and A. Petric, "Spinel coatings for UNS 430 stainless steel interconnects," *Surface and Coatings Technology*,

vol. 201, 2007, pp. 4677-4684.

[54] A.L. Prette, M. Cologna, V. Sglavo, and R. Raj, "Flash-sintering of Co2MnO4 spinel for solid oxide fuel cell applications," *Journal of Power Sources*, vol. 196, 2011, pp. 2061-2065.

[55] A. Petric and H. Ling, "Electrical Conductivity and Thermal Expansion of Spinels at Elevated Temperatures," *Journal of the American Ceramic Society*, vol. 90, 2007, pp. 1515-1520.

[56] T. Uehara, N. Yasuda, M. Okamoto, and Y. Baba, "Effect of Mn–Co spinel coating for Fe–Cr ferritic alloys ZMG232L and 232J3 for solid oxide fuel cell interconnects on oxidation behavior and Cr-evaporation," *Journal of Power Sources*, 2010.

[57] J. Mizusaki and Electrochemical Society.;Electrochemical Society.;Electrochemical Society., *Solid oxide fuel cells IX : (SOFC-IX) : proceedings of the International Symposium*, Pennington N.J.: Electrochemical Society, 2005.

[58] A. Balland, P. Gannon, M. Deibert, S. Chevalier, G. Caboche, and S. Fontana, "Investigation of La_2O_3 and/or $(Co,Mn)_3O_4$ deposits on Crofer22APU for the SOFC interconnect application," *Surface and Coatings Technology*, vol. 203, 2009, pp. 3291-3296.

[59] R. Orrù, R. Licheri, A.M. Locci, A. Cincotti, and G. Cao, "Consolidation/synthesis of materials by electric current activated/assisted sintering," *Materials Science and Engineering: R:*

Reports, vol. 63, 2009, pp. 127-287.

[60] S. Grasso, Y. Sakka, and G. Maizza, "Electric current activated/assisted sintering (ECAS): a review of patents 1906–2008," *Science and Technology of Advanced Materials*, vol. 10, 2009, p. 053001.

[61] Joule, J. P., "On the Production of Heat by Voltaic Electricity," *Philosophical Transactions of the Royal Society of London*, vol. 4, 1837, pp. 280-282.

[62] A.G.[.+.(.G.B. Bloxam, "Improved Manufacture Of Electric Incandescence Lamp Filaments From Tungsten Or Molybdenum Or An Alloy Thereof.," U.S. Patent GB190527002 (A), December 13, 1906.

[63] M. Cologna, A.L.G. Prette, and R. Raj, "Flash-Sintering of Cubic Yttria-Stabilized Zirconia at 750°C for Possible Use in SOFC Manufacturing," *Journal of the American Ceramic Society*, vol. 94, 2011, pp. 316-319.

[64] U. Anselmitamburini, J. Garay, and Z. Munir, "Fast low-temperature consolidation of bulk nanometric ceramic materials," *Scripta Materialia*, vol. 54, 2006, pp. 823-828.

[65] M.L. Allen, M. Aronniemi, T. Mattila, A. Alastalo, K. Ojanperä, M. Suhonen, and H. Seppä, "Electrical sintering of nanoparticle structures," *Nanotechnology*, vol. 19, 2008, p. 175201.

[66] D. Yang, R. Raj, and H. Conrad, "Enhanced Sintering Rate of Zirconia (3Y-TZP) Through the Effect of a Weak dc Electric Field on Grain Growth," *Journal of the American Ceramic Society*, vol. 93, 2010, pp. 2935-2937.

[67] M. Cologna and R. Raj, "Surface Diffusion-Controlled Neck Growth Kinetics in Early Stage Sintering of Zirconia, with and without Applied DC Electrical Field," *Journal of the American Ceramic Society*, 2010, pp. no-no.

[68] Z. Yang, "Recent advances in metallic interconnects for solid oxide fuel cells," *International Materials Reviews*, vol. 53, 2008, pp. 39-54.

[69] S. Ghosh, A.H. Chokshi, P. Lee, and R. Raj, "A Huge Effect of Weak dc Electrical Fields on Grain Growth in Zirconia," *Journal of the American Ceramic Society*, vol. 92, 2009, pp. 1856-1859.

[70] R.M. Young and R. McPherson, "Temperature-Gradient-Driven Diffusion in Rapid-Rate Sintering," *Journal of the American Ceramic Society*, vol. 72, 1989, pp. 1080-1081.

[71] M. Bertoldi, T. Zandonella, D. Montinaro, V.M. Sglavo, A. Fossati, A. Lavacchi, C. Giolli, and U. Bardi, "Protective Coatings of Metallic Interconnects for IT-SOFC Application," *Journal of Fuel Cell Science and Technology*, vol. 5, 2008, p. 011001.

[72] N. Rajeevan, R. Kumar, D. Shukla, P. Pradyumnan, S. Arora, and I.

Shvets, "Structural, electrical and magnetic properties of Bi-substituted Co_2MnO_4," *Materials Science and Engineering: B*, vol. 163, 2009, pp. 48-56.

[73] A. West, *Solid state chemistry and its applications*, Chichester [West Sussex] ;;New York: Wiley, 1984.

[74] X. Guo, B. Ravi, P. Devi, J. Hanson, J. Margolies, R. Gambino, J. Parise, and S. Sampath, "Synthesis of yttrium iron garnet (YIG) by citrate–nitrate gel combustion and precursor plasma spray processes," *Journal of Magnetism and Magnetic Materials*, vol. 295, 2005, pp. 145-154.

[75] T. Takeda, K. Kato, and S. Kikkawa, "Gel Combustion Synthesis of Rare Earth Aluminate Using Glycine or Urea," *Journal of the Ceramic Society of Japan*, vol. 115, 2007, pp. 588-591.

[76] M.T. Colomer, D.A. Fumo, J.R. Jurado, and A.M. Segadaẽs, "Non-stoichiometric $La(1 − x)NiO(3 − \delta)$ perovskites produced by combustion synthesis," *Journal of Materials Chemistry*, vol. 9, 1999, pp. 2505-2510.

[77] S. Gallini, J.R. Jurado, and M.T. Colomer, "Combustion Synthesis of Nanometric Powders of $LaPO_4$ and Sr-Substituted $LaPO_4$," *Chemistry of Materials*, vol. 17, 2005, pp. 4154-4161.

[78] T. Mimani, "Instant synthesis of nanoscale spinel aluminates," *Journal of Alloys and Compounds*, vol. 315, 2001, pp. 123-128.

[79] S.S. Manoharan and K.C. Patil, "Combustion Synthesis of Metal Chromite Powders," *Journal of the American Ceramic Society*, vol. 75, 1992, pp. 1012-1015.

[80] M. Kakade, "Yttrium aluminum garnet powders by nitrate decomposition and nitrate–urea solution combustion reactions—a comparative study," *Journal of Alloys and Compounds*, vol. 350, 2003, pp. 123-129.

[81] L.E. Shea, J. Mckittrick, and O.A. Lopez, "Synthesis of Red-Emitting, Small Particle Size Luminescent Oxides Using an Optimized Combustion Process.," *ChemInform*, vol. 28, 2010, pp. no-no.

[82] K. Ito, K. Hayashi, and T. Yamada, "Cobalt Oxyhydroxide, Method for Producing the Same and Alkaline Storage Battery Using the Same," U.S. Patent 20090233173, September 17, 2009.

[83] E.A. Vasilyeva, L. Morozova, A. Lapshin, and V. Konakov, "Ceramic Materials with Controlled Porosity," *Materials Physics and Mechanics*, vol. 5, 2002, pp. 43-48.

[84] S. Tamura, K. Takeuchi, G. Mao, R. Csencsits, L. Fan, T. Otomo, and M. Saboungi, "Colloidal silver iodide: synthesis by a reverse micelle method and investigation by a small-angle neutron scattering study," *Journal of Electroanalytical Chemistry*, vol. 559, 2003, pp. 103-109.

[85] M. Pileni, *Structure and reactivity in reverse micelles*, Amsterdam

;;New York: Elsevier, 1989.

[86] R. Misra, S. Gubbala, A. Kale, and W. Egelhoff, "A comparison of the magnetic characteristics of nanocrystalline nickel, zinc, and manganese ferrites synthesized by reverse micelle technique," *Materials Science and Engineering B*, vol. 111, 2004, pp. 164-174.

[87] L.E. James, L. Crescentini, and W.B. Fisher, "Process for making a cobalt oxide catalyst," U.S. Patent 4389339, June 21, 1983.

[88] R. German, *Sintering theory and practice*, New York: Wiley, 1996.

[89] A.L. Prette, "Development of Ceramic Glazes: Application in electrical Insulators of high-performance," Master Thesis, Federal University of Santa Catarina, 2007.

[90] E. Elangovan and K. Ramamurthi, "A study on low cost-high conducting fluorine and antimony-doped tin oxide thin films," *Applied Surface Science*, vol. 249, 2005, pp. 183-196.

[91] K. Sivaraman, S. Qin, and M. Gao, "Translucent polycrystalline alumina ceramic," U.S. Patent 7678725, March 16, 2010.

[92] G. Bernardgranger and C. Guizard, "Influence of MgO or TiO2 doping on the sintering path and on the optical properties of a submicronic alumina material," *Scripta Materialia*, vol. 56, 2007, pp. 983-986.

[93] P. Hing, "Fabrication of translucent magnesium aluminate spinel and its compatibility in sodium vapour," *Journal of Materials Science*,

vol. 11, 1976, pp. 1919-1926.

[94] M.R. Sahar and M. Hasbullah, "Properties of SnO_2-based ceramics," *Journal of Materials Science*, vol. 30, 1995, pp. 5304-5306.

[95] R. Selvan, "Combustion synthesis of $CuFe_2O_4$," *Materials Research Bulletin*, vol. 38, 2003, pp. 41-54.

[96] R.K. Selvan, C. Augustin, V. Šepelák, L.J. Berchmans, C. Sanjeeviraja, and A. Gedanken, "Synthesis and characterization of $CuFe_2O_4$/CeO_2 nanocomposites," *Materials Chemistry and Physics*, vol. 112, 2008, pp. 373-380.

[97] R. Kalaiselvan, N. Kalaiselvi, C. Augustin, C. Doh, and C. Sanjeeviraja, "$CuFe_2O_4$/SnO_2 nanocomposites as anodes for Li-ion batteries," *Journal of Power Sources*, vol. 157, 2006, pp. 522-527.

[98] R. Roth and National Bureau of Standards.;American Ceramic Society., *Phase diagrams for ceramists IV*, Westerville: American Ceramic Society, 1981.

[99] L. Chen, S. Wu, G. Wang, and S. Wang, "Structure and dielectric properties of ZnO and Nb_2O_5 doped BaO-TiO_2 system microwave ceramics," *Journal of Wuhan University of Technology-Mater. Sci. Ed.*, vol. 23, 2008, pp. 647-651.

[100] T. Kutty, K. Khan, A. Kumar, and H. Kamath, "Densification strain rate in sintering of ThO_2 and ThO_2-0.25% Nb_2O_5 pellets," *Science of Sintering*, vol. 41, 2009, pp. 103-115.

[101] A. Yaylı, S. Kırtay, E. Oktay, A. Van, M. Aybers, and L. Çolak, "Sintering Properties of V_2O_5, Ta_2O_5 and Nb_2O_5 Doped ThO_2 Powder Under Ar-10% H_2 Atmosphere," *Key Engineering Materials*, vol. 264-268, 2004, pp. 305-308.

[102] C. Li, J. Wang, X. Wang, W. Su, H. Chen, and D. Zhuang, "Nonlinear electrical properties of TiO_2–Y_2O_3–Nb_2O_5 capacitor-varistor ceramics," *Materials Science and Engineering B*, vol. 85, 2001, pp. 6-10.

[103] C. Cheng, J. Lin, and H. Lin, "Addition of Nb_2O_5 on the electrical properties of buried resistors in low-temperature cofired ceramics," *Journal of Materials Research*, vol. 18, 2003, pp. 1211-1218.

[104] G.R. Villalobos, J.S. Sanghera, S.S. Bayya, and I.D. Aggarwal, "Spinel and process for making same," U.S. Patent 7611661, November 3, 2009.

[105] I.E. Reimanis and H. Kleebe, "Reactions in the sintering of $MgAl_2O_4$ spinel doped with LiF," *International Journal of Materials Research (formerly Zeitschrift fuer Metallkunde)*, vol. 98, 2007, pp. 1273-1278.

[106] I. Reimanis and H. Kleebe, "A Review on the Sintering and Microstructure Development of Transparent Spinel ($MgAl_2O_4$)," *Journal of the American Ceramic Society*, vol. 92, 2009, pp. 1472-1480.

[107] G.R. Villalobos, J.S. Sanghera, and I.D. Aggarwal, "Degradation of Magnesium Aluminum Spinel by Lithium Fluoride Sintering Aid," *Journal of the American Ceramic Society*, vol. 88, 2005, pp. 1321-1322.

[108] M. Cologna, B. Rashkova, and R. Raj, "Flash Sintering of Nanograin Zirconia in <5 s at 850°C," *Journal of the American Ceramic Society*, vol. 93, 2010, pp. 3556-3559.

LIST OF TABLES

LIST OF FIGURES

154